UNIVERSITA' DEGLI STUDI DI PADOVA
Dipartimento di Innovazione Meccanica e Gestionale

TECHNICAL UNIVERSITY OF DENMARK
Department of Manufacturing Engineering and Management

Joint Supervision Doctorate

in Manufacturing Engineering

ATOMIC FORCE MICROSCOPY IN NANOMETROLOGY: MODELING AND ENHANCEMENT OF THE INSTRUMENT

Francesco Marinello

Coordinator: Ch.mo Prof. Guido A. Berti

Supervisor: Ch.mo Prof. Paolo F. Bariani

Supervisor: Ch.mo Prof. Leonardo De Chiffre

2006

a mio nonno Giovanni

a mia mamma e mio papà

a Riccardo e Marianna

a Silvia

Then I applied myself to the understanding of wisdom, and also of madness and folly,
but I learned that this, too, is a chasing after the wind

Ho deciso allora di conoscere la sapienza e la scienza, come anche la stoltezza e la follia,
e ho compreso che anche questo è un inseguire il vento

Jeg vendte min Hu til at fatte, hvad der er Visdom og Kundskab, og hvad der er Dårskab og
Tåbelighed; jeg skønnede, at også det er Jag efter Vind

É porque me esforcei grandemente por ser sábio, e não ignorante; no entanto dou-me conta agora
de que até isto foi também como correr atrás de nada

Me he dedicado de lleno a la comprensión de la sabiduría, y hasta conozco la necedad y la
insensatez. ¡Pero aun esto es querer alcanzar el viento!

Und richtete auch mein Herz darauf, daß ich erkennte Weisheit und erkennte Tollheit und
Torheit. Ich ward aber gewahr, daß solches auch Mühe um Wind ist.

Je me suis, en effet, appliqué à connaître la sagesse, ainsi que ce qui est fou et ce qui est stupide.
Et je me suis aperçu que cela aussi, c'est comme courir après le vent.

Dedique cor meum, ut scirem sapientiam et scientiam, insipientiam et stultitiam.
Et agnovi quod in his quoque esset afflictio spiritus

И предал я сердце мое тому, чтобы познать мудрость и познать безумие и глупость:
узнал, что и это-томление духа

私は，一心に知恵と知識を，狂氣と愚かさを知ろうとした．
それもまた風を追うようなものであることを知った

내가 다시 지혜를 알고자 하며 미친 것과 미련한 것을 알고자 하여 마음을 썼으나 이것도 바람을
잡으려는 것인 줄을 깨달았도다
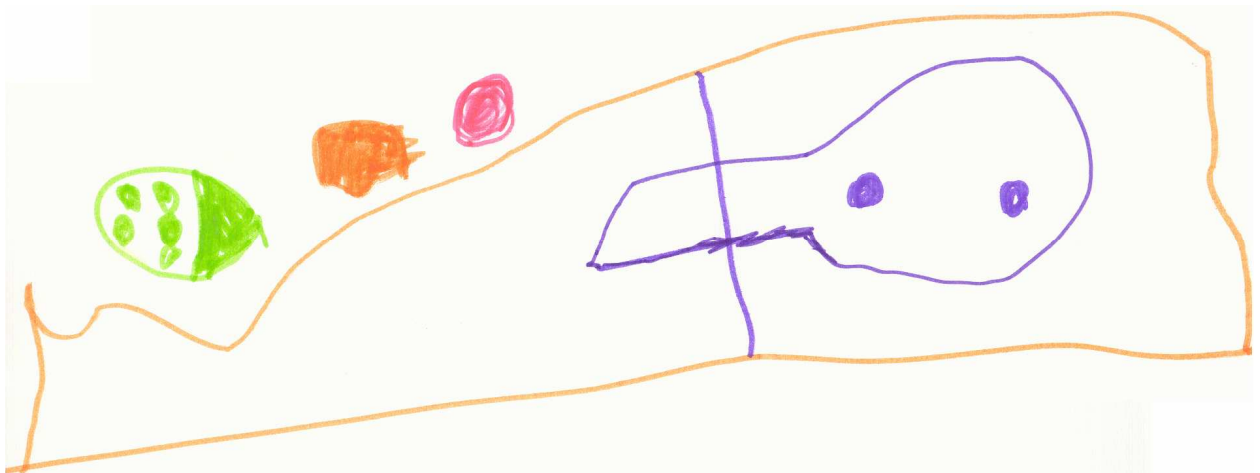
Preface

This dissertation is submitted in partial fulfillment of the requirements for the degree of Doctor of Philosophy.

The work has been carried out from January 2004 to December 2006 at the Department of Innovation in Mechanics and Management (DIMEG), University of Padua, and at the Department of Manufacturing Engineering (IPL), Technical University of Denmark (DTU). It has been performed under the supervision of Professor Paolo Bariani (at DIMEG) and Professor Leonardo De Chiffre (at IPL).

In the following I would like to share my thanks with the people who walked on my side on this *journey*. To anyone who falls in that category who I leave out (and I can guarantee there will be at least one), I'm sorry. It's a reflection of my faulty memory, not your contribution.

First of all I would like to thank my official and unofficial supervisors Prof. Paolo F. Bariani, Prof. Leonardo De Chiffre and Prof. Enrico Savio. I have very much appreciated how they trusted and believed in my abilities, and the ability they had to push me towards obtaining good results in the various projects that make this thesis.

The present work is a continuation of investigations carried on by Dr. Paolo Bariani during his PhD: he has the merit of many results here discussed. I want to express to Paolo my deep and sincere gratitude, for the enthusiasm he brought into our research: I enjoyed working with him.

I wish to thank Dr. Jørgen Garnæs (DFM, Dansk Fundamental Metrologi A/S), Dr. Jan Friis Jørgensen (Image Metrology A/S) and Prof. Hans Nørgaard Hansen, for very constructive advice and inspiring discussions.

Furthermore I want to thank all the students who have been carrying out their M. Sc. projects under my supervision: Oscar, Stefano, Manuel, Riccardo, Maritzia, Nicola, Marco, Alessandro, Enrico and Lorenzo. Not only have I enjoyed their company, but also, I have benefited a lot from their work.

Really thanks to Dr. Gaoliang Dai (PTB): he and his works have been an inspiring source and a model for me.

I am grateful to all my colleagues, with whom I have shared the experience of being a Ph.D. student at our department: they helped to keep the daily friendly atmosphere.

Thanks to my friends, for their support and friendship over the years. Special thanks are for Matteo, Martina, Stefania and Luisa: they are a gift to me.

And thank to my family, that really has too many merits: I feel blessed!

Last, but far from least, thank you Silvia. Your smile is my joy.

Abstract

This Ph.D. project is aimed at developing and validating techniques for successful use of Atomic Force Microscopy in nanometrology. In particular modeling of the instrument behavior, appropriate calibration, correction of distortions and enhancement of AFMs performances are addressed.

Typical AFM error sources are described, mainly arising from the scanning system, the probe, the environment and from data processing subsequent to measurement. Scaling and crosstalk, creep and hysteresis, noise, drift, tip convolution and software are some of the error sources discussed. Different contributions are eventually unified into a single mathematical model, which in principle completely describes AFM scanning.

The issue of AFM calibration is addressed. A new concept of calibration standards is introduced, based on optical fiber technology. It is shown how fiber micro-cylinders can be applied for accurate calibration of horizontal and vertical AFM axes, in the whole scan range. Crosstalk error evaluation and correction are also discussed.

The work continues with a section discussing the possibility of compensating or avoiding typical AFM distortions. Three-dimensional topography reconstruction achieved through surface coupling is proposed for elimination of vertical drift artifacts. Application of an auto-correlation function is then proposed for alignment of profiles and lateral drift distortion removal.

A method for modeling distortions due to tip wear rate in contact mode AFM is eventually proposed, based on lateral force monitoring.

The last part addresses instrument enhancement, proposing a solution to three typical AFM problems. 1) Difficult tip access to steep slopes is overcome through matching and coupling of two or more surface topographies, scanned with different installation slopes. 2) A matching automatic routine is also implemented for mosaicking operations: stitching of three-dimensional topography data sets allows the maximum measurable range limitations to be overcome. 3) The problem of scan time reduction is discussed in the last section, where a feature oriented measurement approach is investigated for overcoming raster scan limitations. With the new method, the probe is driven along free-form paths, scanning with high resolution only discrete features of interest and collecting only relevant data.

Abstract (Italiano)

L'obiettivo di questo progetto di dottorato è stato lo sviluppo e la conseguente validazione di tecniche per un utilizzo efficace della Microscopia a Forza Atomica (AFM). L'attenzione si è concentrata in particolare sulla modellazione del comportamento dello strumento, la sua taratura, la correzione delle distorsioni e il miglioramento delle prestazioni.

Uno studio sulle distorsioni ha condotto a identificare quattro principali fonti d'errore: il sistema di scansione, la sonda, l'ambiente di misura e il processamento dei dati successivo alla misura. Ortogonalità, creep e isteresi, rumore, deriva, convoluzione e software di analisi sono solo alcune delle distorsioni descritte. I diversi contributi sono stati quindi riuniti in un unico modello matematico, che ha l'obiettivo di definire un sistema di riferimento completo per la descrizione delle operazioni di scansione degli AFM.

La trattazione continua con la taratura dello strumento. Viene presentato un nuovo artefatto di taratura, basato sulle tecnologia delle fibre ottiche. La disponibilità di micro-cilindri di elevata qualità consente infatti un'accurata taratura degli AFM sia sul piano orizzontale che sul piano verticale. Nella stessa sezione viene discussa anche la caratterizzazione della perpendicolarità degli assi, con la conseguente compensazione degli errori di ortogonalità.

Viene anche trattata la possibilità di correggere o evitare alcune distorsioni tipiche degli AFM.

Per la compensazione dei fenomeni di deriva sul piano verticale, viene suggerita una ricostruzione tridimensionale, ottenuta mediante accoppiamento di scansioni fatte lungo direzioni perpendicolari. Una funzione di autocorrelazione viene invece applicata per eseguire un allineamento di profili, andando così a correggere le deviazioni causate da deriva sul piano laterale. Viene anche proposto un metodo che, attraverso una mappatura delle forze torsionali che agiscono sulla sonda dell'AFM, consente di monitorare in modo rapido ed efficace il tasso di usura della punta che esegue la scansione.

L'ultima parte affronta lo sviluppo delle prestazioni dello strumento. 1) La caratterizzazione di zone difficilmente accessibili dallo strumento è risolta attraverso l'accoppiamento di misure fatte con inclinazioni diverse. 2) L'unione di più scansioni successive viene utilizzato anche per allargare il range totale di misura dello strumento. 3) L'ultima parte propone infine un approccio intelligente di misura che consente una notevole riduzione dei tempi di misura. Il metodo è basato su un controllo intelligente del sistema di attuazione, che consente di muovere la sonda solo lungo percorsi che ottimizzano la misura concentrandola solo su zone di effettivo interesse.

Contents

Chapter 1

Introduction

1.1   The scenario

Technology is continuously evolving. In the last fifty years the mechanical field as well as electronics, medicine, telecommunications or IT have seen a continuous development. All these cited fields are somehow correlated: in fact the development of one is not independent of improvements in other fields, but there is at least one field that can be considered "collateral" to the others: metrology. In general the importance of metrology is proportional to how far it helps other technologies to improve. Competition, together with market needs, is a perfect engine, pushing technology toward new frontiers. As foreseen more than forty years ago by Feynman, nowadays that frontier is called "nanotechnology" [1].

Nano refers to a nanometer (nm). A nanometer is a billionth of a meter, a dimension less than 1/100000 the diameter of a human hair. Nanotechnology describes many diverse technologies and tools, which very often do not have too much in common. They exploit the fact that, at this scale, materials can behave very differently from when they are in larger form. Nanomaterials can be stronger or lighter, or conduct heat or electricity in a different way, appear in a different color or react in a faster way. Some of these properties are already implemented in a number of micro- and nano-devices, but research is still at the beginning of a long journey which every day progressively leads to new developments and discoveries.

The fields of nanoscience and nanotechnology are broad and still at the exploratory stage, with connections to almost all disciplines and areas of relevance: some application ideas are just visionary interpretations of the nano-world, but on the other hand important results have already been achieved such as, for instance, the realization of nanostructures and nano-manipulation (Figure 1.1).

Figure 1.1: Nanotechnology overview [2].

It is a fact that the potential for nanotechnologies is promising in areas as diverse as healthcare, IT and energy storage: and this idea is clearly shared and supported by governments' investments and businesses across the world (Figure 1.2a).

Figure 1.2: a) Worldwide government funding for nanotechnology Research and Development; b) Nanotechnology R&D "S" development curve [3].

The worldwide nanotechnology research and development (R&D) investment reported by government organizations increased by a factor of 3.5 between 1997 and 2001, and the highest rate of 90% was in 2001. It is estimated that 2001 was somewhere at the beginning sector of the classical "S" development curve of nanotechnology, and after about five years we are now on the fast rising sector of that curve (Figure 1.2b).

Nanotechnology is at the center of a growing debate among scientists, regulators, industry representatives, policy makers and others, over economical implications, interests, future needs and initiatives. Various initiatives have been taken at the international level, in Europe [4] [5] as well as in America [6] or in Asia [7]. In particular the US National Nanotechnology Initiative Workshop, held in Maryland in 2004, produced an important report dealing with the definition of a roadmap in nanometrology [6]. Instrumentation and metrology are both critical areas, essential to the emerging nanotechnology enterprise: progress in fundamental nanoscience, development of new nanomaterials, and ultimately production of nanotechnology-based products are all depending to some extent on the possibility of accurately and reproducibly measure properties at the nanoscale.

Similarly in the Supplement to the US president's FY 2007 budget [8], it is pointed out how instrumentation metrology and standards are key links in the chain from discovery to commercialization. Research efforts have to push forward the boundaries of knowledge in instrumentation and metrology and bring state-of-the-art tools and techniques to bear in the development of standards for the nanotechnology community.

Improvements in metrological instrumentation have facilitated significant advances in nano-research; however resolution and accuracy of current instruments are being stretched to the limit by the needs of researchers in the present as well as manufacturing processes in the immediate future.

A natural trend is to focus attention in particular on surfaces. In fact interface of solid states in nanoscale plays a very important role, being one of the most significant issues to affect properties, including electrical, optical, mechanical properties, etc. Understanding surfaces is a prerequisite for understanding properties: for this reason instruments allowing for surface characterization play a fundamental role at this moment in the nanoevolution.

Imaging individual atoms has been an elusive goal for many years, more precisely until 1981, when Binnig and Rohrer (rewarded with the Nobel Prize in Physics in 1986), with Gerber and Weibel introduced the scanning tunneling microscope (STM). This instrument revolutionized our ability to investigate matter on the atomic scale: in fact for the first time, the individual surface atoms could be visualized. Within one year of its invention, the STM helped to solve one of the

most interesting problems in surface science: the structure of the Si(111)-(7×7) surface. Figure 1.3 shows these first measurements performed by an STM and reported also in Binnig's Nobel Prize lecture (1987) [9].
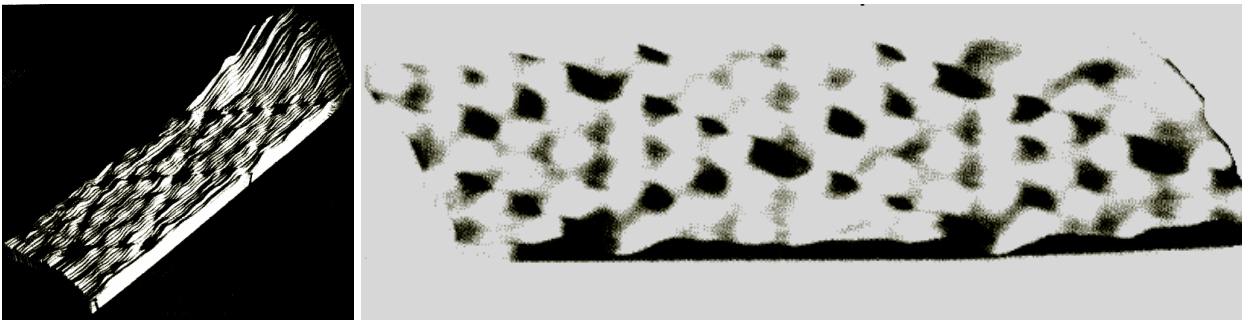

Figure 1.3: Processed images of the 7×7 reconstruction of Si(111), as originally reported in [10].

The spectacular spatial resolution of the STM along with its intriguing simplicity determined the rapid success of the STM, launching a broad research effort with significant impacts on surface science. A large number of metals and semiconductors was investigated on the atomic scale and wonderful images of the world of atoms were created after the inception of the STM. Today, the STM is considered a fundamental advancement for scientific research, but yet it had limited applications, because it worked only on electrically conductive samples.

A major advancement in profilers occurred in 1986 when Binning and Quate demonstrated the Atomic Force Microscope (AFM) [11]. Thanks to a micro probe tip fixed at the end of a cantilever, the AFM could achieve extremely high resolution scans. Initially, the motion of the cantilever was monitored with an STM tip. However, it was soon realized that a light-lever, could be employed for measuring the motion of the cantilever. In their paper, Binning and Quate also proposed a new improvement for the AFM: measurements could be performed by vibrating the cantilever above the surface. The vibrating cantilever technique was first tested and demonstrated in 1987 by Wickramsinghe [12], who measured the amplitude of the vibrations through an optical interferometer. Using this optical technique, oscillation amplitudes of between 0.3 nm and 100 nm were achieved. Since at each oscillation the probe comes into close contact with the surface, it was possible to characterize the surface topography.

After the invention of the STM and AFM, the way was open for the realization of different types of Scanning Probe Microscopes (SPMs), based on different principles: Lateral Force, Magnetic Force, Electrostatic Force, Near-field, etc.

1.2 Challenges

Today, we have the advantage of many years of instrument development, tens of thousands of publications by researchers all over the world (Figure 1.4), and the commercial production of SPMs, which have become a common and relatively inexpensive analysis tool.
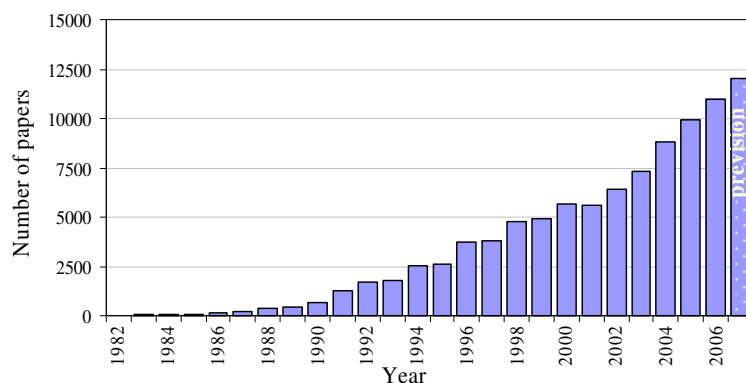
Figure 1.4: Growth of publications in scanning probe microscopy, as determined by searching the ISI Science Citation Index.

SPM applications have spread out, covering a number of different areas, where nano-features and nano-tolerances must be dimensionally quantified. A number of barriers have been broken in recent years but still many of the problems in the existing metrology systems and approaches need to be overcome. The goal for the future is to accomplish advanced metrology techniques to characterize complex, heterogeneous samples in three dimensions over all relevant time and length scales. This is better described in Table 1.1, where the key challenges and barriers in nanometrology are reported in detail.

Table 1.1: Key challenges and barriers for nanocharacterization [6].

Area	Challenges / Barriers
3D Characterization of Structures	- Spatial and spectral resolution and specificity - Data acquisition speed and throughput limitations - Synthesis of 3D information from 2 D datasets - Merging of data from different metrology tools - Measurement artifacts
Interface characterization	- Non-destructive characterization - Buried or embedded interfaces - Interface stability - Probe robustness - Preserving process/sample in situ
Speed of characterization	- Detector speed, efficiency and sensitivity - Source brightness - Software for smart analysis, fast data collection and processing - Fast automated sample preparation

In particular the ability to examine complex structures in three dimensions is felt as a fundamental aspect. And the solution will most probably arise from measurement strategies that enable data taken using one tool to be merged with complementary data taken from separate tools.

1.3 Problem identification

Metrology in the micro- and nano-scale still presents a number of open issues: as highlighted in the previous paragraph, unresolved problems are felt in the instrument development as well as in software, in the measurement approach, in the calibration/verification or in the normative definition.

The general purpose of this project was the enhancement of the existing methods for scanning probe microscopes metrology. Improvements have regarded different aspects of scanning probe and atomic force microscopy. The environment where the work was carried out was deeply involved in problems related with practical applications: therefore an eye has been constantly kept on the industrial benefits and on the potential impact of the proposed solutions.

In particular the work starts giving a description of the context where Atomic Force Microscopy is used and most benefits are achieved from its implementation (Chapter 2).

A review is then presented of all the problems and distortions, commonly affecting atomic force microscope measurements. The global instrument behavior is also described through a complex mathematical model, which can be seen as the ultimate reference model for the complete description of scanning probe instruments. This issue is addressed in Chapter 3.

In Chapter 4 a new concept of calibration standards, based on optical fibers technology is presented, for the horizontal and vertical calibration of scanners. The orthogonality problem is also discussed, with the development of a software tool for evaluation and compensation of crosstalk errors.

Two of the problems most affecting AFM scanning, not or only partially compensated by recent instruments developments, are distortions caused by drift and by tip convolution.

A software strategy for compensating drift distortions and a method for foreseeing tip wear and thus avoiding distortion due worn tips use, are object of the discussion in Chapter 5.

Possible instrument enhancements are eventually presented in Chapter 6. Here the work deals with the improvement of AFM performance in terms of increase of the maximum detectable

slope, enlargement of the maximum measured range and reduction of measuring time through scan path optimization.

The merit of the present work is also connected with the simplicity of the proposed solutions. At the basis of the solutions here developed there is a whish to suggest affordable answers, easily implementable in the industrial fields.

Chapter 2

Scanning Probe Microscopy

2.1 Principles

In the context of micro- and nanotechnology, Scanning Probe Microscopy is one of the elected techniques for fine surface and geometrical characterization [13]. Scanning probe microscopy is a branch of microscopy, imaging surfaces by means of a physical probe that scans the specimen. The basic SPM is relatively simple in concept. Its closest predecessor is the stylus profiler: SPM technology uses sharper probes and lower forces than stylus profilers to provide higher resolution information without sample damage. Surface topographies are obtained by mechanically moving the probe in a raster scan over the specimen, and recording point by point, line by line the interaction between the probe and the surface as a function of the position.

A generic SPM comprises the following components: a scanning system, a probe, a probe motion sensor, a controller, a noise isolator and a computer.

The movement of the tip or sample is performed by an extremely precise positioning device, usually made from piezoelectric ceramics, most often in the form of a tube scanner. Systems based on other actuation principles, such as voice coil, are also available. The scanner is capable of sub-nanometer resolution in x-, y- and z-directions: it is the most fundamental component and the hearth of the microscope. Another key component in the system is the probe. As mentioned above, the probe can be stationary and the sample can be scanned under it or the probe can be scanned over the sample. Sharp tips are integrated into the end of cantilevers, which have a wide range of properties designed for a variety of applications.

The probe motion sensor unit senses the force between the probe and the sample and provides a correction signal to the Z portion of the piezoelectric scanner to keep the force or the distance constant. An optical beam deflection system (optical lever) is often applied for this purpose, ensuring the lowest noise, stability and versatility. The trend now is to replace the optical lever with "self-sensing" means like, for instance, piezoelectric cantilevers or tuning forks.

The control electronics provides interfacing between the computer, the scanning system, and the probe motion sensor. It supplies the voltages that drive the piezoelectric actuator, accepts the signal from the probe motion sensor and includes the feedback control electronics for keeping the force or the distance between sample and tip constant.

To achieve the highest resolution, the microscope must be isolated from external noise (mechanical and acoustic vibrations, electrical and optical noise). A computer and software interface finally is used to drive the system and to process, display, and analyze produced data.

SPMs can image interactions, based on different physical principles: atomic force, capacitance, friction, magnetic fields,... The manner of using these interactions to obtain an image is generally called "mode". The mode is used to classify the typology of SPM, as resumed in the table below.
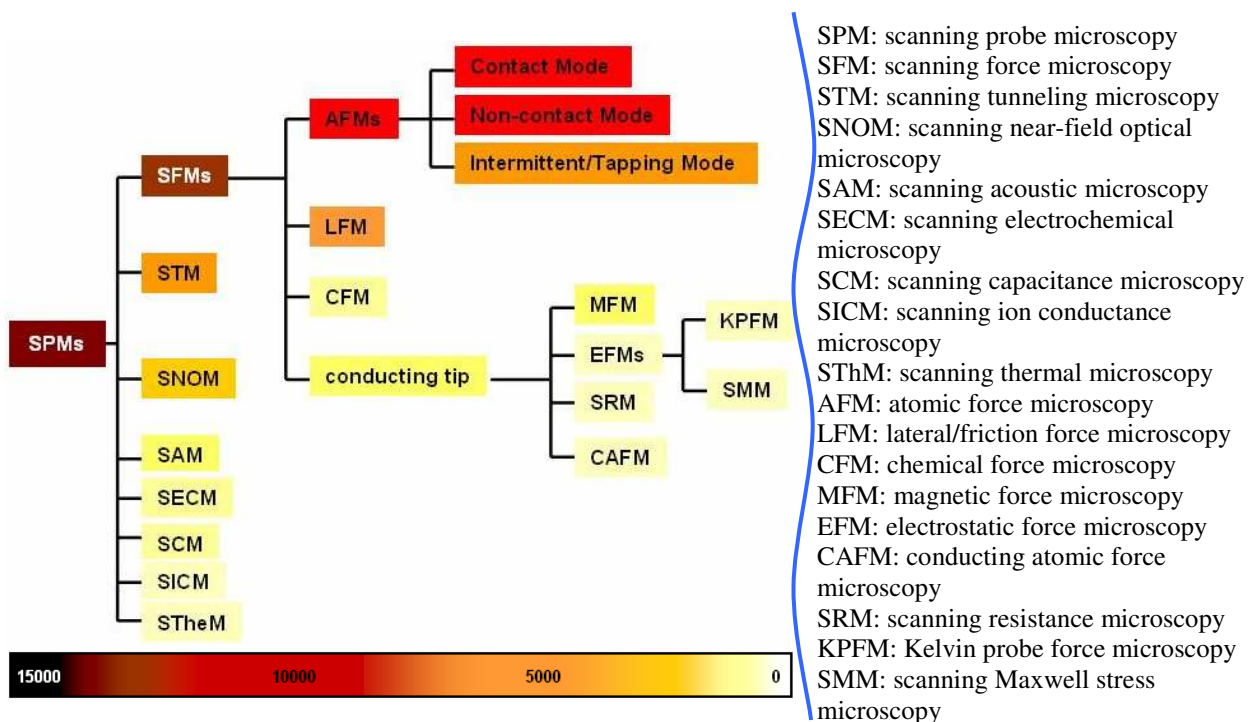

SPM: scanning probe microscopy
SFM: scanning force microscopy
STM: scanning tunneling microscopy
SNOM: scanning near-field optical microscopy
SAM: scanning acoustic microscopy
SECM: scanning electrochemical microscopy
SCM: scanning capacitance microscopy
SICM: scanning ion conductance microscopy
SThM: scanning thermal microscopy
AFM: atomic force microscopy
LFM: lateral/friction force microscopy
CFM: chemical force microscopy
MFM: magnetic force microscopy
EFM: electrostatic force microscopy
CAFM: conducting atomic force microscopy
SRM: scanning resistance microscopy
KPFM: Kelvin probe force microscopy
SMM: scanning Maxwell stress microscopy

Figure 2.1: Scanning probe microscopy techniques [14].

The greatest strength of STMs and AFMs is their ability to sample the vertical and lateral topography information with the highest resolution. Moreover, techniques such as SCM and EFM are able to capture additional information such as surface electrical charge (q), capacitance (C) and surface potential (V). Techniques that use the different behavior of oscillating cantilevers such as contact, non-contact, tapping mode, phase angle and shear mode may be used, enabling different surface and sub-surface characteristics to be imaged. In addition, the rapid development of scanning near-field optical microscopy (SNOM) and more recently scanning probe Raman microscopy is also further developing molecular and chemical analysis in the nanoscale.

Table 2.1: Main SPMs characteristics (images taken from [2]).

NAME	MAIN CHARACTERISTICS	SOME EXAMPLES
Contact Mode AFM	Measures topography with the probe perpetually in contact with the sample.	
Non-contact Mode AFM:	Measures topography by sensing Van der Waals attraction. It is less stable than either contact or Intermittent mode.	
Intermittent AFM	Measures topography by tapping the surface with an oscillating probe tip. Eliminates shear forces (present in contact mode).	
Lateral Force Microscopy (LFM)	Maps frictional forces between the probe tip and the sample surface. The tip can be functionalized for chemical force microscopy.	
Chemical Force Microscopy (CFM)	Evaluates the strengths of specific forces of attraction, and to map spatial distribution of the ligands patterned on the surface.	
Magnetic Force Microscopy (MFM)	Maps magnetic force gradient and distribution above the sample surface.	
Electric Force Microscopy (EFM)	Maps electric field gradient and distribution above the sample surface.	
Scanning Resistance Microscopy (SRM)	Allows determination of two-dimensional dopant profiles.	
Conducting Atomic Force Microscope (CAFM)	Characterizes electrical properties (such as conduction) of surfaces.	
Scanning Tunneling Microscopy (STM)	Measures topography using the tunneling current between the probe tip and a conductive sample surface.	
Scanning Near-field Optical Microscopy (SNOM)	Measures topography and very local optical properties.	
Scanning Acoustic Microscopy (SAM)	Is a non-destructive failure analysis and inspection technique, for studying cracks and pores even when they are hidden from view.	
Scanning Electrochemical Microscopy (SECM)	Measures the potential difference between a potentiometric probe and a sample immersed in an electrolyte solution or a polar liquid.	
Scanning Capacitance Microscopy (SCM)	Maps 2D carrier (dopant) concentration profiles in semiconductor materials.	
Scanning Ion Conduction Microscopy (SICM)	Can be used on living tissues, to image ion currents through membrane channels.	
Scanning Thermal Microscopy (SThM)	Maps surface temperature distribution.	

Characteristics of main SPMs are briefly described in the previous table (Table 2.1), together with some example applications. Successively the attention is focused on atomic force microscopy, the scanning technique that is mainly object of study and development in this work.

2.1.1 Atomic Force Microscopy

Atomic Force Microscopy is the most common of the SPM techniques, diffusely applied in a wide range of research as well as industrial fields [15] [16].

The surface is probed through a sharp tip, located at the free end of a cantilever that is 100 to 400 µm long. This tip is some microns long, with a curvature at the very end that is often less than 10nm; high force sensitivities (between 10^{-7} and 10^{-12} N) make possible the measurement of a single, chemical bond-breaking force. Having an appropriately sized tip is important for acquiring real surface features and atomic resolutions, but advancements in piezoelectric transducers (PZT) are responsible for enabling SPMs to probe a surface with sub-Ångstrom precision. As the tip is scanned over the sample, or the sample is scanned under the tip forces between the tip and the sample surface cause spatial deflections and oscillations of the cantilever. The key information gathered in AFM comes with measuring those deflections, quantified by means of an optical lever system, coupled with position sensitive a photodiode. In Figure 2.3, the probe tip is shown in contact with the sample surface: during scanning, as z-displacements cause cantilever flexions, the light from the laser is reflected onto the split photodiode.
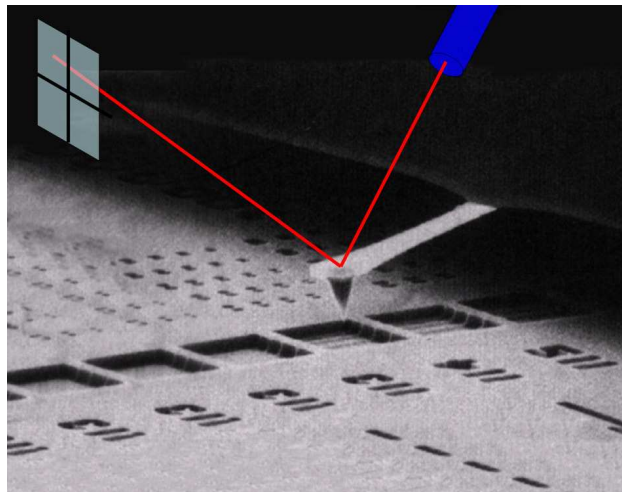
Figure 2.3: Optical lever AFM [2].

By measuring the difference signal, changes in the bending of the cantilever can be measured, while an input can is given to a servo system that ensures the force or the distance between the sample and the tip to be constant.

2.1.2 Modes

Several forces typically contribute to the deflection of an AFM cantilever. The force most commonly associated with atomic force microscopy is an interatomic weak force called the van der Waals force. The dependence of the energy associated with van der Waals effect upon the distance between the tip and the sample is shown in Figure 2.4.
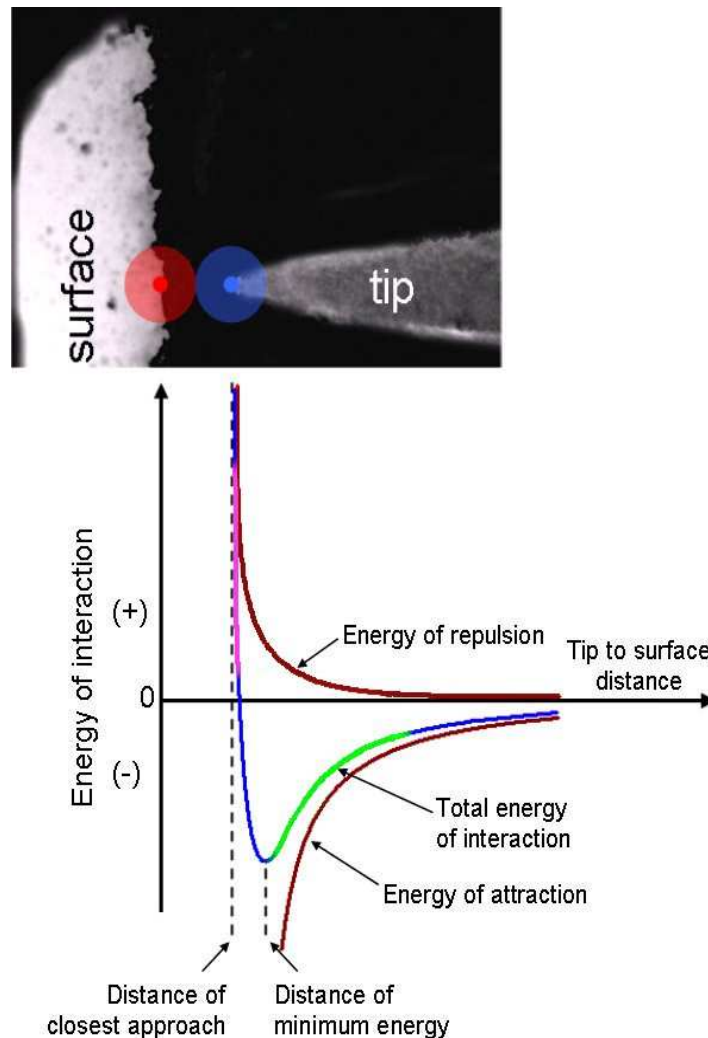
Figure 2.4: Total energy of interaction as a function of the distance between the tip and the surface atoms.

Two distance regimes are put in evidence in Figure 2.4:

- the violet colored zone, below the distance of minimum energy (<1 nm), where the interatomic force between the tip and sample is repulsive;

- the green colored zone, above the distance of minimum energy (about 1-30 nm), where the interatomic force between the tip and sample is attractive.

The repulsion regime is used for the so called contact mode: the tip is scanned across the sample while a feedback loop maintains constant cantilever deflection and force. Other two working modes are commonly used: non-contact and intermittent contact, both operating in the repulsive

force region. These are dynamic modes, since the cantilever is oscillated close to its resonance frequency, above the surface. For Non-Contact AFM the force is measured by comparing the frequency and/or the amplitude of the cantilever oscillation relative to the driving signal. In the intermittent mode the oscillation amplitude is significantly higher (~5-30 nm) and the tip rhythmically touches the surface.

2.2   Industrial applications

Scanning probe microscopes are instruments designed primarily for the characterization of surface topographies with a very high spatial resolution. In their first applications, AFMs were used mainly for measuring 3D surface topography and, although they can now be used to measure many other surface properties, that is still their primary application.

Several industrial and research fields benefit from AFM technology. A classification inspired by [17], [18] and [19] is proposed in the following table (Table 2.2).

This classification encompasses:

- product groups;

- instrument integration level;

- measurement tasks.

"*Product groups*" runs through the technical areas and industries that are applying AFMs techniques. As shown in the table the "*integration level*" includes *applied research* studies, with potential industrial interest, studies by *industry in research*, *manufacturing off-line* usage, to conclude with the highest level of integration, the *manufacturing on-line* use.

An idea of the type and complexity of the generic measurement tasks to be performed is also given. The classification includes:

- dimensions, defined as distances between points or surfaces. Example: width, height or length.

- geometry or form, as defined by the distance between the surface of the object and a pre-defined reference. Example: flatness or curvature.

- texture and roughness, defined as geometries of surface structures whose dimensions are small compared to the object under investigation. Example: widths, heights or lengths. Example: bearing analysis, smoothness or porosity.

Typical applications are also reported, not with the aim of exhaustively enumerate all the fields where atomic force microscopy can play an important role, but with the intent of showing the wide and assorted range of technological clusters where AFM brings relevant benefits.

Table 2.2: Industrial and research applications of AFM technology, by industrial area and level of usage.

Product Group	Measurements tasks			Integration level				Applications
	Dimensions	Geometry	Roughness	Applied res.	Industrial res.	Manuf. off-line	Manuf. on-line	
Mechanical parts	↑	↑	↑	▓	▓			Microgears
								Micromotors
								Microactuators
Microelectronics	↑	↓	↔	▓	▓	▓		Sensors (accelerometers,…)
								MEMS
								Microphones
Biomedicine and biology	↑	↑	↑	▓	▓			Microspeakers
								Hearing aids
								Surgey devices
Chemistry	↑	↓	↑	▓				Implants (stents,…)
								Particles
								Microfluidics
Optics	↓	↑	↑	▓	▓			Micropumps
								Plasmon resonance sensors
								Optical switch
Data storage	↑	↓	↑	▓	▓	▓		Micromirrors
								Lenses
								Hard disks
Polymers and coatings	↓	↑	↑	▓	▓			Magnetic disks
								Thin Films
								Micro-injected parts

2.2.1 Mechanical parts

Mechanical field represents those applications where surface functional emphasis is on moving components and on their tribological interactions. Much of the work carried on in research laboratories is focused in material science and engineering. Thanks to its relatively easy use, AFM can be well introduced in process control, gaining great advantage in the evaluation of final product characteristics. In particular, microstructure control during both the forming phases and subsequent heat treatments can be accurately carried out with the aim of linking microstructural parameters to the product mechanical behavior during its service life [20] [21] [22] [23].

Another important investigation is the analysis of micro-machined surfaces. Quantification of surface topography is of fundamental importance for the evaluation of the generated surface; high resolution and wide measuring range being highly desirable for the evaluation of tool-workpiece interaction (Figure 2.5) [24].

Workpiece roughness also influences properties such as wear, friction, adhesion, light scattering capacitance and corrosion, even more in the microscale. Often these measurements are not possible with classical profilometers, due to the reduced dimensions or to the softness of the material to be investigated. Similarly also working tools can be finely characterized: this is very relevant, since the quality of the final worked surface is strictly connected to the condition of the working tool.
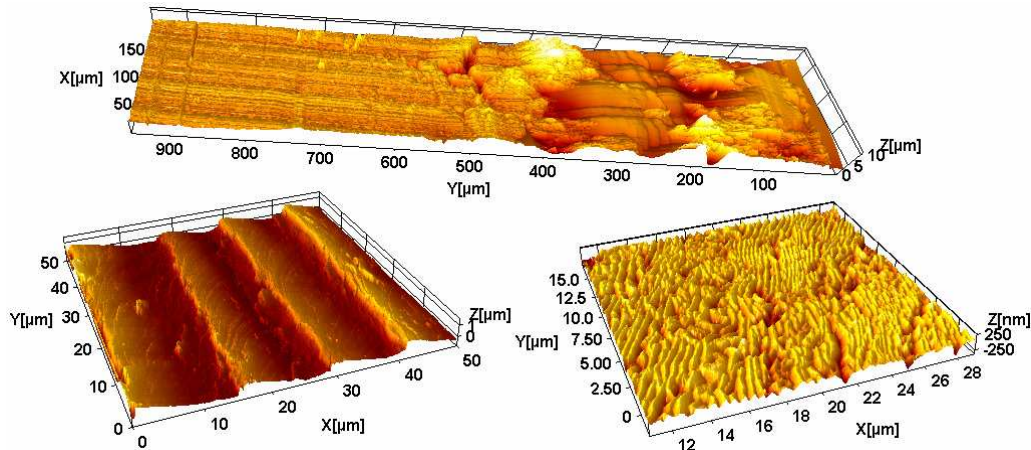
Figure 2.5: Three examples from the mechanical field: interface after punch operation, surface generated by ball nose micromilling and pearlitic microstructure.

2.2.2 Microelectronics

Thanks to its high lateral resolution, AFM is extensively used in the semiconductor industry, where a fast constant shrinking of circuit elements is progressing. Primary needs include measurement of linewidths, step heights, sidewall angles, surface and line edge roughness.

Normally AFMs are used as an additional measuring technique, supporting and complementing faster methods, such as scanning electron microscopy or scatterometry. In-line application of atomic force microscopy is preferred when quantitative measurements are needed also in the vertical direction. Even if slow, in this case AFM provides non-destructive measurement, whereas SEM technique would need sample sectioning for the measurement.

A scanning probe technique is also desirable whenever roughness measurements have to be carried on, due to its unique ability to measure topography with nanometer scale spatial resolution. An important application is also the characterization of rugged silicon topography, useful for increasing capacitance of devices on semiconductor chips.

New instrument set ups have also been developed, with the introduction of new concept allowing for fine sidewall characterization. In particular the realization of boot-shaped tips associated with vertical scan movements allowed for overcoming typical problems associated with cone tips and flanks related distortions [25] [26].

2.2.3 Biomedicine and biology

As recognized by the Nanomaterial Roadmap 2015 [27], Atomic Force Microscopy plays and will play a unique role in the future development of the biomedical sector, thanks to its flexibility and multiplicity of applications. In fact AFM is seen as a double purpose instrument, allowing not only for characterization, but also for manipulation or active functionalization of surfaces.

AFMs have been used for the structural characterization of starch and proteins and have helped to better understand the mechanism of gel formation for biopolymers, or the interfacial distribution and interaction of surfactants in emulsions and microemulsions. These studies have significant value for controlling the functionality, quality, and shelf stability of foods and food ingredients [28]. AFM analysis is also used to get insight into the barrier potential and nanoscale properties of edible biopolymer films and coatings. Finally AFM can also be instrumental in probing the local mechanical and adhesive properties and phase behavior in multi-phase foods, or for evaluating the compatibility of food ingredients.

Very interesting is the use of atomic force microscopy as an active working tool. Etching surfaces with nanoscale grooves or imprinting them with cell attachment molecules (the so called "nanostructuring") can improve cellular attachment and direct cells to grow into defined structures: this is fundamental for example for providing an anti-microbial coating on implants or for improving biocompatibility.

Another relevant application seen in the future development of biomedicine is the realization of smaller and more sensitive microarrays for use in diagnostics and drug discovery.

2.2.4 Chemistry

AFMs are instruments with an unique versatility. In particular the possibility of imaging surfaces with nanometric resolution while functioning in solution, is very interesting for use in situ in electrochemistry. Even though times are still not mature for significant applications in electrochemical processes, relevant studies are normally performed in research and industrial fields.

A typical use is the observation of surface topography evolution during electrochemical reactions, as for example surface structure before and after catalyzed dissolutions.

Very relevant is also the possibility of characterizing small particles: in particular AFM allows for characterization of powder size and distribution with the highest resolution. For instance a typical application is the calibration of mono-disperse reference gold colloids or polymer spheres with various sizes.

A new field has recently gone exponentially increasing its importance becoming a major research topic during the last decade: products for chemical and biochemical analysis of fluid. These so-called lab-on-a-chip components are manufactured both in silicon and polymer material. The geometries of these devices are essentially flat, with features dimensions in the order of some microns. The metrological requirements for quality assurance are well fulfilled by atomic force microscopy: in particular roughness, dimensions and volume of microchannels can be precisely characterized with AFMs [19].

2.2.5 Optics

The quality of optical components used in complex applications such as lasers, microscopes, medical imaging/diagnostics and lithography systems, is critically influenced by surface morphology. Micro-optics have 2D structures with relatively low aspect ratios and dimensions generally ranging from tens to hundreds of microns. Form accuracy is a key measurand and similarly precision assembly is critical to the performance of the component. Typical measurands are: surface roughness, lattice constants, alignment accuracy (for fibers) etc.

A further consideration can be done with regard to optical systems: the majority of the components (lenses, mirrors, beamsplitters, polarizers, etc.) are covered by thin film optical coatings. Hence, important properties of the optical elements such as optical scattering, are significantly influenced by the surface microstructure of the thin film coating. With the ongoing trend of today's optical lithography towards shorter wavelengths, thin film research and industry are facing drastically increasing requirements for low-scatter optics in the UV, and deep UV, spectral region. The surface microstructure of a thin film coating can be advantageously measured through Atomic Force Microscopy. From scattering theories it is well-known that the amount of optical scatter depends not only on the roughness height of a structure but also on its lateral distribution. At a randomly rough surface, many different spatial frequencies are present. This is quantitatively expressed by the Power Spectral Density (PSD), giving the relative strength of each roughness component of a surface microstructure as a function of spatial frequency. Proper AFM data analysis can substantially support predictions about scatter losses in thin film optical coatings and hence, help reduce these losses through PSD-controlled optimization of the processes [29].

2.2.6 Data storage

Data storage is traditionally represented by magnetic recording media, in particular by hard disk drives and magneto-optic devices.

As well known, information on hard disk is stored in terms of bits: microscopic areas (300 nm or less in width) having or not having local magnetic dipole. The writing module operates inducing local magnetic moments in bit areas of hard disk magnetic layer. On the other hand, non magnetized bits cause measurable change in resistance of the magnetoresistive sensor in the reading module, enabling to distinguish between two levels of digital signal.

The progress in hard disk engineering is the result of reduction of sizes of all the materials and modules involved in the process of magnetic recording.

Nowadays thickness of magnetic sublayers and protective carbon coatings have shrunk down to some nanometers and heads hover over disk surface at heights not exceeding 50 nm.

Moving on so small heights requires extraordinary quality of disk surface: defects or particles could in fact severely damage the surface with moving head. Similarly, the effect of nonuniform thermal expansion becomes not negligible at this development stage.

Atomic Force Microscopy easily copes with these tasks, resulting to be a fundamental tool for monitoring of roughness and defectiveness of disk surface as well as magnetic head topography with nanometer accuracy.

Moreover it has been reported about several attempts to measure protective carbon coating (COC) hardness in order to estimate its wear resistance. AFM scratching technique is successfully applied to estimate the scratch resistance of ultrathin protective coatings [30].

Using cantilever with magnetic coating we acquire a powerful technique known as Magnetic Force Microscopy (MFM) for the characterization of bit structure of both hard disk and read/write head. Magnetic force microscopy has become a powerful tool for mapping stray fields: thanks to its high lateral resolution MFM now is the standard method to measure bit lengths and widths, and furthermore is accepted as one of the most precise techniques for the characterization of bit structure irregularities.

Optical compact disks contain a pattern of tiny pits in a plastic substrate medium read by an infrared laser sensor. For HD-DVD (High Density Digital Versatile Discs) data marks with lengths of about 200 nm are produced. The quality of the pits is of great importance in optical disc technology, and AFM are key techniques for assessing the quality of the stamped replica discs as well as laser ablated masters.

Investigations for the active application of AFM for data storage are held intensively by IBM: the most famous development is known as "Millipede" [31]. The bit writing module can be realized with a cantilever equipped with a heater: the tip makes indentation in a plastic substrate that stands for a logical "1". Erasing of data is performed by means of heating either entire plastic card or its local region. This approach for single lever allows for reaching densities of

hundreds Gbit per square inch though at the expense of relatively low data transfer rates up to 10 Mbit/s. Millipede overcomes this limitation, using many cantilevers working in parallel (Figure 2.6).
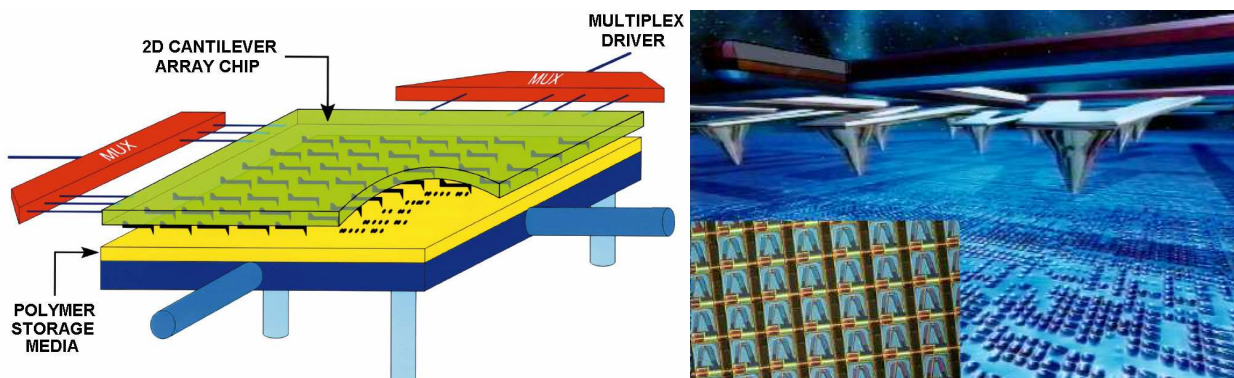
Figure 2.6: The "Millipede" concept and a SEM image of the writing results: bit indentations are equivalent to a storage density of 100-200 Gb/in² [31].

2.2.7 Polymers and coatings

The term polymer covers a large, diverse group of molecules, including substances from proteins to high-strength kevlar fibers. A key feature that distinguishes polymers from other large molecules is the repetition of units of atoms (monomers) in their chains. This occurs during polymerization, in which many monomer molecules link to each other.

Multiscale structuring and the resulting materials properties across the hierarchy of length scales from atomic, to macroscopic is an absolute necessity. Furthermore, it is fundamental to understand the critical roles that surfaces and interfaces play in nano- and micro-structured materials: this is true both for polymer components and coatings. In fact a fundamental role is played not only by the structure of these interfaces, but also by their local chemistries, segregation and interaction.

Scanning Probe Microscopy plays a primary role: in particular a great variety of products and processes can gain great benefits from AFMs techniques. Typical examples are the particle analysis during printing, analysis of component mixing in injection molding and film forming processes. In particular adhesion, wettability, friction wear, stiffness, scratch damage and appearance are key performance criteria for coatings and polymer additives. Interest in atomic force microscopy is due to the possibility of both studying surface morphology and measure chemical and nano-mechanical properties. Efforts are being done also for a traceable measurement of thin films thickness, independent from material parameters [32].

A particular mention is here given also to micro-injection molding. Complex geometries bring challenges during the filling stage of the process: many features (holes, pins and cores, micro inserts, etc.) cause melt front separation. When two or more melt flows join each other after

separation a weld line is formed on the surface of the micro molded part. This phenomenon has to be avoided or at least reduced because in the weld line area the mechanical properties are lower than in the bulk part, creating strength problems on the final part. Atomic force microscopy can be successfully applied to the topographical characterization of weld lines on micro injection molded parts and subsequent interpretation of main driving factors influence [33] [34] (Figure 2.7).
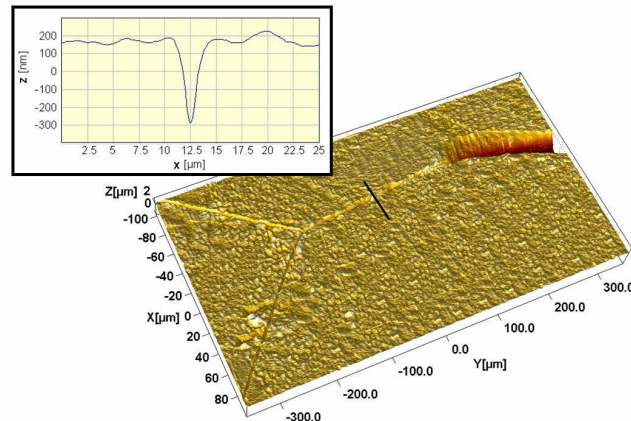
Figure 2.7: Large Range AFM scan of a triple weld line: in the zoom box a single profile is plotted.

2.3   Open issues

The vision for nanocharacterization, as developed in [6] for the future is to achieve advanced methods and metrology techniques to characterize complex heterogeneous samples in three dimensions over all relevant time and length scales.

Micro- and nanocharacterization span issues in several directions, including length measurement, shapes of pores and particles, 3D characterization, etc. To support to the nanotechnology industry, some advances are considered urgent:

- realization of nanoscale 3D imaging capabilities;

- acquisition of robust and artifact free measurement methods;

- development of quantitative metrology with analytical capabilities that parallel what is currently achievable on the micro- and meso-scale.

Several steps forward have been made in recent years. In particular, with the advent of scanning probe microscopy many things are possible and practical today that were not possible 20 years ago.

Furthermore, advanced computer control, with digital and spectral imaging approaches has revolutionized all the microscopy methods allowing quantitative spatially resolved spectroscopy

and higher throughput of specimens with easier and more reliable acquisition. Although full automation has not yet been achieved, there is a definite trend in that direction.

Metrological tools are needed that push the limits of what can be realized in terms of sensitivity, spatial resolution, data acquisition speed and time resolution. At the same time, instrumentation will also be needed that is robust, amenable to production environments and affordable.

The following table (Table 2.4) proposes an attempt to organize the main metrology challenges and barriers, with particular reference to SPMs/AFMs. A level of importance/urgency is also proposed: it is proposed to give only a qualitative idea of how it is perceived both in the micro- and in the nanoscale.

Table 2.3: Main SPM/AFM metrology challenges and barriers.

Category	Metrology challenges	Micro	Nano
Interface	Non-destructive characterization	↑	↑↑
	3D characterization	↑↑↑	↑↑
	Interface stability	↑	↑↑
	Buried or embedded or inaccessible interfaces	↑↑	↑
	Preserving process/sample in situ	↑	↑
	Large range measurements	↑↑↑	↑↑
Instrument	Modeling of instrument behavior	↑	↑↑
	High throughput metrology	↑	↑
	High sensitive/high accuracy/high resolution	↑↑	↑↑↑
	Measuring range enlargement	↑↑	↑
	Stability in space and time	↑	↑↑
	High accuracy 3D positioning over large volume	↑	↑
	High speed/real time measurement	↑↑↑	↑↑↑
	Calibration: standards and modeling	↑	↑↑
	Automation	↑↑	↑
	Avoid artifacts	↑↑	↑↑
Probe	Probe robustness	↑↑	↑
	Tips sharpness	↑	↑↑
	Modeling of tip wear	↑	↑↑
	Modeling of tip to surface interaction	↑	↑
	Tip influence/deconvolution	↑	↑↑
Method and analysis	Bridging from microscale to nanoscale	↑	↑
	Merging of data from different metrology tools	↑	↑
	Tolerance system definition	↑	↑
	Software for design, control and modeling	↑	↑
	Software for fast data collection and processing	↑	↑
	Tolerance verification	↑	↑
	Simulation of measurement	↑	↑
	Quantitative parametrization	↑↑	↑↑
	Post-processing: data manipulation and correction	↑↑	↑↑

In the author's opinion, the main challenges regard the possibility of performing fast and accurate 3D measurements in relatively large ranges, reducing tip influence as far as possible.

There are two possible ways of overcoming the numerous barriers to existing metrology systems and approaches: an evolutionary advance or, through a significant breakthrough, the development of new concept-based techniques.

In the following chapters, the intention is to propose techniques for an intelligent solution of some metrological requirements, and in particular in the scanning probe microscopy field. Solution will have the characteristic of being easily implementable, even in commercial instruments, with no or very few hardware modification needs.

Chapter 3

AFM Modeling

3.1 Introduction

Experience suggests that Atomic Force Microscope measurements suffer from distortions, which reduce the image quality and introduce uncertainty in quantitative evaluation. As a result, this can shade or alter processes occurring on the surface under investigation. AFM data then need special processing for correcting distortions coming from bad instrument calibration, and eliminating so called artifacts, which can come from improper scan settings or external effects.
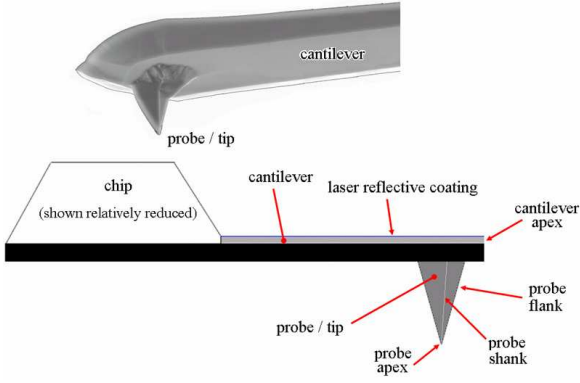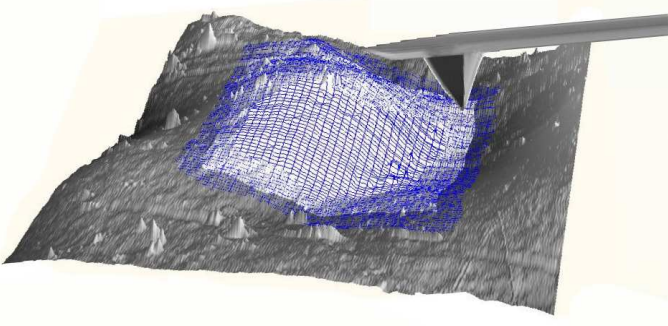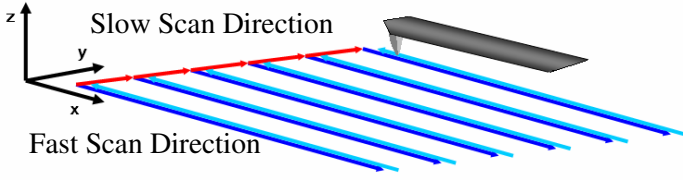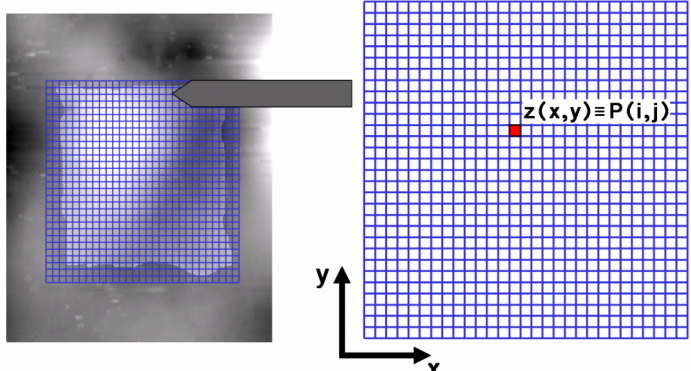
In AFM literature the term "artifact" is used to identify measuring distortions; it has not to be confused with the calibration artefacts (cited for instance in Chapter 4), which identify reference objects for calibration purposes

In this chapter, a classification and description will be given of the most common artifacts affecting AFM measurements. Scaling and crosstalk, creep and hysteresis, noise, drift, tip convolution and software will be some of the error sources discussed here. A theoretical model is also introduced for a complete description of instrument behavior. This model is quite complex: it was designed to define a reference framework, able to give a mathematical *collocation* to the different distortions occurring. The following chapters will be devoted to the presentation of possible solutions to some of the problems described here.

3.2 Basic terminology

The present chapter starts with a table, schematizing most recurrent and important terms (Table 3.1). These will be of help, for a proper comprehension and correct interpretation of the topics discussed in the following. In particular the pixels matrix presented in the last row is the model commonly used by commercial instruments and analysis software for topography representation [35] [36].

Table 3.1: Basic terminology.

Representation	Description
	Surface topographies are achieved by scanning a probe over a surface. In the case of an AFM, the probe is generally made by silicon and consists of a sharp tip sticking out of a piece called cantilever.
	The probe is scanned over the surface in a raster fashion. Surface topography is reconstructed through a collection of parallel profiles.
	Normally two main directions are used to describe SPMs probe movement: x, the so called "Fast Scan Direction", parallel to the profiles, and y the "Slow Scan Direction", perpendicular to the first one. Each profile is normally scanned twice: one forward and one back. The two movements are normally indicated as "scan" or "trace" and "back-scan" or "retrace".
	Surface is eventually characterized by a matrix of points (usually referred as pixels), called "image". Positions i,j in the matrix corresponds to physical positions x,y in the surface. The value stored in i,j cell of the matrix is the vertical elevation z.

3.3   AFM distortions and artifacts

All measurement instrumentation used by scientists for research development and quality control generates results that may be affected by error sources. In this paragraph there is an identification and organization of the main distortions occurring during AFM imaging. This review is divided by the sources that originate the problem; there are four main sources in atomic force microscope measurements: scanning system, probing system, environment, and image processing. The "environment" class stands for those phenomena coming from the complex instrument-operator-room system and affecting the measurement operation. Table 3.2 reports a classification of main distortions and relative sources, discussed in the following. Lines within the table are dotted on purpose: even if a main source has been identified, generally those distortions have to be regarded as the result of multiple interactions rather than the effect of a single direct origin.

Table 3.2: Main AFM distortions.

SOURCE	DISTORTION
scanning system	scaling crosstalk non-linearity creep overshoots mode-switching
probing system	convolution unsampled parts tip artifacts
environment	drift noise
data-processing	filtering leveling

3.3.1 Scaling

As already described, Atomic Force Microscopes are based on a scanner: this provides lateral movement to the probing system. The lateral movement is electronically controlled: a certain voltage step is associated with a relative displacement. Knowing the characteristic of the actuating system allows for the extrapolation of the scanner position. Open-loop system rely on this information: the supplied voltage is therefore used for defining the x,y coordinates of the scanned systems. Conversely, closed-loop systems are provided with a feedback control in the horizontal x,y plane, and tip position is monitored with respect to a reference frame. For

reference instruments (Metrological AFMs) the highest precision is achieved by integration with laser-interferometers. A classification of AFM scanners is given in Table 3.3.

Table 3.3: Classification of AFM scanners [37].

AFM	Position control	Linearity
Metrological	integrated interferometers (traceable by laser wavelength)	~0.01%
Closed-loop	integrated position sensors (capacitive, inductive, encoders,…)	<1%
Open-loop	open loop (positioning based on applied voltage)	<10%

For both types of instruments, but in particular for open-loop instruments, the measured position doesn't correspond to actual tip position. This leads to a distortion which is in general proportional to the scanned measured range, and that can be described as a linear scaling of scanned topographies. Distortions are commonly in the order of some percent for open-loop instrument, and <<1% in the case of closed-loop scanners. In Figure 3.1 a 1:1:0.7 pyramidal pattern is simulated, together with the same structure virtually measured by an instruments with +9.0%, -4.6% and +0.1% distortions respectively along *x*, *y* and *z* axis. Positive and negative signs refer respectively to dimension enlargement and shrinking.
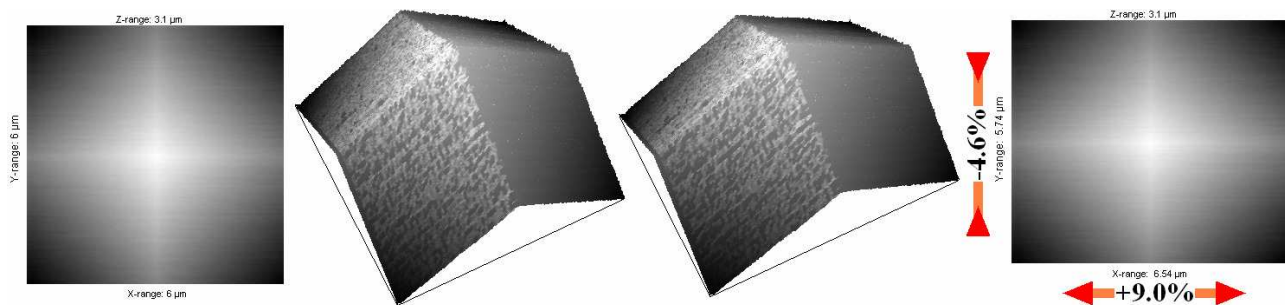
Figure 3.1: Distortion occurring to a pyramidal structure.

Normally calibration operations are used in order to quantify and correct systematic deviations of the measuring device, providing traceability to the SI-unit of length. Upon definition of a reference metric coordinates system, machine readouts are somehow offset to the correct metric values. Determination of proper correction coefficients is done by statistical analysis. Ideally, after calibration, systematic offsets are null, and probed coordinates accuracy is determined by a random spread distributed around the value. For Metrological AFMs traceability to the SI-unit of length is realized directly via the wavelength of the used laser. The lower class of instruments, which encompasses those AFMs having integrated position sensors (capacitive, inductive, strain

gauges, encoders), is usually calibrated by temporarily attaching laser-interferometers to the scan system or by using high quality physical standards. The last class of AFMs, with open loop instruments using the applied voltage as position control, have to be calibrated usually using physical transfer standards [37]. Most commonly, transfer standards consist of one or two-dimensional gratings with various arrangement of structures, allowing for lateral and vertical calibration. In Section 4.3 a new sample and a new method for horizontal calibration is introduced. Calibration is also discussed in Section 4.4, where an innovative vertical calibration standard and technique are presented. A mathematical model can be introduced in order to describe the scaling problem. In this model and from here on it is assumed that the fast scanning direction coincides with the x axis. Assuming that the imaging process leads only to linearly distorted images, the correct tip position is given by:

$$\begin{bmatrix} x \\ y \\ z \end{bmatrix} = \begin{bmatrix} c_{xx'} & 0 & 0 \\ 0 & c_{yy'} & 0 \\ 0 & 0 & c_{zz'} \end{bmatrix} \cdot \begin{bmatrix} x' \\ y' \\ z' \end{bmatrix} \tag{3.1}$$

and using the compact notation:

$$M_{xyz} = C_{xyz} \cdot M'_{xyz} \tag{3.2}$$

In (3.1) and (3.2) measured coordinates are noted with an apostrophe ', while the calibration matrix C allows determination of the metric coordinates X through correction of measured coordinates X': the terms on the principal diagonal represent scaling factors.

$$c_{xx'} = \frac{\partial x}{\partial x'} \qquad c_{yy'} = \frac{\partial x}{\partial x'} \qquad c_{zz'} = \frac{\partial x}{\partial x'}. \tag{3.3}$$

3.3.2 Crosstalk

Deviations from orthogonality, known also as squareness errors, between coordinate axes are possible. These deviations occur when movements of the probing system along the three axes are not uncorrelated, and movements set along one direction generate uncontrolled shifts along the other directions. This kind of problem can be resembled as an angular misalignment between instrument and reference ideal coordinate axes system. Crosstalk is of concern for open-loop AFMs, and in a minor way for closed-loop and metrological instruments, where the parasitic angular motion due to the Abbe error in displacement measurements is present.

In Figure 3.2 the result of crosstalk is shown applied to the same pyramidal structure seen before. Crosstalk errors cause an angular deformation: with reference to Figure 3.2, angles γ_{xy}, γ_{xz} and γ_{yz} represent respectively deviations from orthogonality in the horizontal x,y plane and in the vertical x,z and y,z planes.

Implementation of an automatic routine for determination of γ and subsequent correction is presented in the following (Section 4.5).
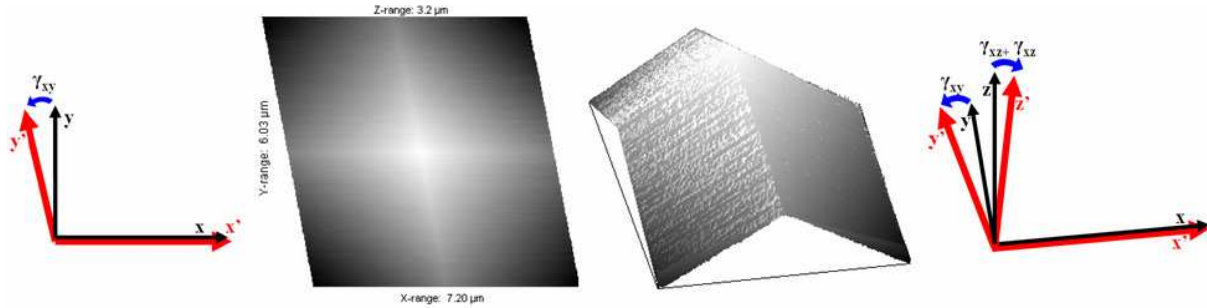
Figure 3.2: Sketch of the angular misalignment between instrument and reference ideal coordinate axes, and effect on a pyramidal structure.

As proposed in the previous paragraph, a mathematical model can be used to describe crosstalk. Assuming that the imaging process leads only to first order squareness distortions, the correct tip position is now given by:

$$
\begin{bmatrix} x \\ y \\ z \end{bmatrix} = \begin{bmatrix} 1 & c_{xy'} & c_{xz'} \\ 0 & 1 & c_{yz'} \\ 0 & 0 & 1 \end{bmatrix} \cdot \begin{bmatrix} x' \\ y' \\ z' \end{bmatrix} \tag{3.4}
$$

Once again, in (3.4) measured coordinates are noted with an apostrophe ', while the calibration matrix C_{xyz} allows determination of the metric coordinates M_{xyz} through correction of measured coordinates X': scaling factors on the principal diagonal are set to 1 meaning that no correction is considered. The three terms lying over the diagonal represent the crosstalk correction factors; they can be evaluated as follows (3.5):

$$
c_{xy'} = \frac{\partial x}{\partial y'} \qquad c_{xz'} = \frac{\partial x}{\partial z'} \qquad c_{yz'} = \frac{\partial y}{\partial z'}. \tag{3.5}
$$

3.3.3 Non-linearity

The linear model discussed in Paragraph 3.3.1 is in practice applicable only to metrological and closed-loop AFM scanners, being these usually controlled by capacitance sensors whose non linearity is in the order of 0.01% or less. Conversely, images delivered by open loop AFM scanners, based on tube or stack piezo-actuators are not linear. In fact scanners based on piezoelectric actuation, the most diffused systems, suffer from hysteresis and creep: consequently the positioning accuracy is significantly reduced due to non-linear hysteresis effects, especially when piezo-actuators are used in relatively long-range, positioning applications.

3.3.3.1 Hysteresis

Because of differences in the material properties and dimensions of each piezoelectric element, AFM scanners respond differently to different applied voltage. This response can be measured in terms of sensitivity, defined as the ratio between the piezo movement and the piezo voltage. In other words how far the piezo extends or contracts subsequently to an applied volt. Sensitivity is not linear, in fact piezo scanners exhibit more sensitivity (i.e. a larger movement per volt) at the end of the scan line than at the beginning. This causes the forward and reverse scan directions to behave differently and display hysteresis between the two scan directions. The effect of nonlinearity and hysteresis can be seen from the curve in Figure 3.3, which shows the relation between the driving voltage of the lateral scanner, and the scanner position is shown in. Two cycles are shown, that are obtained for the subtending voltage intervals on the abscissa axis. The two arms of each cycle describe respectively the trace and retrace displacement of the scanner: the hypothetical transducer in the thick marked cycle, corresponding to a short scan range, exhibits a reduced sensitivity respect to the large cycle. This means that, for any given set of scanning instrumental parameters, the scaling coefficient increases as the nominal scan range is enlarged. Similarly, for a given voltage range, different scan velocities result in change of the slope of the cycle, because of induced creep effects. Scanner positioning is therefore influenced by scan range and speed: non-linear deformation is represented by the distance between the actual and the measured position after correction for linear scaling. These non constant deviations are resembled by arrows comprised between the dotted line and the curve (second graph in Figure 3.3). An example of these effects on AFM images is simulated by the waffle image in the same figure.
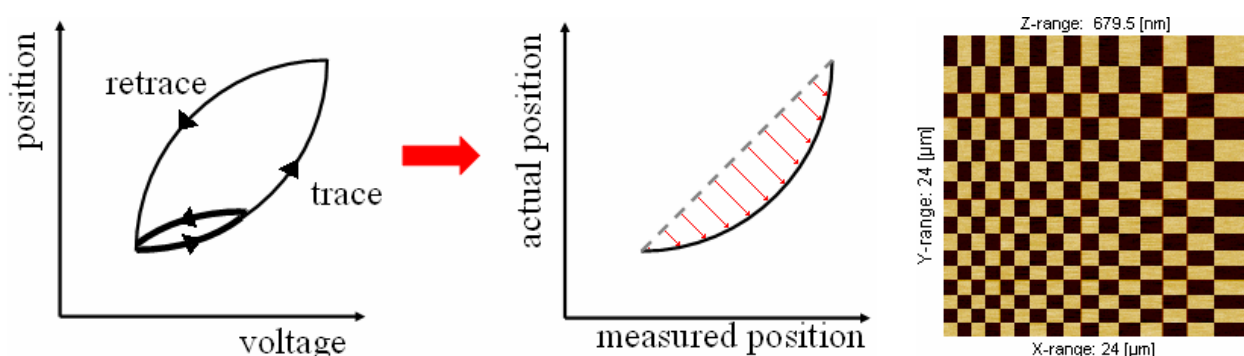
Figure 3.3: Characteristic hysteretic behavior of piezo-actuators and non-linearity influencing AFM measurements. On the right is reported a simulation giving an idea of possible extreme effects of hysteresis on a synthetic waffle image with a regular pattern.

Additionally the sensitivity of piezoelectric materials decreases exponentially with operation time and the form of the exponential depends on how often the scanner is used (aging). If the scanner is not used, the elongation under a certain voltage gradually diminishes, and

consequently also c_{xx} and c_{yy} diminish. If the scanner is exploited at regular short intervals, the elongation coefficient varies more slowly [38].

3.3.3.2 Creep

Creep can be seen as the drift of the piezoelectric actuator after an offset voltage is applied. This usually occurs when large changes are imposed in x or y direction, as for instance when the piezo travels over most of the scan area to restart the scan or after the scanner passes from the trace to the retrace and vice versa. When a large offset voltage is applied, the answer of the scanner is not immediate, not moving the full offset distance all at once. The majority of the offset distance is moved quickly, and then slowly moves over the remainder. In fact when the voltage is sharply changed, the size of a piezoelectric actuator changes in two stages: fast (less than a millisecond) and slow. Creep is a phenomenon characterized by the duration of the second stage, in the horizontal plane, and causes a change of the scan scale and of the position of the scan centre. The scan then resumes after a majority of the offset distance has been moved although the scanner is still slowly moving in the direction of the offset. Creep is the result of this slow movement of the piezo-actuator over the remainder of the offset distance once scanning has resumed. Creep appears in the image as an elongation and stretching of features in the direction of the offset for a short period of time after the offset. An example of creep is shown in the image of a one dimensional calibration standard (Figure 3.4). The tip was scanning from the bottom to the top of the image. The slight bending of the lines which occurs in the bottom of the figure is due to creep. Creep decreases logarithmically, settling out by the end of the scan. What operators usually do in order to avoid creep effects into quantitative measurements is to cut the affected zones out and perform calculations over zones where creep effect is negligible. Alternatively it can be reduced by offsetting beyond the desired point and then offsetting back to the desired initial measuring point [38] [39].
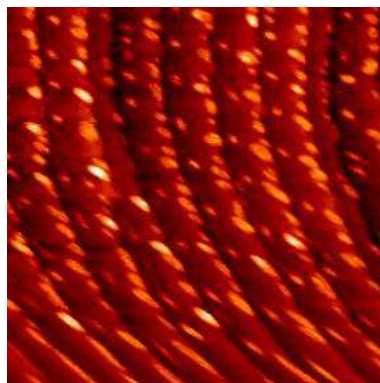
Figure 3.4: 60 nm STM image of the Au(11,12,12) surface. At the bottom of the image, the steps are not straight and Co islands are elongated due to creep of the piezoelectric ceramics [2].

3.3.3.3 Bow

A combination of non-linearity associated with coupling between the vertical axis and the x-y directions is frequent, known as bow distortion. This is a non-linear image artifact, that has the appearance of a false curvature superimposed to the actual specimen topography. This kind of artifact is not due to hysteresis phenomena, but to the particular probe movement, associated with tube scanner architectures. In fact the tip raster scan pattern is achieved by lateral bending of the piezo-tube: this movement is not horizontal but follows a curved trajectory with a radius of curvature generally in the order of some tens of millimeter.

The influence of bow is negligible when measurements are performed in reduced scan ranges, but gets more severe as the scanning range increases. In Figure 3.5 a representation is given of the spherical/paraboloidal movement (depending on the scanner architecture) causing bow artifacts. In the same figure an example is also given of a nominal flat AFM topography affected by bow deformation.

Figure 3.5: (a) Representation of a tube scanner movement causing bow and (b) AFM topography on a flat sample, presenting image bow.

The mathematical model proposed in the two previous paragraphs can now be re-introduced for describing higher order interactions. Assuming that the imaging process is already compensated for first order distortions, the correct tip position is now given by (3.6):

$$
\begin{bmatrix} x \\ y \\ z \end{bmatrix} = \begin{bmatrix} x' \\ y' \\ z' \end{bmatrix} + \begin{bmatrix} c_{xx'^2} & c_{xy'^2} & c_{xz'^2} & c_{xx'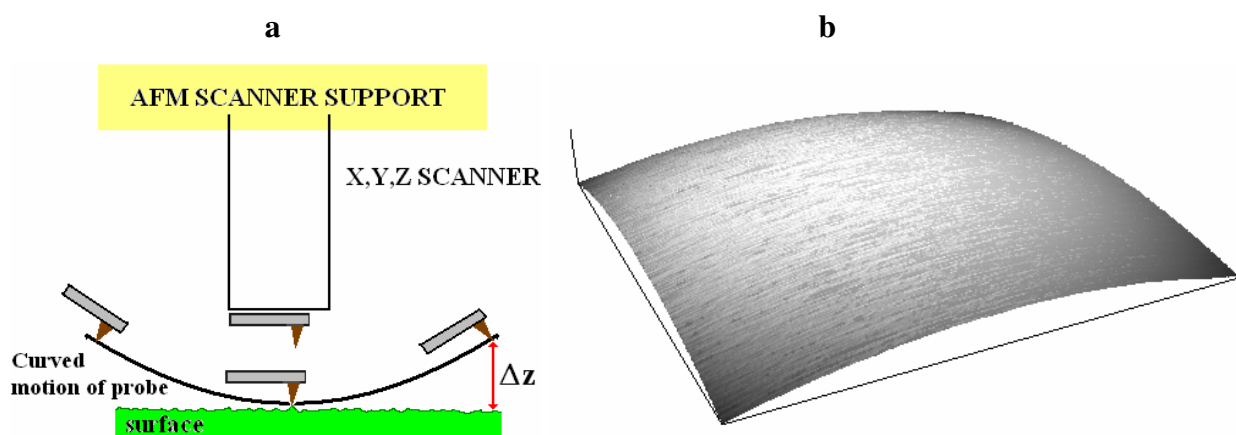y'} & c_{xx'z'} & c_{xy'z'} \\ c_{yx'^2} & c_{yy'^2} & c_{yz'^2} & c_{yx'y'} & c_{yx'z'} & c_{yy'z'} \\ c_{zx'^2} & c_{zy'^2} & c_{zz'^2} & c_{zx'y'} & c_{zx'z'} & c_{zy'z'} \end{bmatrix} \cdot \begin{bmatrix} x'^2 \\ y'^2 \\ z'^2 \\ x'y' \\ x'z' \\ y'z' \end{bmatrix} +
$$

$$
+ \begin{bmatrix} c_{xx'^3} & c_{xy'^3} & c_{xz'^3} & c_{xx'^2y'} & c_{xx'^2z'} & c_{xx'y'^2} & c_{xx'z'^2} & c_{xx'y'z'} \\ c_{yx'^3} & c_{yy'^3} & c_{yz'^3} & c_{yx'^2y'} & c_{yx'^2z'} & c_{yx'y'^2} & c_{yx'z'^2} & c_{yx'y'z'} \\ c_{zx'^3} & c_{zy'^3} & c_{zz'^3} & c_{zx'^2y'} & c_{zx'^2z'} & c_{zx'y'^2} & c_{zx'z'^2} & c_{zx'y'z'} \end{bmatrix} \cdot \begin{bmatrix} x'^3 \\ y'^3 \\ z'^3 \\ x'^2y' \\ x'^2z' \\ x'y'^2 \\ x'z'^2 \\ x'y'z' \end{bmatrix} \qquad (3.6)
$$

or using the compact notation:

$$
M_{xyz} = C_{xyz}^{(1)} \cdot M_{xyz}'^{(1)} + C_{xyz}^{(2)} \cdot M_{xyz}'^{(2)} + C_{xyz}^{(3)} \cdot M_{xyz}'^{(3)} \qquad (3.7)
$$

Where:

- $c_{xx'^2}$, $c_{xx'^3}$, $c_{yy'^2}$, $c_{yy'^3}$, $c_{zz'^2}$ and $c_{zz'^3}$ represent second and third order non-linearities along the three coordinate axes;

- all the other coefficients describe second and third order non-linear coupled interaction (i.e. cross correlation between axes);

- in particular $c_{zx'^2}$, $c_{zy'^2}$, $c_{zx'^3}$ and $c_{zy'^3}$ represent the second and third order parameters of the paraboloid that best fits the bow deformation.

Of course not all of the coefficients in (3.6) have the same importance and influence for the instrument characterization.

3.3.4 Overshoots

Bad compensation of hysteresis and creep in the piezoelectric ceramic that moves the cantilever in the motion perpendicular to the surface, can cause edge overshoot.

This problem is often observed when measuring micro-fabricated structures such as step-patterns of silicon wafers. The result is an over-extension of the step in the proximity of the edge. An example is given in Figure 3.6a, where the arrows indicate overshoots in the line profile, at the leading and trailing edge of the structure [40]. The scanned image usually shows a better apparent contrast, but quantitative measurements, especially the ones in the vertical axis, results bad influenced.

A reduction of this kind of distortion can be achieved by operating on the loop gain. An accurate definition of this parameter will avoid also other problems, generally related with measurements on edges, such as the one reported in Figure 3.6b and Figure 3.6c. Excessive gains bring in fact to instability, with the appearance of superimposed vibrations. On the other hand excessive low gains cause the image to be blurred and smoothed, with tip flights causing an increment in the total length of unsampled parts.
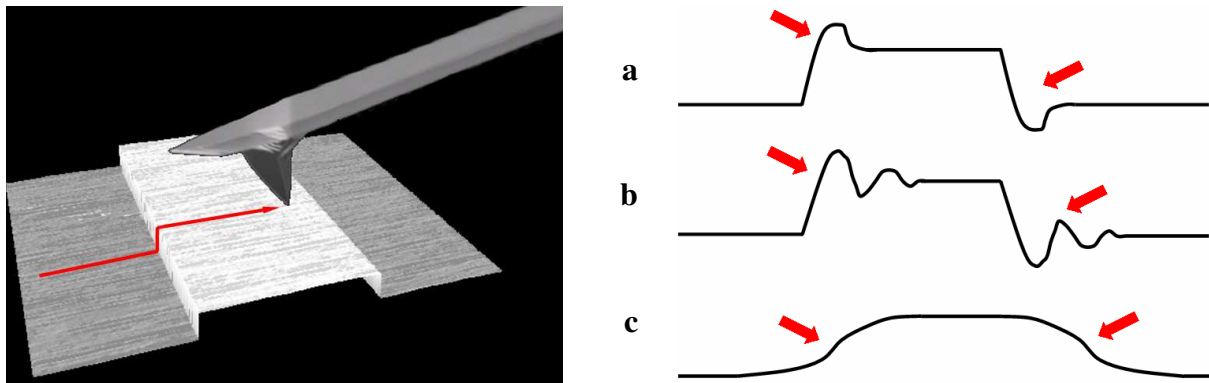
Figure 3.6: The probe is scanned from lest to right across the step. Typical edge artifacts: a) Overshoots, related to bad compensation of creep and hysteresis of the vertical servo control; b) feedback instability due to excessive gain and (c) smooth edge, the two terraces are far apart from each other.

3.3.5 Mode switching

When recording images with an AFM using the intermittent mode, artifacts may affect the imaging process, appearing as unexpected height shifts. An example is given in Figure 3.7, where characteristic fringes show up around the structures. In the same figure a segmentation of these fringes is proposed, together with a profile evidencing the apparent height level shift. The height level shifts can simply be interpreted as stochastic jumps from repulsive to attractive mode and back. When a jump from repulsive to attractive mode occurs during imaging, the feedback loop, which tries to keep the amplitude constant, will respond by re-retracting the probe from the sample in order to increase the suddenly decreased amplitude to the set-point level. The result is a height level shift *upwards*, i.e. the structures seem buried [38] [39] [40] [41].

The sudden increase/decrease in the amplitude is then related to the tip to surface interaction. For a given surface, characterized through AFM with a given set of parameters, the phenomenon has a certain stability. In fact it occurs in proximity of well defined topography slopes and curvatures, producing height shifts with a certain constancy.

A discussion regarding the compensation of this phenomenon is proposed at Appendix B.

a   **b**   **c**   **d**
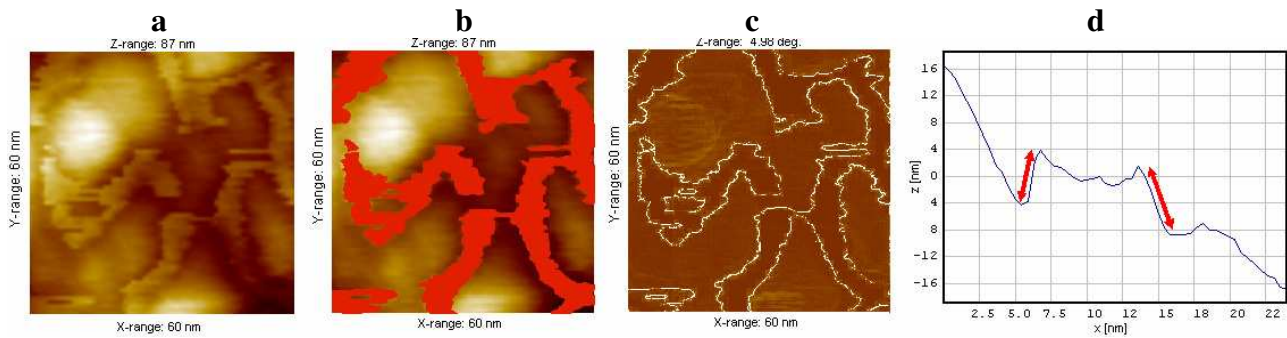
Figure 3.7: a) Fringes around NiO structures due to mode switching; b) and c) segmentation and isolation of jumps; d) profile evidencing an apparent height level shift.

Similar effects can be produced when different interaction forces interfere during scanning. By way of example, local electrical charges on the surface, magnetic forces or capillary forces due to humidity may act on the tip. These influence the measurement, leading to attractive or repulsive additional force contributes, that bring distortions to the measurement.

3.3.6 Convolution

AFM measurements are the result of scanning over a surface using a mechanical probe of finite dimensions, and the resulting topography includes features of both the measurand and the probe shape. This interaction is normally known as convolution effect and introduces distortions that are particularly evident whenever structures with sharp details are measured in the nanometer range.

The most visible effect of convolution is the dilation of the measured topography.

How the surface image is created is shown in Figure 3.8. In this example, the tip side, in that position, touches the sample before that the tip apex, because the tip width does not allow the tip apex to reach the sidewall of the step.

Since the image is created only by the position of the tip apex, the measured topography is different from the sample topography; this means that the apex is not always the actual contact point. This originates the problem of dilation.

Figure 3.8: The conventional model for imaging [42].

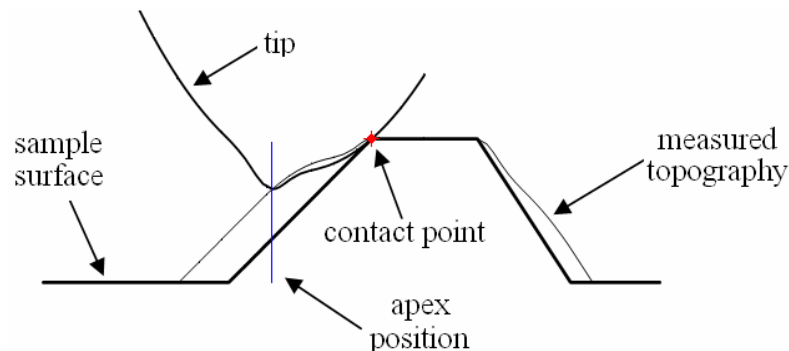The imaged topography is the replica of the surface obtained if an inverted tip is placed at all points on the surface. The envelope produced by these inverted tip images is the image of the surface [43] [44]. Therefore dilation can be graphically represented as in Figure 3.9. There, *I*, *S* and *P* are the sets of which the function *i*, *s* and *p* are the respective tops. *P* is defined as the reflection of the tip, through the origin.
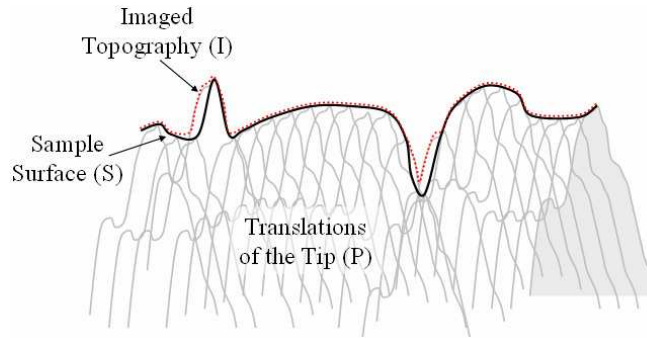
Figure 3.9: Forming the image by dilation.

The amount of dilation depends on the shape and orientation of the probe as well as on the surface topography. The description the dilation process can be defined through Equation (3.8):

$$I = S \oplus P \tag{3.8}$$

The operator $\oplus$ is used to indicate the convolution; it can be more extensively expressed as (3.9):

$$i(x, y) = \max_{(u,v)}[s(x - u, y - v) + p(u, v)] \tag{3.9}$$

where *u* and *v* are the components of a vector defining the translation related with the convolution phenomenon.

Partial compensation for dilation can be achieved through erosion operations. Erosion is not the inverse operation of dilation, but the dual of the dilation.

In fact, although it is not possible to define an actual contour of those surface regions not touched by the tip during scanning, an approximation S_r of the real image of the sample surface can be evaluated as follows (Equations (3.10) and (3.11)):

$$S = I \, \Theta P \tag{3.10}$$

The deconvolution operator Θ can be more extensively expressed as:

$$s_r(x, y) = \min_{(u,v)}[i(x + u, y + v) - p(u, v)] \tag{3.11}$$

The shape of the tip is always "convolved" with the surface; a couple of considerations can be then produced [45]:

- dilation shrinks holes and pits while broadens peaks and bumps [46] (Figure 3.10a);
- a sharper tip can resolve smaller structures than a bull tip (Figure 3.10b and Figure 3.10c);
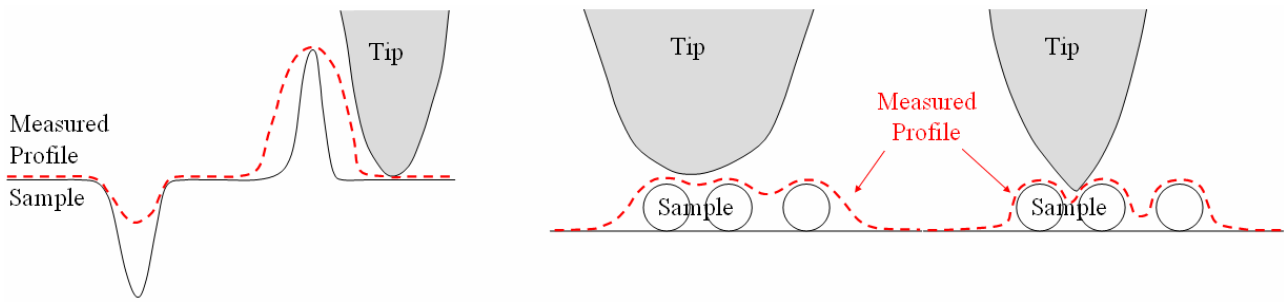
Figure 3.10: Tip radius curvature effect: a) holes shrinking and peaks broadening; b) and c) tip curvature effect.

Distortions are more significant whenever tip dimensions come closer to measured features dimensions. Image dilation is then a problem as soon as the AFM tip becomes comparable in size with the surface structure [47].

When the tip width is smaller than a certain feature distance, the image obtained shows the two features well resolved, as the tip width becomes larger than the feature separation distance, the image shows the two features to be broadened.

Without an estimate of the tip shape, sometime it is impossible to say what part of the imaged topographies is due to the tip and what part is due to the sample. Furthermore, the amplitude of these distortions is not constant. Due to physical effects and dynamic interactions, tip shape evolves with time: in particular continuous deterioration is introduced by wear effects. This worsens even more the problem, since a correct compensation, usually called deconvolution operation, would ask for a frequent monitoring of tip dimensions.

3.3.7 Unsampled parts

A direct consequence of the observations presented in the previous Paragraph 1.2.6 is the lack of data in correspondence of inaccessible regions. In fact Atomic Force Microscope is an instrument measuring "from above": this, combined with the finite dimensions of the probing tip, produces inconsistent values in proximity of steep slopes, narrow cavities, undercuts or hidden parts (Figure 3.11).

Figure 3.11: Examples of unsampled parts: undercuts and narrow cavities are not properly characterized.

Overcoming these instrument limitations is not easy. A simple reduction of the tip dimensions is often insufficient to provide a proper surface characterization. Thu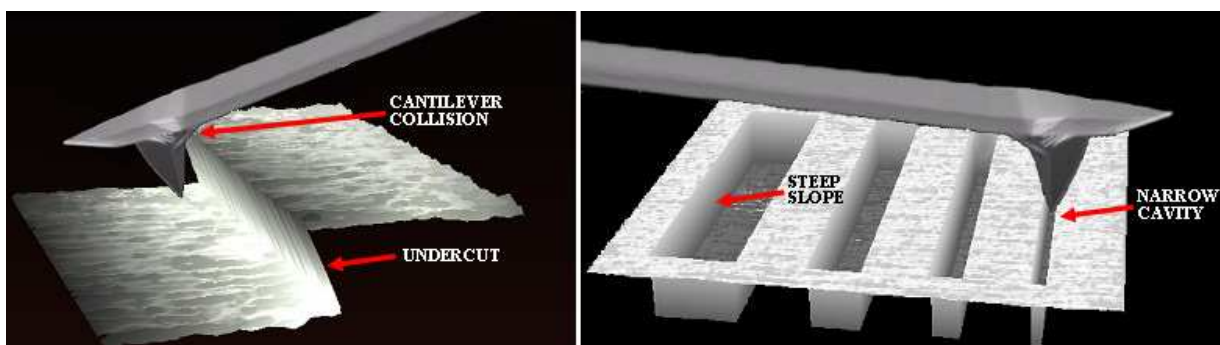s development of a new instrument architecture or a new measurement set up is made necessary: this will be discussed again, with the development of a double tilting technique (Paragraph 6.2).

3.3.8 Tip artifacts

A last effect of tip shape influence is recognized in the apparent generation of new features on the scanned surface. This is nothing different from the convolution phenomena discussed in the two previous paragraphs, but affects imaging in a different way. In fact distortion is not a simple dilation of scanned geometries or a non-sampling of surface regions, but it exploits with the generation of repeating patterns in the imaged topography. This happens in particular when features on the measured surface are much smaller than the probe: in this case a sort of inversion of roles takes place. This means that the measuring process can be thought as the surface features operating the scan over the tip. Thus the shape of the tip is reproduced over the scanned area a number of times which is correspondent to the number of small features that have performed an "inverted scan" over the tip. This is clearly shown by Figure 3.12a, where a sort of nano-foot-shaped structure is reproduced 3 times within the surface topography. A close look to the nano-foot and software investigations (such as a cross-correlation analysis) put in evidence that those features are highly correlated. This should be an alarm bell for the user: a scan on a tip characterizer sample can then provide a tip reconstruction, necessary for a proper interpretation of measured topographies or artifacts.

Typically tip contaminations or fractures are the main causes for those artifacts; use of new tips is the solution for avoiding this disturb.
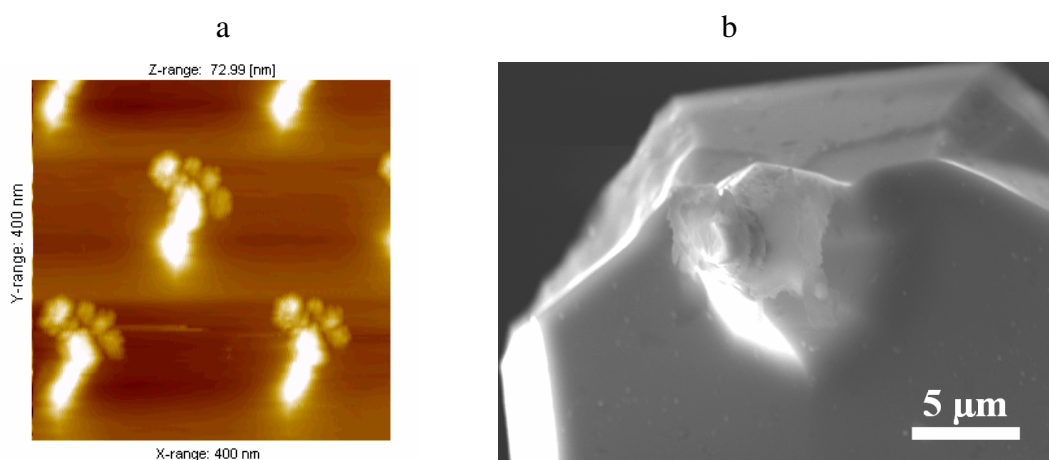

Figure 3.12: a) Nano-foot-shaped structure due to tip fracture, and b) a SEM image of a contaminated tip.

3.3.9 Drift

Drift is the gradual uncontrolled movement of the system over time. It is not easy to uniquely define sources of drift, but most probably one of the primary causes has to be ascribed to changes in temperature and in temperature gradients. Most microscopes are covered and many are insulated or placed in a temperature-controlled environment, but anyway it is difficult to achieve drift to velocities lower than 10 nm/h. This means that uncontrolled relative movements between the tip and the surface occur, with a speed in the order of a nanometer per minute. This distortion is almost insignificant for a measurement carried out in a range of some micrometers: in fact in this case the error is in the order of 1 ‰ or less. Conversely drift results heavily distorting when high resolution imaging is achieved by taking many profiles (i.e. a long scan operation) in the nanometer scale: in this case errors in the order of some percent can indeed affect measurement. This is of concern also in closed loop scanners, whereas tip position is controlled with respect to a reference frame, while the sample is not.

Drift effects should be conveniently described by considering both short term and long term effects. Thermal drift determines distortion in the single image. In a longer time scale, after a few probe relocations, thermal drift results in net probe offset from the nominal position. In the following thermal distortion affecting single images will be referred as short term thermal drift. Long term thermal drift is considered to be the net probe motion relative to indicated position after the time required to take at least two images.

As already stated, drift is a time-dependant distortion, affecting tip positioning in the lateral as well as in the vertical plane. Initial drifts, e.g. after the instrument has been switched on, usually exhibit an exponential decrease, stabilizing after a warm-up period that is usually in the range of 10-60 minutes. A helpful simplification is achieved dividing drift into its horizontal and vertical components: d_x, d_y and d_z. In Figure 3.13 it is possible to appreciate two measurements affected respectively by horizontal and vertical drift. In the first one, a triangular repetitive pattern measured with an extremely low scan rate is reported. Drift is recognizable as a variable misalignment producing relative shifts of profiles in the x direction (i.e. the fast scan direction). Drift is continuously affecting scan operation, but it is someway discretized during the measurement process: in fact when the tip is positioned for beginning scan of the n-th profile, a positioning error occurs, given by the whole amount of drift accumulated during trace and retrace of the (n-1)-th profile. Recognizing horizontal drift distortions within single profiles is very difficult, often impossible; therefore it has to be considered as a stochastic error affecting single pixels position. The second measurement in Figure 3.13 reproduces the result of a scan on a silicon flat, affected by an evident distortion due to vertical drift. The distortion is recognizable

as a variable misalignment producing relative shifts of profiles in the z direction. Once again the topography shows a sort of discretization of the drift: shifts between two subsequent profiles are in fact the result of the total drift "accumulated" during one trace and one retrace scan operation.
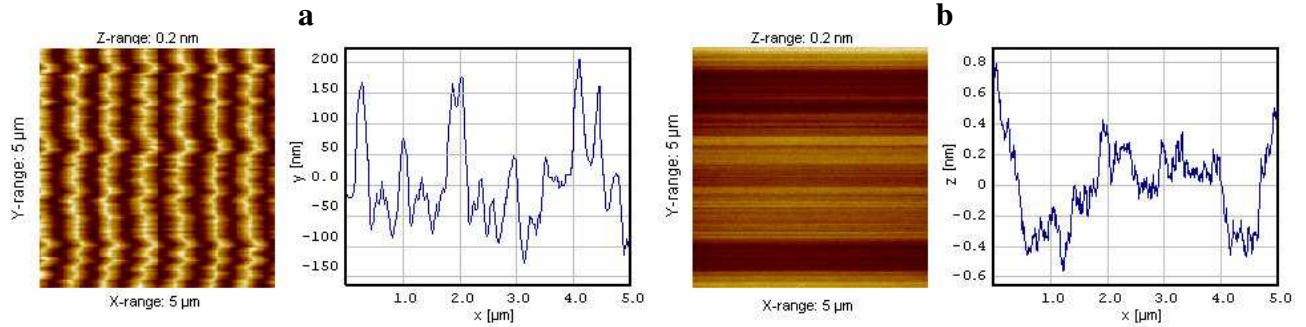

Figure 3.13: Surface topographies affected by horizontal and vertical drift: in the graphs relative shifts respectively in the y and z direction are reported. In case of drift-free scanning, graphs would report a straight line.

A mathematical model can be introduced for describing drift [48]. Assuming that the imaging process leads only to constant velocity drift deformations, and considering that drift velocities are known to be free of rotational components [49], the following equation can be written (3.12):

$$\begin{bmatrix} x \\ y \\ z \end{bmatrix} = \begin{bmatrix} x' \\ y' \\ z' \end{bmatrix} - \begin{bmatrix} d_x \cdot t \\ d_y \cdot t \\ d_z \cdot t \end{bmatrix} \tag{3.12}$$

where t is the time elapsed from the beginning of the scan to the measurement of the pixel lying in the position (x,y). By indicating the scanning velocity as v_x (in the fast scan direction), the number of pixels with N ($Nx = Ny = N$), the scanned range with L_x and L_y, the time interval can be also expressed through (3.13):

$$t = \frac{2 \cdot L_x \cdot y \cdot (N-1)}{L_y \cdot v_x} + \frac{x}{v_x} = \frac{2 \cdot L_x \cdot y \cdot (N-1) + L_y \cdot x}{L_y \cdot v_x} \tag{3.13}$$

As already stated this model doesn't consider deviation of drift velocity from the mean value: these deviations will be therefore considered as contributes of the uncertainty affecting x, y, z positioning.

A measuring procedure to get rid of vertical sensor drift, applicable to non flat surfaces, will be discussed in Paragraph 5.2.

3.3.10 Noise

Atomic Force Microscopy is affected by noise, originating from different sources: electrical, acoustical, vibrational or mechanical. Its effect is usually a stochastic disturb, often dominating the high spatial frequency ends of scanned topographies. In Figure 3.14b a noisy measurement is

proposed, together with the Fourier Transform of a profile traced in the middle of the scan. The red circle indicates the high frequency region, where Fourier spectrum is mainly indicative of noise distortions.
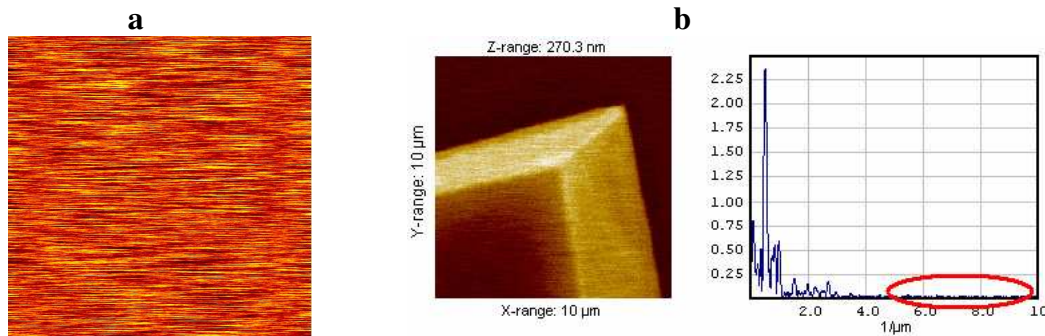

Figure 3.14: a) Example of noise investigation by the non-scanning method on a glass surface. b) Noisy measurement and Fourier Transform: noise characteristic area is red circled in the spectrum.

A practical method for investigating and quantifying noise is the non-scanning-method ('standstill' measurement). In this mode the scanning probe is kept over a flat and stable sample. without performing any lateral scanning movement. The measurement signal is captured, with the time signal being transformed into an apparent spatial signal (Figure 3.14a). From the signal, a noise equivalent Power Spectral Density PSD can be calculated by applying the respective time/length conversion factor. This analysis is helpful when imaging the actual sample, since it allows distinguishing between instrument noise and the actual roughness of the sample [37].

Noise can't be avoided during measurement. A proper insulation system, and appropriate setting of scan parameters can help for a reduction of the disturb. Filtering operation are commonly implemented for attenuating or eliminating noise during data processing, but these operation often leads to loss of information on the measured topography.

3.3.11 Filtering

Before data from AFM measurement can be analyzed, it is usually necessary to do some pre-processing, such as filtering or leveling operations.

With regard to filtering usually three operations are carried out: statistical filtering, Fourier filtering and outliers filtering.

Statistical filtering includes noise removal using statistical methods like averaging, median filtering (for spikes) or conservative noise reduction. More details on statistical filters are given in Appendix B.

Fourier filtering is often used for frequency-dependent reduction of noise and removal of some parasitic frequencies from data in the fast scan direction [37].

The outliers filtering is a tool often implemented in commercial software, allowing for detection and elimination of outliers, as dust particles, unwanted features or artifacts. Regions are subsequently resampled, filling in the most probable values, as for example by interpolation of neighboring pixels.

Three examples of drastic filtering are reported in Figure 3.15, highlighting the problems connected with this kind of data pre-processing.

Fourier filtering reduced noise contribute, allowing also for an elimination of the artifact on the bottom of the image (a dust particle, recognizable as a white rather big spot). But a close look to the surface shows that a bad use of the filter isolated a dominating wavelength, leaving on the surface a sort of periodical bump pattern.

A different situation was instead generated by the Gaussian filtering. The dust artifact was moderately smoothed, and even noise is strongly reduced, but on the other hand a general loss of definition can be noticed, together with a blurry effect appearing all over the image.

The horizontal interpolation had no effect on the noise level, but provided an elimination of the dust particle. This operation improves the general appearance of the scanned topography, but is someway misleading. In fact the interpolation performed on the processed area, didn't add "true points" to the data set, but only virtually resampled the topography guessing new points. Clearly interpolation is not a recommendable operation and in general from a metrological point of view is not acceptable, in particular when wide areas need resampling.
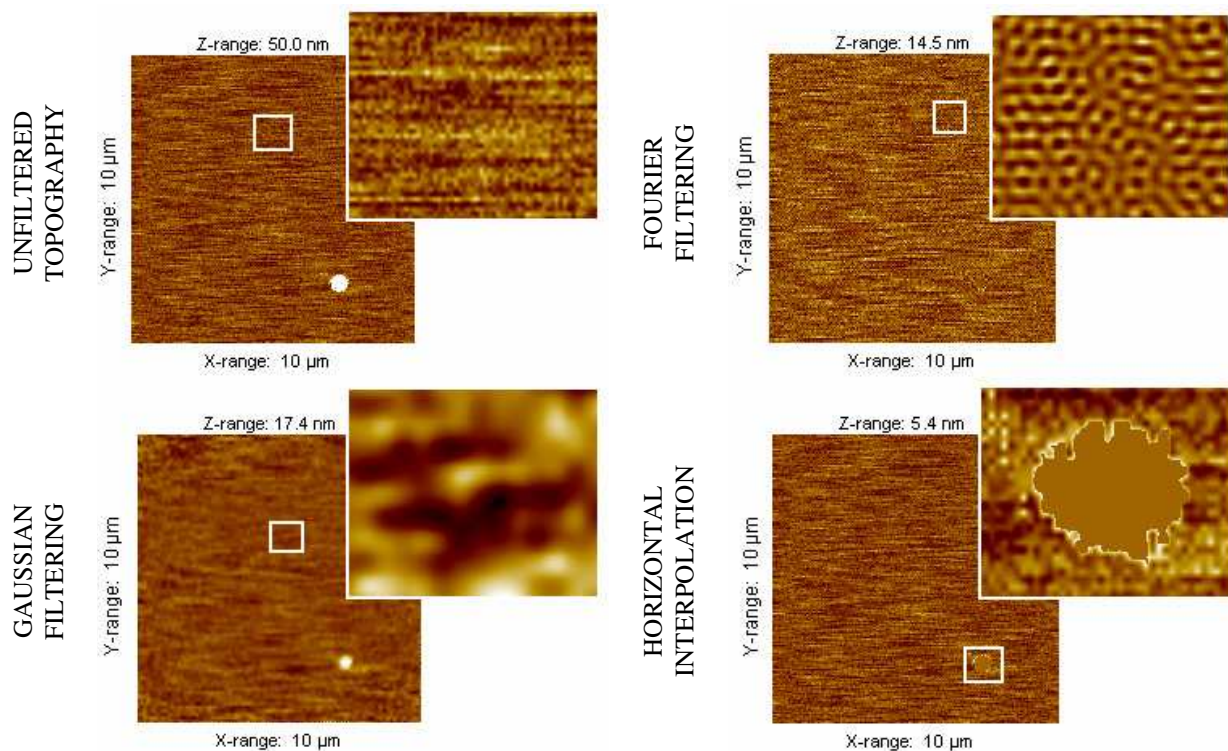

Figure 3.15: Effects of filtering on an AFM measurement.

3.3.12 Leveling

A typical software operation performed on AFM measurements is data leveling. The aim of this correction is to remove the installation slope, i.e. the tilt occurring between the microscope x-y scanning plane and sample surface. This tilt is typically lower than 5°, but accurate sample positioning can reduce the tilt to angles lower than 1°. It is worth to note that in some case this angle can exceed 15-20°, especially when characterizations are needed on steep slopes or on regions non completely accessible from the top. Two typical examples are the surface topographies reported in Figure 3.11: in that case a clockwise rotation can in fact help the measure of the sidewall.

When tilt has to be removed from scanned topographies, usually compensation is carried on, through a simple leveling algorithm. Routines implemented in commercial software generally compute the mean plane best fitting measured data and subtract that plane from the individual data. This procedure is not correct, since introduces two distortions: the cosine error and a deformation of the surface topography.
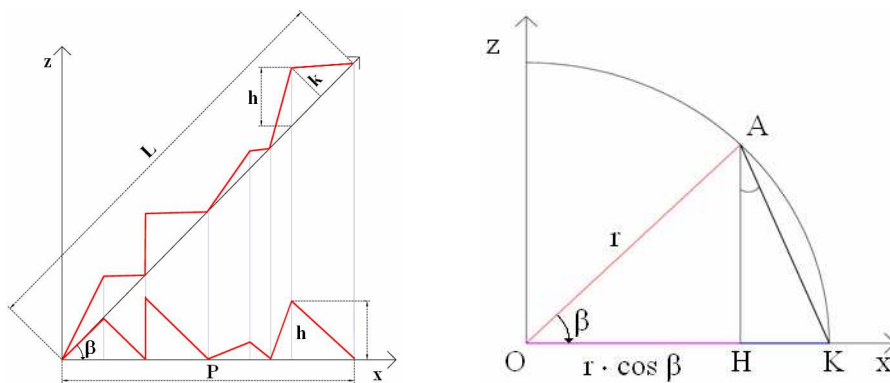
Figure 3.16: Representation of the cosine error, connected with the best fitting plane subtraction [50].

Both the distortions are clearly seen in Figure 3.16, where L represents the scanned range, β the surface tilt, k the actual height of a given feature and h the distorted height of the same feature, after simple projection. During plane subtraction, a sort of projection takes place, and the total dimension of the topography is shrunk. With refer to Figure 3.16, this can be explained through analysis of segment OA: its projection OH is shorter by the length HK, with an average error that is proportional to (1- cos β). For each pixel, this distortion is proportional not only to the x coordinate, but also to its elevation (i.e. the local height). For this reason the distortion occurring during plane subtraction is not constant, and a local change in the topography shape takes place. This phenomenon is reproduced by the deformations affecting the triangular structures in Figure 3.16.

The mathematical models describing rotation (3.16) and projection (3.17) give evidence to the difference. In three dimensions, a rotation can be defined by three Euler angles, (α, β, γ), or by a single angle of rotation, θ with the direction of a unit vector $v(v_x, v_y, v_z)$, about which to rotate. The matrix to rotate a column vector in Cartesian coordinates about the origin is:

$$\begin{bmatrix} x' \\ y' \\ z' \end{bmatrix}_r = \begin{bmatrix} \cos\beta\cos\gamma & \sin\alpha\sin\beta\cos\gamma - \cos\alpha\sin\gamma & \cos\alpha\sin\beta\cos\gamma + \sin\alpha\sin\gamma \\ \cos\beta\sin\gamma & \sin\alpha\sin\beta\sin\gamma + \cos\alpha\cos\gamma & \cos\alpha\sin\beta\sin\gamma - \sin\alpha\cos\gamma \\ -\sin\beta & \sin\alpha\cos\beta & \cos\alpha\cos\beta \end{bmatrix} \cdot \begin{bmatrix} x' \\ y' \\ z' \end{bmatrix} \quad (3.14)$$

or:

$$\begin{bmatrix} x' \\ y' \\ z' \end{bmatrix}_r = \begin{bmatrix} \cos\theta + (1-\cos\theta)v_x^2 & (1-\cos\theta)v_xv_y - (\sin\theta)v_z & (1-\cos\theta)v_xv_z + (\sin\theta)v_y \\ (1-\cos\theta)v_xv_y + (\sin\theta)v_z & \cos\theta + (1-\cos\theta)v_y^2 & (1-\cos\theta)v_yv_z - (\sin\theta)v_x \\ (1-\cos\theta)v_xv_z - (\sin\theta)v_y & (1-\cos\theta)v_yv_z + (\sin\theta)v_x & \cos\theta + (1-\cos\theta)v_z^2 \end{bmatrix} \cdot \begin{bmatrix} x' \\ y' \\ z' \end{bmatrix} \quad (3.15)$$

where x', y' and z' are the measured coordinates and subscript "r" indicate the "*rotated matrix*", i.e. the new coordinates after compensation of tilt.

A simplification of the model brings to:

$$\begin{bmatrix} x' \\ y' \\ z' \end{bmatrix}_r = \begin{bmatrix} \cos\beta & \sin\alpha\sin\beta & \cos\alpha\sin\beta \\ 0 & \cos\alpha & -\sin\alpha \\ -\sin\beta & \sin\alpha\cos\beta & \cos\alpha\cos\beta \end{bmatrix} \cdot \begin{bmatrix} x' \\ y' \\ z' \end{bmatrix} \quad (3.16)$$

Where:

- α and β represent the correction angles, evaluated in an counterclockwise system respectively around x and y axis (see Figure 3.16);

- rotation relative to z axis γ was set to zero.

On the other hand, projection can be expressed as:

$$\begin{bmatrix} x' \\ y' \\ z' \end{bmatrix}_r = \begin{bmatrix} 1 & 0 & 0 \\ 0 & 1 & 0 \\ 0 & 0 & 1 \end{bmatrix} \cdot \begin{bmatrix} x' \\ y' \\ z' \end{bmatrix} + \begin{bmatrix} 0 & 0 & 0 \\ 0 & 0 & 0 \\ -\sin\beta & \sin\alpha & 0 \end{bmatrix} \cdot \begin{bmatrix} x' \\ y' \\ z' \end{bmatrix} = \begin{bmatrix} 1 & 0 & 0 \\ 0 & 1 & 0 \\ -\sin\beta & \sin\alpha & 1 \end{bmatrix} \cdot \begin{bmatrix} x' \\ y' \\ z' \end{bmatrix} \quad (3.17)$$

Evidently the difference between the two expressions (3.15) and (3.17) is negligible when the tilt angles tend to zero. As a consequence, plane leveling is only applicable for correcting small tilts, while in general the right procedure would be the implementation not of a projection but of a real topography rotation. This concept will be recalled also in Paragraph 6.2.

Sometimes surface topographies are leveled even more dramatically, for example each profile of the scan (measured within the fast scan direction) can be adjusted with respect to adjacent lines with a given criterion. This approach is not much unusual, since AFM images should be regarded as collections of parallel profiles rather than three dimensional images [51], and in fact is in practice very useful for low frequency noise and scanner artifact compensation. However the

disadvantage is that the uncertainties in the slow scan direction are increased, as the software compensation is not supported by real measurement, such as traceable scanners or interferometric devices.

Correction of single profiles (implemented in commercial SPM software and also in SPIP™ with the name *Line Wise Leveling*) is in general applicable to images of flat surfaces generating minor distortions and introducing minor contributes of uncertainty: bigger problems are encountered when the shape in the slow scan direction is relevant for the characterization of the topography. An example of the effect of the single profiles leveling is given in Figure 3.17, where a spherical topography is distorted into a cylindrical shape.

However, a measuring procedure to get rid of vertical sensor drift, applicable to non flat surfaces, will be discussed in Section 5.2.
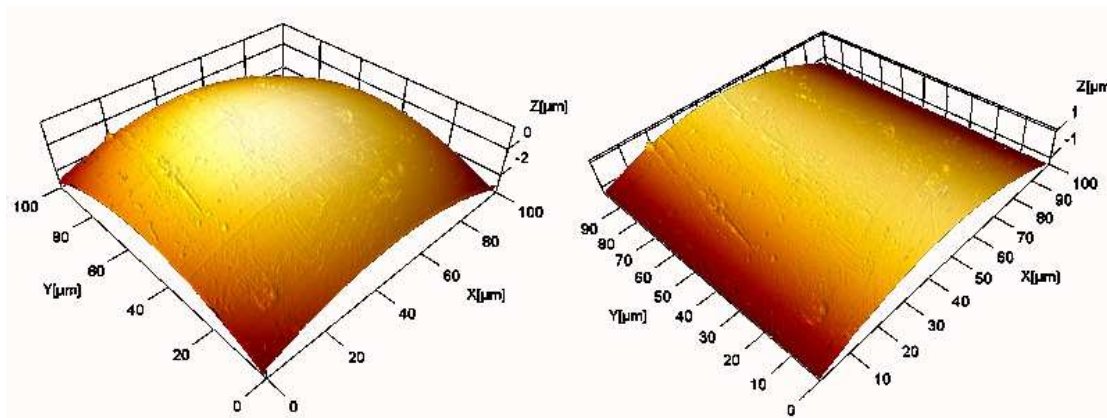
Figure 3.17: Single profiles leveling applied to a spherical surface generates a cylindrical topography.

3.4 Complete mathematical model

In this paragraph a complete mathematical model for correction of Atomic Force Microscopy data sets is presented. This model is achieved assembling all the single contributes discussed and presented in the previous paragraphs:

- scaling (3.1);

- orthogonality (3.4);

- non-linearity (3.6 and 3.7);

A more detailed model will also consider:

- tilt and bow (3.14, 3.15 and 3.7);

- drift (3.12);

- tip convolution (3.10 and 3.11).

In order to better clarify the model, basic assumptions are here briefly repeated.

Let $i = 1, \ldots, m$, and $j = 1, \ldots, n$ be indices of the scanned pixels in a matricial representation (see Paragraph 3.2), and n, m be the number of indices (i.e. respectively the number of pixels per line and the number of scanned profiles) [52] [53].

Let's consider the microscope at reference conditions, in equilibrium with environment. At these reference conditions the sampling points during scanning can be described as an *oblique coordinate system:*

$$z'(i, j) = z'(x_i', y_i') \tag{3.18}$$

where z', and x_i', y_j' are the vertical and lateral positions in the z', x' and y' direction which would be displayed by the microscope at the reference conditions, with the dimensions length. This reference coordinate system will be referred to as the "microscope coordinate system" and an apostrophe ' will indicate that the basis for a coordinate set is the coordinate axes of the microscope coordinate system.

A single line ($j = 1$) is named a profile $z'(x_i')$.

In order to simplify the notation, the discrete values of the lateral position, x_i' and y_j' are substituted with only x' and y' and redefined as a continuous variable. This is of help when, for example, analysis is done at sub pixel level.

The purpose is to find a transformation of the displayed and uncorrected z' topography $z'(x', y')$ into a metric coordinate system.

As stated also by [52], the physical and the true z-coordinate for the same topography are expressed as $z(x', y')$. If the physical z-coordinate $z(x', y')$ is a single valued function of the uncorrected z-coordinate $z'(x', y')$ and the position x', y', then the physical z-coordinate can be expressed as $z(x', y', z(x', y'))$.

In this context, single valued function is used to point out the difference to a multi-valued function. In fact for a piezo-actuator that exhibits hysteresis and creep the position of the tip as function of the control signal (typically the voltage applied to the piezo-scanner) is a multi-valued function. Therefore several positions are possible for a given control signal, depending on the "history" of the control signal applied.

The immediate consequence is that, for each tern of uncorrected z-coordinate $z'(x', y')$ and position x', y' there is one and only one position of the tip, that is only one physical z-coordinate $z(x', y')$. This means that the AFM system, including the readings from the position sensors, can be described as having no significant time-dependent creep and constant hysteresis distortions.

The purpose is now to find an expression in $(x', y', z'(x', y'))$ that will give a corrected z-coordinate $z(x, y)$. The full mathematical model can be expressed as:

$$
\begin{bmatrix} x \\ y \\ z \end{bmatrix} = \begin{bmatrix} c_{xx'} & c_{xy'} & c_{xz'} \\ c_{yx'} & c_{yy'} & c_{yz'} \\ c_{zx'} & c_{zy'} & c_{zy'} \end{bmatrix} \cdot \begin{bmatrix} x' \\ y' \\ z' \end{bmatrix} + \begin{bmatrix} c_{xx'2} & c_{xy'2} & c_{xz'2} & c_{xx'y'} & c_{xx'z'} & c_{xy'z'} \\ c_{yx'2} & c_{yy'2} & c_{yz'2} & c_{yx'y'} & c_{yx'z'} & c_{yy'z'} \\ c_{zx'2} & c_{zy'2} & c_{zz'2} & c_{zx'y'} & c_{zx'z'} & c_{zy'z'} \end{bmatrix} \cdot \begin{bmatrix} x'^2 \\ y'^2 \\ z'^2 \\ x'y' \\ x'z' \\ y'z' \end{bmatrix} +
$$

$$
+ \begin{bmatrix} c_{xx'3} & c_{xy'3} & c_{xz'3} & c_{xx'2y'} & c_{xx'2z'} & c_{xx'y'2} & c_{xx'z'2} & c_{xx'y'z'} \\ c_{yx'3} & c_{yy'3} & c_{yz'3} & c_{yx'2y'} & c_{yx'2z'} & c_{yx'y'2} & c_{yx'z'2} & c_{yx'y'z'} \\ c_{zx'3} & c_{zy'3} & c_{zz'3} & c_{zx'2y'} & c_{zx'2z'} & c_{zx'y'2} & c_{zx'z'2} & c_{zx'y'z'} \end{bmatrix} \cdot \begin{bmatrix} x'^3 \\ y'^3 \\ z'^3 \\ x'^2y' \\ x'^2z' \\ x'y'^2 \\ x'z'^2 \\ x'y'z' \end{bmatrix} + \sigma \begin{bmatrix} x'^3 \\ y'^3 \\ z'^3 \\ x'^2y' \\ x'^2z' \\ x'y'^2 \\ x'z'^2 \\ x'y'z' \end{bmatrix} \quad (3.19)
$$

and using the compact notation:

$$
M_{xyz} = C^{(1)}_{xyz} \cdot M'^{(1)}_{xyz} + C^{(2)}_{xyz} \cdot M'^{(2)}_{xyz} + C^{(3)}_{xyz} \cdot M'^{(3)}_{xyz} + \sigma\left(M'^{(3)}_{xyz}\right) \quad\quad\quad (3.20)
$$

where the number on brackets indicates the power order of the correction and σ indicates the higher order residual (Peano residual term). The contribute of σ should have to be considered whenever an uncertainty budget is evaluated with regard to quantitative AFM measurements. The same uncertainty budget will of course consider all the distortions that, due to their non-systematic nature, are not considered by the correction model (3.19).

This complex formulation will be seldom applied for instrument calibration: in fact evaluating single calibration coefficients is definitely not an easy. Anyhow it is in the author belief that a complete mathematical model constitutes a good reference point for people involved in AFM metrology. The model can be used also to define an order of priority on calibration tasks: fine definition of third order coefficients is in fact incomplete whenever second order coefficients are not properly evaluated. Secondly $\sigma\left(M'^{(n)}_{xyz}\right)$ should have to be compared with the number of uncorrected distortions affecting atomic force microscopy, deciding as a result the appropriate order n. High orders (n>2) are in fact meaningful and useful only whenever other source of errors (such as drift or tip convolution) are sufficiently low.

Assumed the x axis to be coincident with the fast scan direction (x') and the x-y plane to lay on average x'-y' plane, the matrix $C^{(1)}_{xyz}$ simplifies as follows:

$$\begin{bmatrix} c_{xx'} & c_{xy'} & c_{xz'} \\ 0 & c_{yy'} & c_{yz'} \\ 0 & 0 & c_{zy'} \end{bmatrix} \qquad (3.21)$$

A more detailed expression is achieved introducing drift and tip convolution effects:

$$\begin{bmatrix} x \\ y \\ z \end{bmatrix} = \left(C_{xyz}^{(1)} \cdot M_{xyz}'^{(1)} + C_{xyz}^{(2)} \cdot M_{xyz}'^{(2)} + C_{xyz}^{(3)} \cdot M_{xyz}'^{(3)} \right) - \begin{bmatrix} d_x \cdot t \\ d_y \cdot t \\ d_z \cdot t \end{bmatrix} \Theta\, P \qquad (3.22)$$

And introducing rotation (for correction of installation slope):

$$\begin{bmatrix} x \\ y \\ z \end{bmatrix}_r = \begin{bmatrix} \cos\alpha\cos\beta & \sin\alpha\cos\beta & -\sin\beta \\ -\sin\alpha & \cos\alpha & 0 \\ \cos\alpha\sin\beta & \sin\alpha\sin\beta & \cos\beta \end{bmatrix} \cdot \begin{bmatrix} x_c \\ y_c \\ z_c \end{bmatrix} \qquad (3.23)$$

where x_c, y_c and z_c indicate coordinates corrected through (3.22) and subscript "*r*" stands for "*rotated matrix*".

3.5 Conclusions

Through this chapter sections, typical AFM source of errors are described, mainly arising from the scanning system, the probe, the environment and from data processing subsequent to measurement. When possible, distortions are described through a mathematical model: all contributions are eventually unified in a single reference model, which in principle completely describe AFM scanning.

3.5.1 Contributions

A grateful acknowledgement is given to Dr. Anders Kühle (DFM, Dansk Fundamental Metrologi A/S) and Prof. Mario Pitteri (Department of Mathematical Methods and Models in Applied Sciences, University of Padua) for useful discussions in connection with topics discussed in the present chapter.

Chapter 4

AFM Calibration

4.1 Introduction

Today Scanning Probe Microscopy (SPM) is a key measuring technology for different tasks, including research, development and quality control in industrial companies. The increasing need not only for qualitative, but also for quantitative analysis is consequently a driving force in the development of traceable measurements.

Some metrological Atomic Force Microscopes (AFMs) have established traceability by using, for example, built-in laser interferometers on the axes. However, most instruments need calibration operations on standards [54] [55] [56] [57].
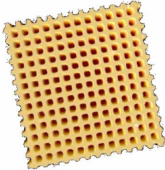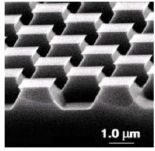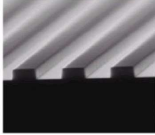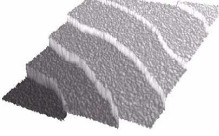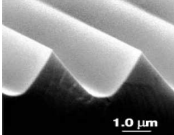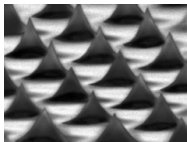
Quite a number of calibration standards are available on the market or have been realized by several research groups: they generally embody simple geometries, with 1D or 2D line gratings of given mean pitch [58].

The design of standards is generally related to their purpose and limited by available manufacturing techniques. Some standards cover only one aspect of calibration (e.g. tip characterizers) others cover several (e.g. waffle gratings) some provide information relative to a restricted measuring range (e.g. step heights) while others provide information concerning the full working range (e.g. flatness standards).

The standards normally applied for the calibration of AFMs can be classified into four groups, based on what they are used for: lateral, vertical and orthogonality calibration, and performance tests [59] [60] (Table 4.1).

This chapter focuses on calibration. In the first part optical fibers are proposed for the realization of new calibration artefacts and afterwards their application is described for completion of lateral and vertical calibration. Finally the development and implementation of a software tool is proposed, allowing for characterization and correction of z to x-y plane orthogonality error.

Table 4.1: Classification of the most commonly used standards for the calibration and verification of AFMs [60] [61] [62].

	Axes	Standard	Used for	Expected parameters
LATERAL CALIBRATION	X-Y	waffle	calibration of X,Y	Scaling factors $c_{xx'}$, $c_{yy'}$
			x-y orthogonality	$c_{xy'}$
		chessboard-like grating	non linearity	Higher order calibration coefficients
VERTICAL CALIBRATION	Z	step height	calibration of Z	Scaling factor $c_{zz'}$
		monoatomic silicon steps	non linearity	Higher order calibration coefficients
ORTHOGONALITY CALIBRATION	X-Z Y-Z	triangular steps	x-z and y-z orthogonality	$c_{xx'z'}$, $c_{yy'z'}$
PERFORMANCE TEST	X,Y,Z	silicon flat	Flatness	Higher order calibration coefficients $c_{zx'^2}$, $c_{zy'^2}$
		inverted tip	Tip characterization	Tip radius R and tip cone angle α

4.1.1 Horizontal axes

One and two-dimensional gratings with various rectangular patterns are available for horizontal axes calibration in Scanning Probe Microscopy. These gratings generally report structures periodically arranged, with wavelengths ranging from a tenth of micron to 10µm [58]. Usually the structures have reduced heights (<100 nm) in order to reduce crosstalk distortions occurring during vertical movements. Several techniques are implemented for their manufacturing. A classification of the main calibration standards for lateral calibration is reported in Table 4.2.

Table 4.2: Main lateral calibration standard [37] [55]

Pitch dimension	Manufacturing Technology	Notes
>200 nm	lithographic or holographic techniques	good rectangularity and homogeneity over large areas [63]
50-200 nm	e-beam lithography	[55] [63]
<50 nm	cleaving and etching of growth semiconductor heterostructures	[63]
<1 nm	crystalline surfaces of graphite (HOPG), gold or silicon	Ideal for angle measurements; atomically plane single crystal surfaces over wide areas [64]

Traceable calibration of those standards is ensured by means of different instruments. X-ray reflectometry is suitable for some of the smallest structure; instead optical diffraction techniques can provide accurate results when averaging is performed over large areas on periods greater than 250 nm, even if inhomogeneities are not revealed. Lateral standards with topographical structural spacing of less than 250 nm can at present be calibrated only with metrological SPMs. The calibration procedure of the scanner should comprise different orientations of the standard, in order to provide information needed both for the scale and for orthogonality. Main spacing of gratings evaluated through the instrument are compared with reference values in order to calculate calibration coefficients. Lattice constants are extrapolated through software analysis, generally based on Fast Fourier Transform or using gravity centre techniques [35].

4.1.2 Vertical axis

Common practice usually makes use of step heights; different samples covering different heights are usually applied to verify instrument performance, with ranges from 6 nm to 2400 nm [37]. Most step-height standards are made from silicon or silicon oxide. The steps are lines or two-

dimensional rectangular patterns, are calibrated in accordance with ISO 5436 [65] using interference microscopes, stylus instruments or metrological SPMs and realizing expanded uncertainties down to 1 nm. Monoatomic step-height standards have also been produced on silicon crystalline surfaces, with dimensions down to a tenth of nanometer.

An alternative method for step height evaluation, with results coherent with the previous one, is through the heights distribution histogram, in agreement with ISO 4287 [66].

The main limitation connected with use of step-height standard is the fact that calibration is performed only on a small part of the whole vertical measuring range. As a consequence a proper characterization of the non-linear behavior of the whole instrument vertical range can be carried out only by using different calibrated step heights, or shifting one step height standard shifted several times in the vertical direction, using a wedge or a laser interferometer [52] [67] [68].

Attention has also to be paid to cantilever movements, which often have an important role in the vertical calibration of the instrument.

4.1.3 Novel standards

Atomic force microscopes, and more in general the whole family of scanning probe microscopes, cover a wide range of industrial as well as research metrological needs. Measurements are in fact carried out on a lot of different engineered surfaces, taking advantage of the whole performance of the instrument, included the full measuring range. For this reason a calibration performed on a flat surface or on a single step height standard can be somehow limiting, and efforts are being done to produce samples that allow for calibration in the whole measuring volume [37].

Micrometer sized structures constitute the new generation of calibration standards, allowing for calibration not only of SPMs, but also of other instruments for surface characterization at the microscale, as for instance optical based profilometers, nano-CMM or 3D-SEM. By way of example micro-pyramids, with terraces, slopes and reference nanomarks have been produced and applied for AFM calibration (Figure 4.1a) [69]. Differently from step heights or gratings, these samples allow for characterization of the instrument in terms of vertical, horizontal and orthogonal performance, while limitations mainly deal with a need of more sophisticated image analysis software.

From the author's point of view, a great opportunity is given by the nanoparticles properties. High quality micro- and nano-spheres are in fact already produced, and organized in complex structures, as for example demonstrated by Figure 4.1b. The possibility of precisely controlling arrangement of those particles, can help for production of calibration standards "on demand" that provide a solution to all the different instruments calibration needs.
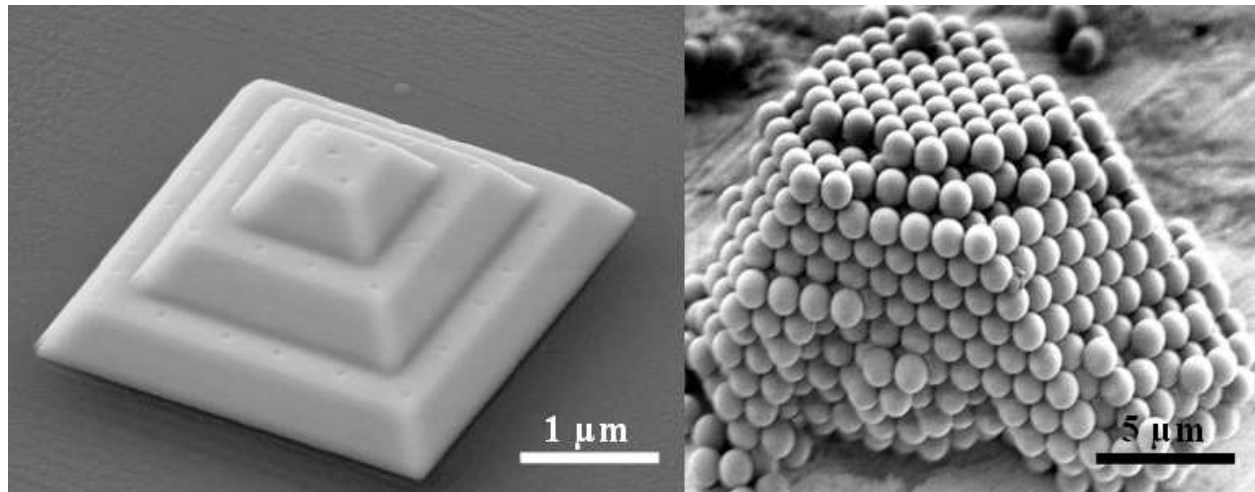
Figure 4.1: The SEM images give examples of 3D structures: a) a pyramid with landmarks [69] and b) assembled 1.5 µm silica beads [70].

4.2 Optical Fiber Technology

In the following sections we will discuss the possibility of using high precision cylindrical artefacts for calibrating AFM scanners.

Fiber optic technology was selected and applied for new calibration standards engineering and realization [71]. In fact, due to IT demands, fibers manufacturing process has taken great steps forward, reaching very high quality levels (in terms of non-circularity and roughness and the highest repeatability) in parallel with relative low costs.

There are two main types of optical fiber: single-mode and multimode. Both types of fiber are composed of two basic concentric glass structures: the core, which is responsible for carrying the light signals, and the cladding, which confine the light in the core [72].

Single-mode fibers were preferred for the present application, since they usually ensure more regular geometries, with incredibly low tolerances at a low price.

Single-mode fibers consist primarily of silica with typically only small amounts of germania. Three chemical vapor deposition methods are usually applied for manufacturing of the pure glass preform: inside vapor deposition, outside vapor deposition, or vapor axial deposition. As most optical fibers nowadays fabricated, the high precision fibers used within this study were produced through chemical vapor axial deposition. These are produced by pulling from a so-called preform in a fiber drawing tower, an apparatus which is typically several meters high. The preform is a glass rod with a few centimeters diameter and roughly one meter length.

When heated close to the melting point in a furnace at the top of the drawing tower, the preform allows pulling a thin fiber out of the bottom side of the furnace. The fiber from a single preform can be many kilometers long. During the pulling process, the furnace has controlled atmosphere

and temperatures held between 1900 and 2200°C. The fiber is than moved onto a controlled spool, which spool slowly pulls the fiber from the preform by a tractor mechanism. Laser-based diameter gauge are used to monitor the diameter of the fiber, and to regulate the rate the tractor pulls on the thread [72].

In the table below product specifications of some single mode fibers available on the market are reported (Table 4.3).

Table 4.3: Specifications of some single mode optical fibers available on the market ([73] [74] [75] [76]).

Specifications / Manufacturer	Diameter [µm]	Diameter Uncertainty	Non circularity $\left(1 - \dfrac{D_{min}}{D_{max}}\right) \times 100$
OFS	125	±0.7	<1.0%
Corning	125	±0.7	<0.5%
tyco (AMP)	125	±1.0	<1.0%
Belden	125	±0.3	<0.3%

4.2.1 Development of new calibration standards

Quite a number of calibration standards based on very different materials, geometries and accuracies is already available on the market or have been realized by several research groups.

What's innovative in the new developed artefacts is their flexibility: they can be applied in principle to calibration of most of the contact or non-contact instruments for characterization of surface topographies and micro geometries, such as micro- or nano-CMMs, optical based instruments and of course scanning probe microscopes. The new calibration standards, based on optical-fibers technology, cover an interesting metrology range, allowing for horizontal and vertical calibration from the micro to the millimeter dimension.

The new calibration standards have the appearance of series of cylinders embedded in a polymeric matrix or pasted on a flat surface. The solution proposed in Figure 4.2a and Figure 4.2b is meant for both vertical and lateral calibration [77], while the solution reported in Figure 4.2c was expressly realized for vertical calibration [78]. Implementation of these artefacts is more extensively described in the following paragraphs (Section 4.3 and 4.4).

A new class of prototype calibration standards has also been realized, with aspect-ratios higher than 10:1 (Figure 4.3). These reproduce a miniature of calibration standard used in the field of Coordinate Measuring Machines (CMMs), and in fact were more specifically developed for nano-CMM calibration [79]. The solutions here reproduced are only indicative of the feasible

structures: different dimensions and different arrangements are possible, using for example larger or thinner fibers [80].
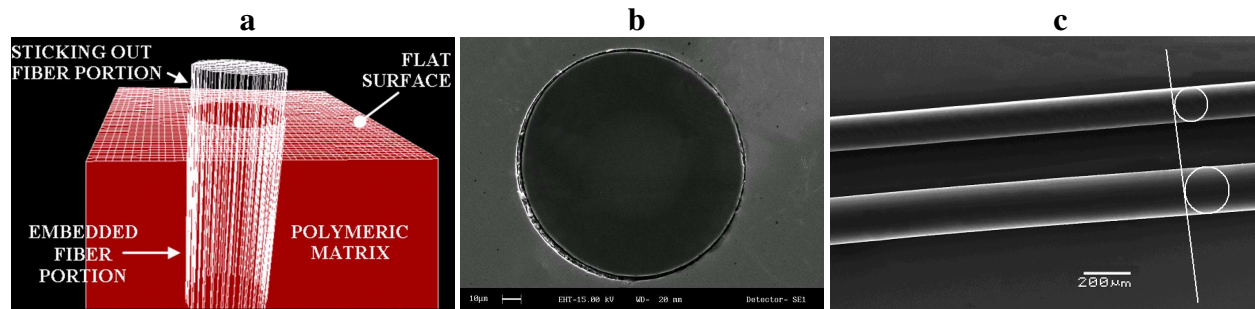

Figure 4.2: Schematic (a) and SEM image (b) of the sample designed for horizontal and vertical calibration. In (c) fibers are applied for realization of a standard for "complete" vertical calibration.
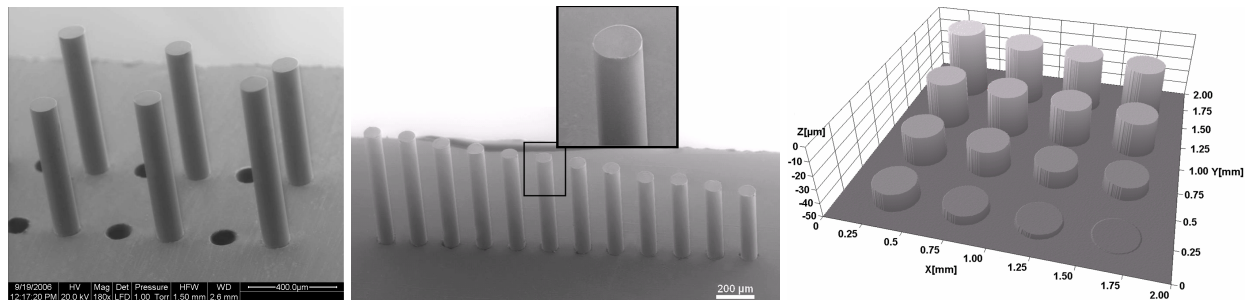
Figure 4.3: High aspect ratios samples realized by means of optical fibers.

4.3   Horizontal calibration

The new standard, based on the fiber optic technology, is here used for completing horizontal calibration [77].

The fiber, embedded in a polymeric matrix, after fine polishing has the appearance of a ~1µm height and 125 µm diameter cylinder sticking out of a flat surface (Figure 4.2a). Smaller fibers (such as 80 µm or 30 µm diameters) can also be applied whenever smaller samples are needed.

4.3.1 The calibration principle

A mathematical model for the description of an AFM measuring system was reported in the previous chapter (Paragraph 3.3.1, 3.3.2 and 3.4). A simplification can be introduced to Equations (3.1) and (3.4), limiting the model only to description of the scanner horizontal behavior. The following Equation (4.1) can be then proposed.

$$\begin{bmatrix} x \\ y \end{bmatrix} = \begin{bmatrix} c_{xx'} & c_{xy'} \\ 0 & c_{yy'} \end{bmatrix} \cdot \begin{bmatrix} x' \\ y' \end{bmatrix} \tag{4.1}$$

This model, commonly applied for AFM calibration [52] describes the linear transformation of a distorted scanned image into the scaled, metric one. This is also the model, implemented in SPIP™ for lateral calibration [35].

As already stated $c_{xx'}$ and $c_{yy'}$ represent the scaling factor while $c_{xy'}$ the coefficient for correction of crosstalk error in the horizontal plane.

The proposed method allows for quantification of these calibration coefficients: higher order terms can also be in principle evaluated, but a software tool for completing analysis is still not available.

The calibration here described is based on use of fiber section as reference for evaluation of distortions introduced by AFM scanner. In fact when the arc of cylinder is measured, deviations occur in the scanned topography. The function transferring the measured topography to the actual one includes all the distortions symbolized by the vectors in Figure 4.4.
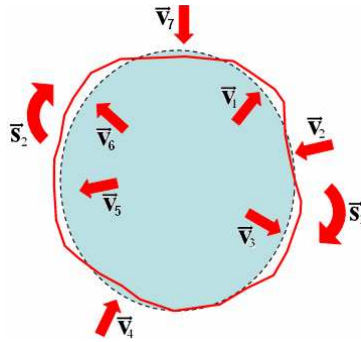

Figure 4.4: Actual and scanned sections: vectors are qualitatively indicative of occurred deformations.

In particular:

- $\vec{v}_1, \vec{v}_2, \vec{v}_3, \vec{v}_4, \vec{v}_5, \vec{v}_6, \vec{v}_7$ are representing distortions related to lateral calibration and non-linearities: these were referred to as $c_{xx'}$ and $c_{yy'}$ in Equation (4.1) and $c_{xx'^2}$ and $c_{yy'^2}$ in Equation (3.6);

- $\vec{s}_1$ and $\vec{s}_2$ are representative of the orthogonality error: referred to as $c_{xy'}$ in Equation (4.1) and $c_{xx'y'}$, $c_{xy'^2}$, $c_{yx'y'}$ and $c_{yx'^2}$ in Equation (3.6).

Distortions are also present due to drift. These should have to be eliminated or compensated or anyhow taken in account, since they can be interpreted as a horizontal orthogonality error.

The definition of the function transferring the measured topography to the actual one, allows for extrapolation of calibration coefficients $c_{xx'}$, $c_{yy'}$ and $c_{xy'}$. Additionally evaluation of fiber height can also be in principle used for quantification of calibration factor $c_{zz'}$.

4.3.2 Measurements and results

Measurements were carried out on the developed calibration standard, in order to test its applicability (Figure 4.5a). Different scans were performed using an Atomic Force Microscope

(AFM) at different sample orientations: 30° angle shifts around the fiber axis (12 measurements in total) were therefore taken into account between subsequent measurements. In parallel, measurements with the same scan parameters were carried out on a grating consisting of a two dimensional lattice of inverted cones with 2.12 µm pitch etched into a silicon chip [61].
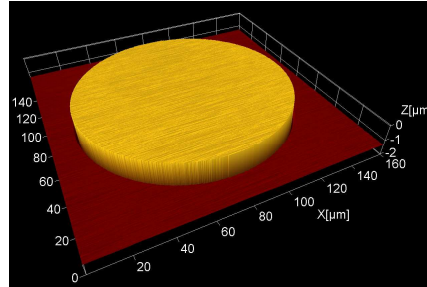

Figure 4.5: a) AFM measurement of the fiber section.

Automatic routines were developed and implemented into commercial software [35] for fast processing of the surface topographies. The software tool can perform calibration, based on the following three steps:

- edge detection, using a Sobel filtering mask. Other functions performing two dimensional spatial gradient convolution (such as Laplacian or Kirsch Compass) were tested, with no relevant improvements (Figure 4.6b) (Appendix B);

- segmentation, to complete circle edge isolation (Figure 4.6c);

- comparison of the extrapolated circle with the reference one (Figure 4.6c). Crosstalk and lateral scaling factors are eventually computed as members of the function transferring from the measured to the reference circumference.
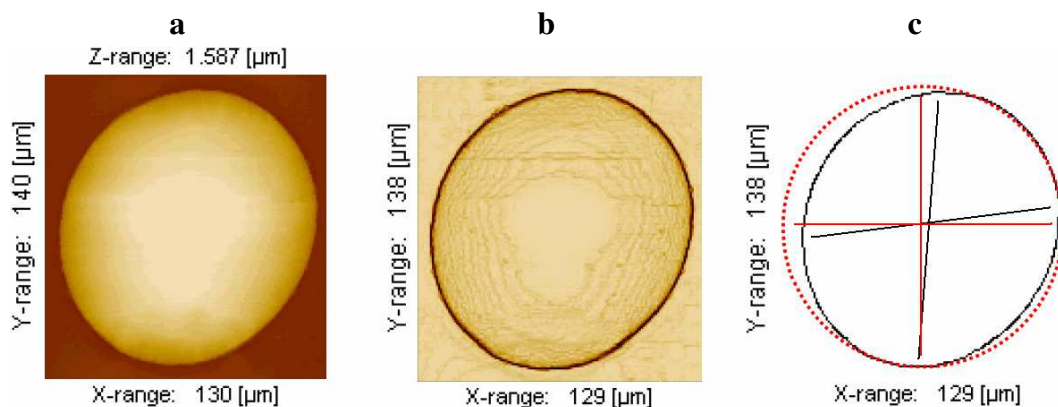

Figure 4.6: a) The scan over the optical fiber section; b) topography after Sobel filtering; c) final segmentation result (black line) compared with reference circumference (red dashed one).

Calibration factors were compared with those achieved using a 2D silicon grating (Table 4.4). Preliminary tests confirm applicability of the standard: in particular, full compatibility is shown

on the scaling factors. With regard to the crosstalk coefficient, normally affected by high relative uncertainty, further investigations are needed.

Table 4.4: Evaluated calibration factors and relative standard deviations.

	$c_{xx'}$	σ	$c_{yy'}$	σ	$c_{xy'}$	σ
Fiber	1.0023	$2 \cdot 10^{-4}$	0.9988	$2 \cdot 10^{-4}$	$6.3 \cdot 10^{-4}$	$1.5 \cdot 10^{-4}$
2D grating	1.0025	$2 \cdot 10^{-4}$	0.9991	$2 \cdot 10^{-4}$	$3.1\ 10^{-4}$	$1.2 \cdot 10^{-4}$

The sample is believed to be efficient for calibration of AFMs, however it can be applied in principle to the calibration of other instruments for surface topography characterization, such as Scanning Probe and Scanning Electron Microscopes, optical profilers, etc. High aspect ratios structures can also suitable for nano-CMM calibration, as already described in Section 4.2.1 (Figure 4.3).

As a demonstration of application, investigations were also performed on a Scanning Electron Microscope (SEM), after a gold sputtering (Figure 4.2b). Post processing was carried out, based on grey scaling: if images with sufficient contrast are taken, no impediment is seen in the application.

4.4 Vertical calibration

The present chapter gives a particular focus to a technique for exploiting fine vertical calibration. Common practice usually makes use of step heights: different samples covering different heights are usually applied to verify instrument performance. Other techniques that use vertical shift of the step standard, tilting devices and fine stage control, have been proposed in the past [68] [52] [81]. However, these methods present limitations or impediments to an application by both scientific and industrial SPM users. In fact, a proper characterization of the non-linear behavior of the whole instrument vertical range would require great efforts to perform a big amount of measurements. Other approaches, such as the use of physical wedges, precision positioning stages and laser interferometers, are limited by difficulties related to the production and costs of the devices [67] [82] [83].

In the following section we will discuss the possibility of using high precision cylindrical samples for calibrating AFM scanners on the full vertical range in terms of first, second and third order

vertical calibration coefficients (respectively $c_{zz'}$, $c_{zz'^2}$ and $c_{zz'^3}$). The standards were developed using optical fibers, which ensure the lowest non-circularity and roughness and the highest repeatability.

4.4.1 Application of the new standard for vertical calibration

The design of the proposed artefact is shown in Figure 4.2c and Figure 4.7: it simply consists of different micro-cylinders fixed on a flat surface, with diameters ranging from 80 µm to 125 µm. As stated above, fiber optics were used due to their exceptional surface quality. Glue not aggressive to glass surfaces, was applied to fix the fibers to a silicon substrate, which was used as a flat reference surface. Specifications of some suitable single mode fibers available on the market are reported (Table 4.3).

Parameters typical of vertical calibration can be evaluated by performing one or more measurements over the cylindrical surfaces and comparing measured curvatures with actual ones. Thanks to their specific shape, the newly introduced cylindrical standards can be used to calibrate an AFM scanner in the full vertical range, overcoming limitations often connected with using the steps of a fixed height.
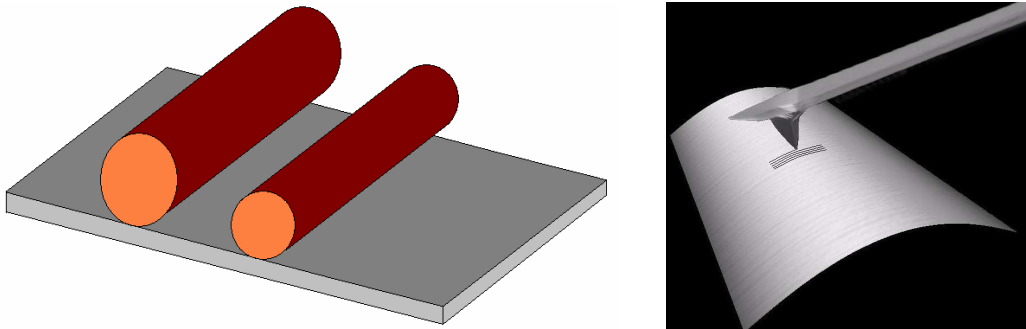
Figure 4.7: A drawing of the proposed standard and a representation of an AFM probe scanning a cylindrical surface.

4.4.2 Calibration principle

An AFM system, in good environmental-electro-mechanical equilibrium can be described as having no significant hysteresis or time-dependent creep: this is particularly true for closed loop instruments. This assumption implies that for each pair of measured coordinates (x', z') there is one single position of the tip. As a consequence the physical position of the tip z can be expressed as a function of the measured coordinates z' and x': $z(z', x')$.

A complete model for the description of an AFM measuring system can be achieved using a Taylor expansion, which describes the physical z-coordinate of a surface as a function of the uncorrected vertical and horizontal positions (respectively x' and z') measured by the scanning

instrument [52] and [53]. According to this model, the real physical position z approximated by the Taylor series to the third order in z' and x', is:

$$z(z',x') = c_{z0} + c_{zz'}z' + c_{zx'}x' + c_{zx'z'}x'z' + c_{zz'^2}z'^2 + c_{zx'^2}x'^2 + c_{zx'^2z'}x'^2z' + c_{zx'z'^2}x'z'^2 + c_{zx'^3}x'^3 + c_{zz'^3}z'^3 + \sigma(z'^3, x'^3) \qquad (4.2)$$

The proposed model doesn't include the y' axis in the computation: this mathematical simplification is sustained by the fact that AFMs do not deliver real topographies but only a collection of profiles of uncertain relative positions.

Equation coefficients are directly related to the instrument's performances:

- c_{z0} is a negligible offset;

- $c_{zz'}$ is the linear scaling factor;

- $c_{zx'}$ can be related to the sample installation slope;

- $c_{zx'z'}$, $c_{zx'^2z'}$, and $c_{zx'z'^2}$ are the cross correlation terms between x' and z', and quantify deviations from linearity on the vertical axis due to the position of x';

- $c_{zz'^2}$ measures the first order vertical non linearity;

- $c_{zx'^2}$ and $c_{zx'^3}$ are a measure for the image bow;

- $c_{zz'^3}$ measures the second order vertical non linearity.

- $\sigma(z'^3, x'^3)$ is the residual Peano error due to the Taylor series approximation.

Contributions related to the performance of the instrument specifically on the vertical axis (respectively $c_{zz'}, c_{zz'^2}$ and $c_{zz'^3}$) will be hereafter referred to with the term C_{zz*}.

In Figure 4.8 an ideal hemisphere and result of a typical AFM scan are represented.
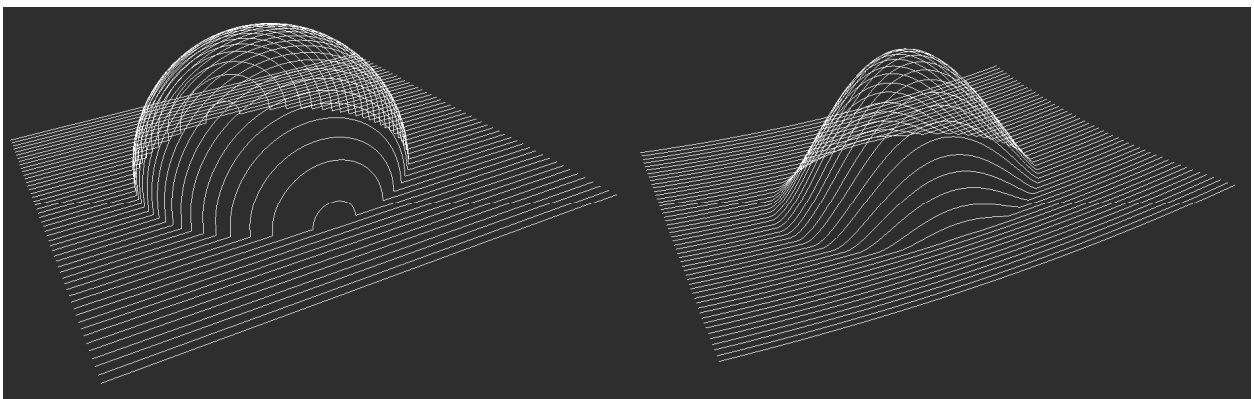
Figure 4.8: Ideal hemispheric shape and result of a typical AFM scan.

In principle a hemispheric shape could be applied for a complete calibration task: this is already done in the roughness profilometry field, and also in the coordinate metrology one. Unfortunately, it is very hard to manufacture hemispheric shapes fitting the needs of atomic force microscopy in terms of dimensions and accuracy. For this reason we have shifted our interest to

the cylindrical shape: this introduces some difficulties but, on the other hand, it is possible to use unexpensive objects as the fiber optics.

At this point it is important to understand how a cylindrical shape can help calibrate AFM scanners. When the arc of cylinder is measured, deviations occur in the scanned topography. The function transferring the scanned profile to the actual one includes all the distortions symbolized by the vectors in Figure 4.9.
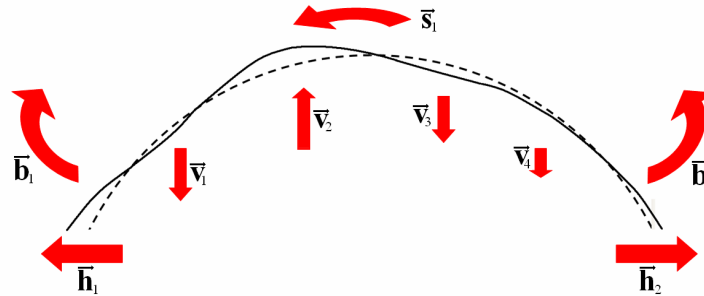

Figure 4.9: Actual and scanned cylinder arc: vectors are qualitatively indicative of occurred distortions.

In particular:

- $\vec{v}_1, \vec{v}_2, \vec{v}_3, \vec{v}_4$ are representative of distortions related to vertical calibration and non linearity: these were referred to as $c_{zz'}, c_{zz'^2}$ and $c_{zz'^3}$ in equation (4.2);

- $\vec{b}_1, \vec{b}_2$ are representatives of the bow effect: this was referred to as $c_{zx'^2}$ in equation (4.2);

- $\vec{h}_1, \vec{h}_2$ are related to horizontal calibration and non linearity, referred to as $c_{xx'}$ in Table 4.1 and in Equation 3.1;

- $\vec{s}_1$ is representative of the orthogonality error: referred to as $c_{xz'}$ in Table 4.1 and in Equation 3.4.

The two coefficients present in equation (4.2) are missing: c_{z0} and $c_{zx'}$. As already highlighted, the first one concerns the vertical offsets between the actual and scanned profiles, which are irrelevant for this analysis. The second one is related to the installation slope: thanks to the cylindrical shape, unaffected by rotational shifts, this deviation contribution is missing.

The cylindrical shape is proposed for the accurate calibration of an instrument's vertical axis in the full working range: for this purpose, deviations related to the horizontal axis have to be compensated for.

The procedure to eliminate the bow effect is commonly applied, especially when tube piezo scanners are used. A reference flat surface is scanned with a proper horizontal range: the result of the measurement, consisting of the bow curvature, is subsequently subtracted from measured topographies.

Finally, compensation of the residual horizontal distortions, mainly due to x-axis scaling effects, is carried out by correcting measurements through calibration factors. An alternative could be then the measurement and comparison of at least two or more cylinders with different diameters.

4.4.3 Coefficient extraction

An analysis software tool was specifically developed and implemented for comparing scanned cylindrical topographies with actual ones, and eventually extracting calibration coefficients [84] [35]. The sequence of operations performed by the single routines is shown in Figure 4.10.
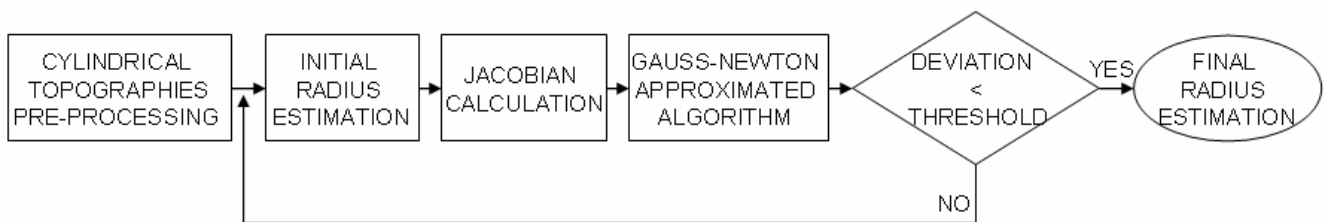

Figure 4.10: Cylindrical fitting procedure.

As a first step (referred to in the diagram as the pre-processing phase), the symmetry of the profile is checked using centre of mass estimations. Possible asymmetries are directly related to x-z orthogonality errors. Before proceeding with further analyses, these are corrected by applying opposite angular deformations.

Subsequently, the best fitting arcs of circumference are evaluated for each profile through approximated Gauss-Newton's algorithm. This is one of the most robust and well-known numerical methods for solving a root finding problem f(x)=0, where f(x) is a non-linear function. This technique is commonly used in applications of linear least squares model of circles, spheres, cylinders, and cones. Gauss-Newton's algorithm is recursive: in fact it is repeated until it converges to a point, within a given threshold. For the present study, the threshold was set to 1 nm.

Local and global curvatures are then evaluated and compared with reference values. The fitting operation and comparison task are automatically repeated for different scan lengths L.
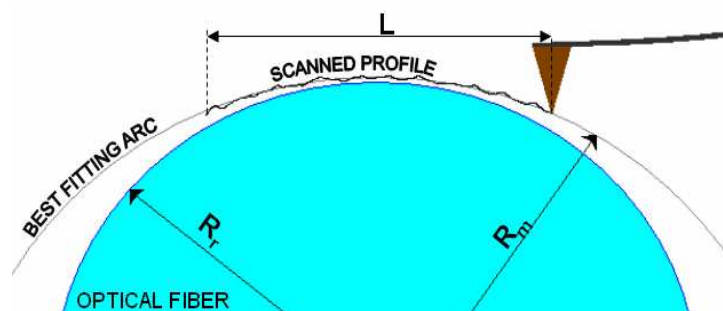

Figure 4.11: Parameters used for the evaluation of the calibration factor.

With reference to Figure 4.11, Equation (4.3) shows how a calibration factor can be achieved for a given arc of circumference:

$$C_{zz*} = \frac{R_r - \sqrt{R_r^2 - 0.25 \cdot L^2}}{R_m - \sqrt{R_m^2 - 0.25 \cdot L^2}} \qquad (4.3)$$

where subscript r refers to reference values and subscript m to the measured ones. R indicates the radius, L the scanned range, both evaluated after correction through horizontal calibration factors. Reporting the C_{zz*} trend as a function of z' and fitting the points through a second or higher order function, it is possible to extract other coefficients relative to the vertical coordinate axis calibration: respectively $c_{zz'}$, $c_{zz'^2}$ and $c_{zz'^3}$.

The analyses described above are carried out on surface topographies centered with respect to the horizontal measuring range. By repositioning the fiber and repeating measurements at different positions in the x range, it is possible to evaluate correlation between the x' and z' axes: this estimation was not considered in this work.

4.3.4 Measurements and results

The proposed method was applied for the fine calibration of the vertical coordinate axis of a commercial open loop AFM. The tube scanner was produced by DME with a measuring volume of 200×200×15 µm. Experimental results were based on the use of two different single mode fibers selected and produced by OFS Fitel Denmark ApS. The fiber specifications are reported in the table below (Table 4.5).

Table 4.5: Manufacturer specifications of the optical fibers used in the experiments.

	Cladding diameter [µm]	Cladding ovality [%]	Surface Roughness RMS [nm]
Fiber 1	124.75	0.07	3.5
Fiber 2	79.73	0.24	3.7

Measurements were taken in different portions of fiber taken from a 3 m long thread. Ten contact mode measurements were taken for each fiber: respectively 60×60 µm² and 50×50 µm² for Fiber 1 and Fiber 2. Scan ranges were chosen in order to not exceed the dynamic z-range (~15 µm) and to avoid tip damages or tip flights. The scan speed was set at 5 µm/s and the scan force 10 nN. The fiber was carefully positioned orthogonally to the x-scan direction. Two additional measurements, called Flat References, were carried out over the silicon flat surface; these were performed by applying the same scan setting used respectively for Fiber 1 and Fiber 2.

Surface topographies were processed as described in Paragraph 4.3. Surface topographies were corrected of the bow effect by subtracting the Flat Reference topography; they were then corrected using x-y coordinate axes calibration factors. Cylindrical topographies were finally processed using the automatic routine described above.

4.3.5 Uncertainty estimation

Uncertainty $u(C_{zz*})$ related with the evaluation of C_{zz*} was estimated, according to the Guide to the Expression of Uncertainty in Measurement (GUM) [85], based on its mathematical model. Equation (2) was referred to as model function for variables R_r, R_m and L.

The degree of correlation between the input quantities R_m and L was evaluated by sets of tests on different virtual images. L was varied within a ±2% range, simulating a possible lateral calibration error, and effect on the measured radius R_m was studied through covariance analysis. An average correlation coefficient r(L, R_m)=0.13 was quantified. A simplification was then introduced, considering the other quantities independent.

The most critical estimation is the effect due to the radius R_m. The Gauss-Newton's algorithm implemented provides an arc radius with a precise approximation, defined by the threshold (1 nm). Nevertheless deviations are possible, caused by noise, distortions, tip to sample interaction or perturbations effects, affecting the scanned profiles. The combined standard uncertainty associated with the evaluation of R_m was estimated by carrying out a set of simulations on virtual images. Virtual topographies used within the simulations took into account distortions caused by noise and other sources (see Section 3.3).

Uncertainty sources connected with the fiber geometry were considered as part of the uncertainty related with the actual radius R_r. The quantification gave a combined standard uncertainty of 0.15 µm and 0.2 µm for Fiber 1 and Fiber 2 respectively.

The uncertainty sources in the measurement of the scanned range L are mainly due to the lateral calibration and lateral resolution. The lateral calibration error is caused by the calibration operation, performed through calibrated gratings, and can be roughly approximated in excess to $0.02 \times L$. The contribution of the resolution is derived from the sampling settings: having set 2048 pixels per line, the lateral resolution was 29 nm and 24 nm for Fiber 1 and Fiber 2 respectively.

Table 4.6: Uncertainty in the measurement of local calibration factor czz*; Rm standard uncertainty was experimentally derived; *h* is the vertical range in nm.

Source of unc.	Value of standard uncertainty		Sensitivity coefficients
	Fiber 1	Fiber 2	
L	$0.02\,L$	$0.02\,L$	$$\dfrac{L\left(\dfrac{R_m - \sqrt{R_m^2 - L^2/4}}{\sqrt{R_r^2 - L^2/4}} - \dfrac{R_r - \sqrt{R_r^2 - L^2/4}}{\sqrt{R_m^2 - L^2/4}}\right)}{4\left(R_m - \sqrt{R_m^2 - L^2/4}\right)^2}$$
R_m	$(0.2+0.02/h)$	$(0.13+0.013/h)$	$$\dfrac{\left(R_r - \sqrt{R_r^2 - L^2/4}\right)\left(\dfrac{R_m - \sqrt{R_m^2 - L^2/4}}{\sqrt{R_m^2 - L^2/4}}\right)}{\left(R_m - \sqrt{R_m^2 - L^2/4}\right)^2}$$
R_r	$0.15\ \mu m$	$0.20\ \mu m$	$$\dfrac{\sqrt{R_r^2 - L^2/4} - R_r}{\sqrt{R_r^2 - L^2/4}\left(R_m - \sqrt{R_m^2 - L^2/4}\right)}$$
L-R_m cross-correlated effect			$$\dfrac{L\left(R_r - \sqrt{R_r^2 - L^2/4}\right)}{4\sqrt{R_m^2 - L^2/4}\left(R_m - \sqrt{R_m^2 - L^2/4}\right)}\left(\dfrac{1 - \sqrt{R_m^2 - L^2/4}}{R_m^2 - L^2/4} + \dfrac{1}{\sqrt{R_r^2 - L^2/4}}\right)$$

Evaluated scaling factors C_{zz*}, averaged on the twenty measurements, with the expanded uncertainties are reported as a function of z', both for the Ø=124.75 µm and for the Ø=79.73 µm fibers. z' is given as the vertical range of the arc used for the computation (Figure 4.12). The graph shows C_{zz*} is not a constant but a function of z': this behavior can be modeled and described through a polynomial function, as reported below.
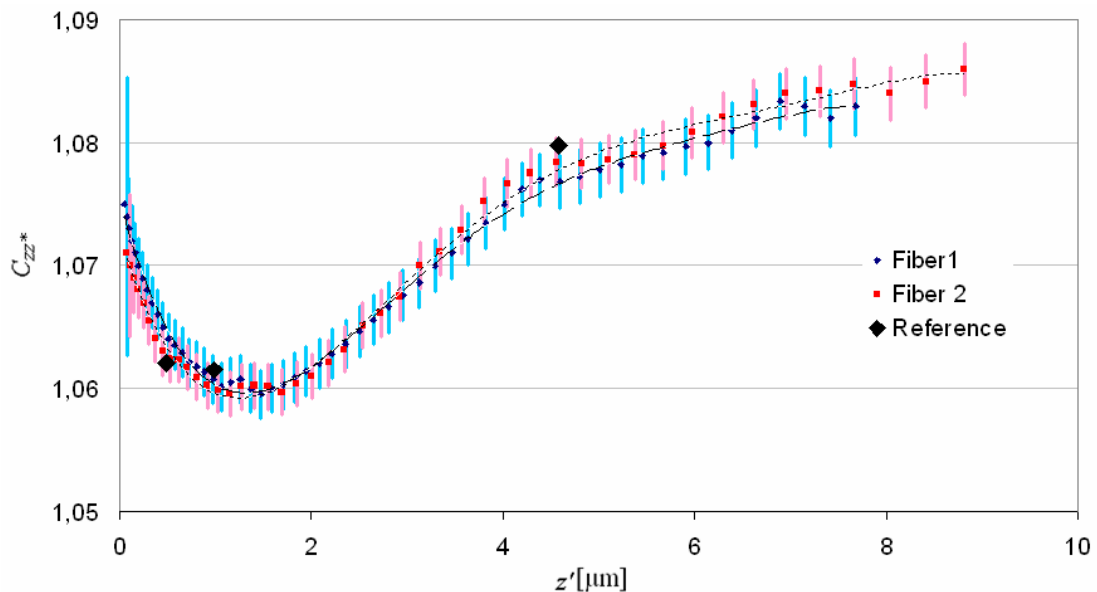

Figure 4.12: Variation of Czz* as a function of z'.

4.3.6 Extrapolation of the calibration coefficients

Using the same principle described in [52], data sets collected from the two fibers were fitted through a fourth order polynomial function (4.4):

$$C_{zz*}(z') = a + b \cdot z' + c \cdot z'^2 + d \cdot z'^3 + e \cdot z'^4 \tag{4.4}$$

The following results were achieved:

- Fiber 1 $C_{zz*} = 1.0771 - 0.0335 \cdot z' + 0.0209 \cdot z'^2 - 0.0050 \cdot z'^3 + 0.0005 \cdot z'^4$

with a correlation coefficient R=0.995 between experimental data and the polynomial function;

- Fiber 2 $C_{zz*} = 1.0737 - 0.0284 \cdot z' + 0.0175 \cdot z'^2 - 0.0039 \cdot z'^3 + 0.0004 \cdot z'^4$

with a correlation coefficient R=0.996 between experimental data and the polynomial function.

The correlation coefficients worsen down to R=0.94 for both fibers whenever the polynomial function is truncated to the third order term. This is mainly due to the fact that a third order function is not sufficient to properly describe an instrument's non-linearity. In particular, the right part of the graph reported in Figure 4.12, corresponding to extreme conditions (the scanner working in the full vertical range), is better described by a fourth or higher order function.

In finite terms C_{zz*} represents the ratio between the actual and the measured heights. Passing from the discrete to the continuous, point by point the polynomial fitting curves shown in Figure 4.12 represent the local instantaneous rate when the step tends to zero (4.5):

$$C_{zz*} = \frac{\Delta h_r}{\Delta h_m} = \frac{\Delta z}{\Delta z'} \xrightarrow{\text{if } \Delta z' \to 0} C_{zz*} = \frac{\partial z}{\partial z'} \longrightarrow \partial z = C_{zz*} \partial z'. \tag{4.5}$$

Integrating the last equation in (4.5) and introducing function (4.4), we can express the contribution of z' to z as:

$$z(z') = \int C_{zz*} dz' = \int (a + b \cdot z' + c \cdot z'^2 + d \cdot z'^3 + e \cdot z'^4) dz' = a \cdot z' + \frac{b \cdot z'^2}{2} + \frac{c \cdot z'^3}{3} + \frac{d \cdot z'^4}{4} + \frac{e \cdot z'^5}{5} + k \tag{4.6}$$

This contribution (4.6) represents part of the expression reported in (4.2): corresponding terms can be easily extrapolated, as follows (4.7):

$$z(z') = a \cdot z' + \frac{b \cdot z'^2}{2} + \frac{c \cdot z'^3}{3} + \frac{d \cdot z'^4}{4} + \frac{e \cdot z'^5}{5} + k = c_{z0} + c_{zz'} z' + c_{zz'^2} z'^2 + c_{zz'^3} z'^3 + P(x', z') \tag{4.7}$$

Where the polynomial $P(x', z')$ includes higher order terms (such as $c_{zz'^4} z'^4$ and $c_{zz'^5} z'^5$) and terms not relevant for the equation (such as $c_{zx'^2} x'^2$).

From expression (4.7), we can evaluate the calibration coefficients up to the third order:

$$c_{zz'} = a; \tag{4.8}$$

$$c_{zz'^2} = \frac{1}{2} b; \tag{4.9}$$

$$c_{zz'3} = \frac{1}{3}c. \tag{4.10}$$

Coefficients d and e can be used in order to evaluate higher order calibration coefficients (i.e.: $c_{zz'4}$ and $c_{zz'5}$); otherwise they can be computed as part of the residual error $\sigma((z'(x')^3),(x'^2))$; k is a negligible constant, contributing to the other constant c_{z0} as seen before.

From analyses on Fibers 1 and 2, coefficients $c_{zz'}$, $c_{zz'2}$ and $c_{zz'3}$ were computed, and the results are reported in Table 4.7.

Table 4.7: Vertical calibration coefficients.

	$c_{zz'}$	$c_{zz'2}$ [μm^{-1}]	$c_{zz'3}$ [μm^{-2}]
Fiber 1	1.0771	-0.0168	0.0070
Fiber 2	1.0737	-0.0142	0.0058

4.3.7 Results

The vertical calibration curves agreed well within their expanded uncertainties: slight differences can be seen from the results relative to the two different fibers, more evidently in the extreme areas of the graph. Good agreement was also verified after comparison with values on reference step height specimens (Figure 4.12). Moreover, these differences are associated with higher uncertainties. The origin of these deviations can be correlated mainly to the different diameters of the two fibers. Whenever the radius of the curvature is evaluated by the automatic routine, more precise results can be expected for arc angles comprised between ±5° and ±50°, as shown in Figure 4.13.
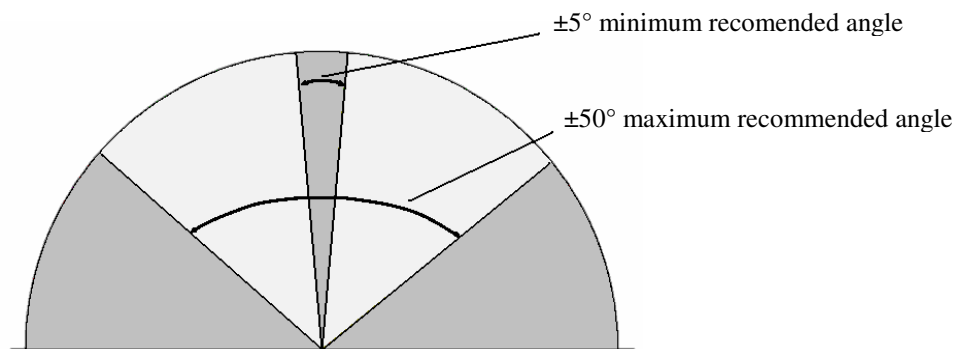
Figure 4.13: Part of the fiber best suited for the calibration.

The lower limit can be explained by looking at the arc fitting operation: inaccurate results could be achieved when the arc is too small and local perturbations can deviate from the measured curvature. On the other hand, distortions can be expected when the local cylinder topography slope is bigger than ~50°, due to the tip flank of the surface interaction. This can be seen in

Figure 4.12, where higher uncertainties are found when z' is close to zero or is bigger than 7-8 µm. In general, the smaller fibers seem to be more suitable when calibrating low height ranges; conversely bigger ones are recommendable when higher vertical ranges have to be calibrated.

4.5 Orthogonality

4.5.1 Basic principle

Deviations from orthogonality between the z axis and the scanning directions x, y have to be checked and corrected, in particular whenever slopes have to be extracted and evaluated from AFM measurements.

In Figure 4.14 profile of a non symmetrical triangular profile is shown. With reference to Figure 4.14a: α and β are the actual slopes, calculated relatively to the horizontal axis. The measured slopes α' and β', because the orthogonality error γ, do not equal the sidewall angles of the cusp (Figure 4.14b). Upon rotating the specimen by an amount of 180 degrees around the vertical, and tracing, the profile of Figure 4.14c can be obtained, that is reversed. The new measurements give a different result, with the new sidewall angles α" and β".

Determination of the squareness error γ can be accomplished with the reversal strategy depicted, by comparing measured angles α', β' with α" and β" [48].

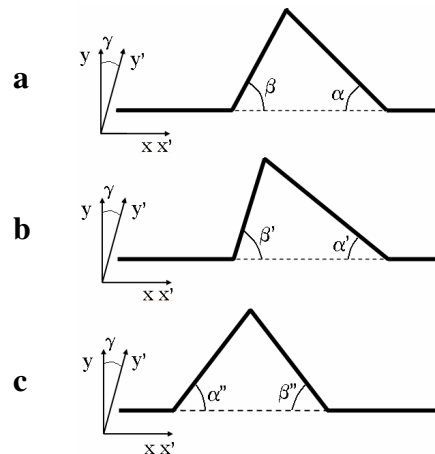

Figure 4.14: Non-symmetrical triangular profile. a) Actual slopes. b) Effective slopes differ from the nominal ones due to the squareness error γ. c) Reversed sample positioning.

The following sets of equations can be derived from the Figure 4.14b:

$$\begin{cases} \alpha' = \alpha - \gamma \\ \beta' = \beta + \gamma \end{cases}$$

(4.11)

And from Figure 4.14c:

$$\begin{cases} \alpha'' = \alpha + \gamma \\ \beta'' = \beta - \gamma \end{cases}$$
(4.12)

The unknowns are α, β and γ, and four linear relations were found. The problem can therefore be simply solved, for example through Equation (4.13):

$$\begin{cases} \alpha = \dfrac{\alpha' + \alpha''}{2} \\ \beta = \dfrac{\beta' + \beta''}{2} \\ \gamma = \dfrac{(\alpha'' - \alpha' + \beta'' - \beta')}{4} \end{cases}$$
(4.13)

The procedure described here can be applied to the x,z and the y,z axes separately to determine crosstalk errors in the two vertical planes.

4.5.2 Vertical axis

An automatic routine for evaluation of crosstalk errors on vertical planes and subsequent compensation was developed and implemented into commercial software [35].

The orthogonality estimation tool is based on the principle described above. Any couple of measurements performed on a topography presenting a triangular pattern is suitable for analysis [86]. Analyzing equation (4.13), it results evident that for a correct estimation of γ, knowing the sidewall angles is not strictly necessary. Indeed application of the reversal method bring to a simplification of systems of equations (4.11) and (4.12), bringing to a solution that is a function only of the measured sidewall angle values α', β', α'' and β''. This is helpful, since it means that estimation of the orthogonality of axes can be performed even if the instrument is not calibrated in the vertical direction. Conversely, using a single scan approach would introduce more difficulties:

- knowledge of the actual sidewall angles;
- calibration of the instrument vertical axis.

The sequence of operations performed by the orthogonality estimation routine is shown in the following figure (Figure 4.15).

Figure 4.15: Orthogonality estimation procedure.

First of all scanned topographies undergo to installation slope correction. This is achieved by real a real rotation operation [50]. In fact, as already discussed (Section 3.3.12) simple projection is

not a rigid transformation, introducing distortions in the scanned topographies. As shown in Figure 3.16, a consequence would be deformation of triangles (an equilateral triangle would turn to a scalene one), introducing an error in crosstalk evaluation.

The second step is detection of the core part. An example is given in Figure 4.16 this refers to a measurement performed on a calibration samples, generated by KOH etching of silicon [61]. This etching process is highly anisotropic, generating sharp isosceles triangular cusps, with slopes of 54.7 degrees.

Segmentation is done by evaluating the mean distance Δz between the top of peaks and the bottom of valleys, and isolating the regions whose vertical height is comprised within a certain percentage Δp (defined by the operator) of the total height Δz (see Figure 4.16b)

Sidewall angles are evaluated by computing best fitting lines. Fitting is carried out on each profile and on each triangle, using data sets within core region (Figure 4.16c). Mean α' and β' values for the first scanned image and α" and β" values for the reverse scanned image are eventually processed for quantification of deviation from orthogonality γ.
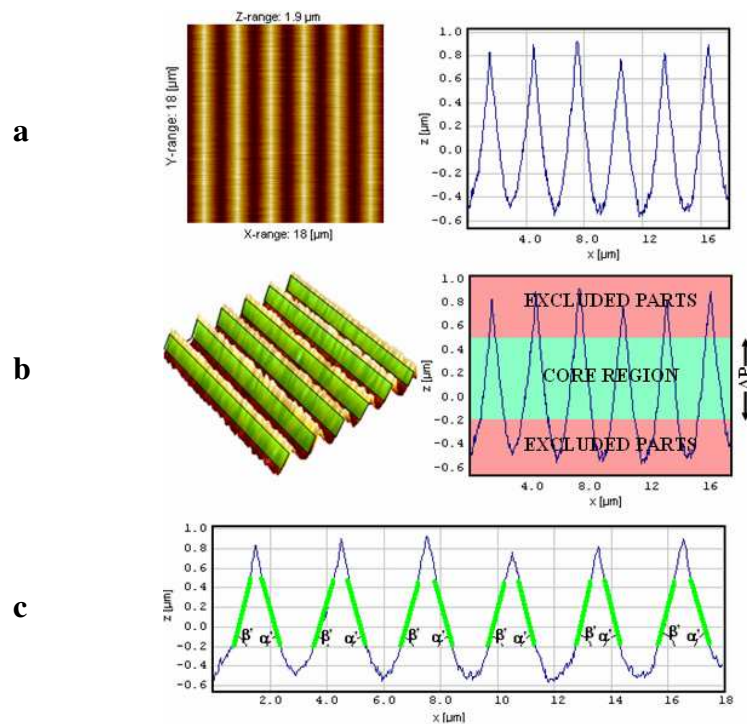

Figure 4.16: Example of orthogonality estimation in three steps: a) a measurement on a triangular profile is analyzed; b) the core region is used to evaluate flanks slope; c) flanks angles can then be compared with reference values to quantify deviation from orthogonality.

Besides automatic procedure for extraction of sidewall slope angle features, also an off-line correction of deviations from orthogonality in the x,z and y,z planes was implemented in the SPIP™ environment. This software tool implements the simplified mathematical model described in the previous chapter (Equation 3.4). A resampling strategy has also been introduced,

together with the orthogonality correction tool, in order to allow preservation of the constant pixel dimension, needed for the matricial representation described in Chapter 3.1, and used by most of commercial software for analysis of SPMs measurements.

4.6   Conclusions

The present chapter addresses AFMs calibration issue.

A new concept of calibration standards is presented, based on an optical fibers technology. It is shown how fibers, used as micro-cylinders, can be applied for performance verification of a number of instruments for topographical characterization in the microscale.

In particular the possibility of accurately calibrating horizontal and vertical AFM axes is described: results are seen to fairly agree with values coming from traditional techniques.

The merit of the new procedure for vertical calibration is the possibility of calibrating the instrument with continuity over the full vertical range. The same task in common practice would need a number of measurements on different step heights of a fixed height.

The chapter eventually discusses orthogonality, presenting a software tool developed for estimation and correction of crosstalk errors.

4.6.1 Contributions

A grateful acknowledgement is given to OFS Fitel Denmark ApS. and Pietro Sanguini for studying and providing several optical fibers best suited for vertical calibration purposes.

Stefano Cossi, Nicola Marcolongo, Stefano Zanoni and Francesca Borsetto, are also acknowledged for the important contribute given by their master thesis works to the development of the solutions proposed in the present chapter.

Chapter 5

Artifact Correction

5.1 Introduction

Atomic force microscopes (AFMs) allow surface topography imaging with the highest resolution, as a result of precise actuation combined with the sharpness of tips. As already described in Chapter 3, surfaces are scanned in a raster fashion by a probe and topographies are sequentially built up. This sequential imaging process suffers from instrumental drift, predominantly in the slow scan direction. Data sets should therefore be regarded as collections of parallel profiles of uncertain relative vertical position, rather than truly three-dimensional images [51]. An important consequence is that surface topography is known accurately only in the fast scan direction x and no reliable analysis can be performed along the two perpendicular directions y and z.

Additionally due to physical effects and dynamic interactions, tip shape evolves with time: in particular continuous deterioration is introduced by wear phenomena; this means that tip sharpness is not constant. The consequence is that also convolution distortions affect measurements in a non-constant way: a correct compensation (deconvolution), would then require for a frequent monitoring of tip dimensions.

In this chapter drift and tip wear are considered and in particular:

- quantification and compensation of vertical and (with some limitation) horizontal drift;

- quantification and modeling of tip wear.

5.2 Vertical drift

It has already been described how surfaces are scanned in a raster fashion and how such sequential imaging process suffers by instrumental drift, predominantly in the slow scan direction. In addition, pick up of dust contamination may contribute in further alter profiles alignment. Off-line correction methods are implemented in commercial software packages, to

provide leveling of the single profiles. However, these are blind routines based on polynomial fitting and, ultimately, they flatten topography in the slow scan direction. As already discussed in Paragraph 3.3.12, a relevant consequence of such flattening is that surface topography is known accurately only in the fast scan direction and no reliable analysis can be performed perpendicularly to that. Other approaches have been investigated and proposed to get rid of this distortion, considering hardware [87] as well as software [88] [89] solutions.

In the presented chapter implementation and validation of a method for accurate imaging of three-dimensional surface topographies, developed for AFM metrology but in principle applicable to the whole family of scanning probe microscopes is presented [48] [90] [91]. The method provides correction of the vertical drift, and can be applied to any AFM scanner system, without need of modification of the instrument hardware.

5.2.1 Method for three dimensional AFM imaging

The method presented hereafter is based on own developed software [48] [90] coded in C++ within the programming interface of a commercially available software package [35].

A pair of AFM scans is processed and a single data set produced as an output, containing the corrected three-dimensional surface topography.

The measuring strategy is based on two images, used to complete the reconstruction (Figure 5.1):

- For the first image (Figure 5.1a), scan angle is set to 0 degrees, i.e. x- is the fast scan direction. From here on this will be referred to as the XFD (X-Fast scan Direction).

- For the second image (Figure 5.1b), scan angle is set to 90 degrees, so that y- is the fast scan direction, orthogonal to cantilever axis. This will in the following be referred to as YFD (Y-Fast scan Direction).
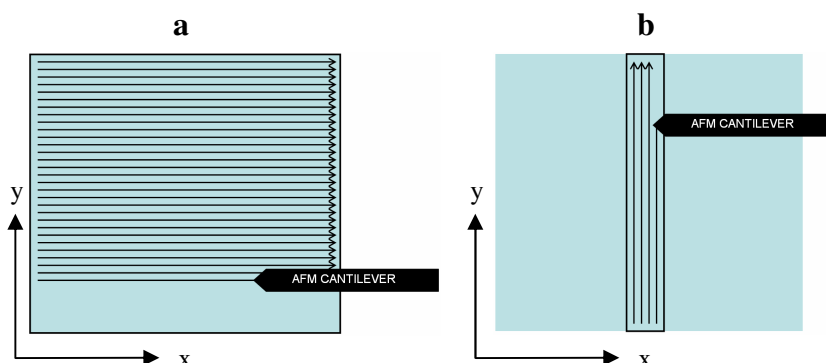

Figure 5.1: AFM imaging process. Arrows indicate single profiles taken in the fast scan direction. This is, respectively, x-direction (a) and y-direction (b). The black border in (a) indicates the XFD, while the one in (b) defines the YFD.

For the success of the reconstruction, the measuring strategy can also be modified: 0 and 90 degrees are just the most common scan directions, but the method works identically if other orthogonal scan directions are chosen, such as +45 and -45degrees or +60 and -30 degrees.

Other scanning solutions were considered and can be applied for the YFD scan, not modifying in substance the concept of the proposed method. Some examples are reported in Figure 5.2. The centered scan (Figure 5.1b) was anyhow preferred for a few reasons:

- it was found to be the fastest one;

- no offsets are needed, as in the case of solutions (a) and (b) in Figure 5.2;

- no multiple scan operation is required, as in the case of strategy (d) in Figure 5.2.
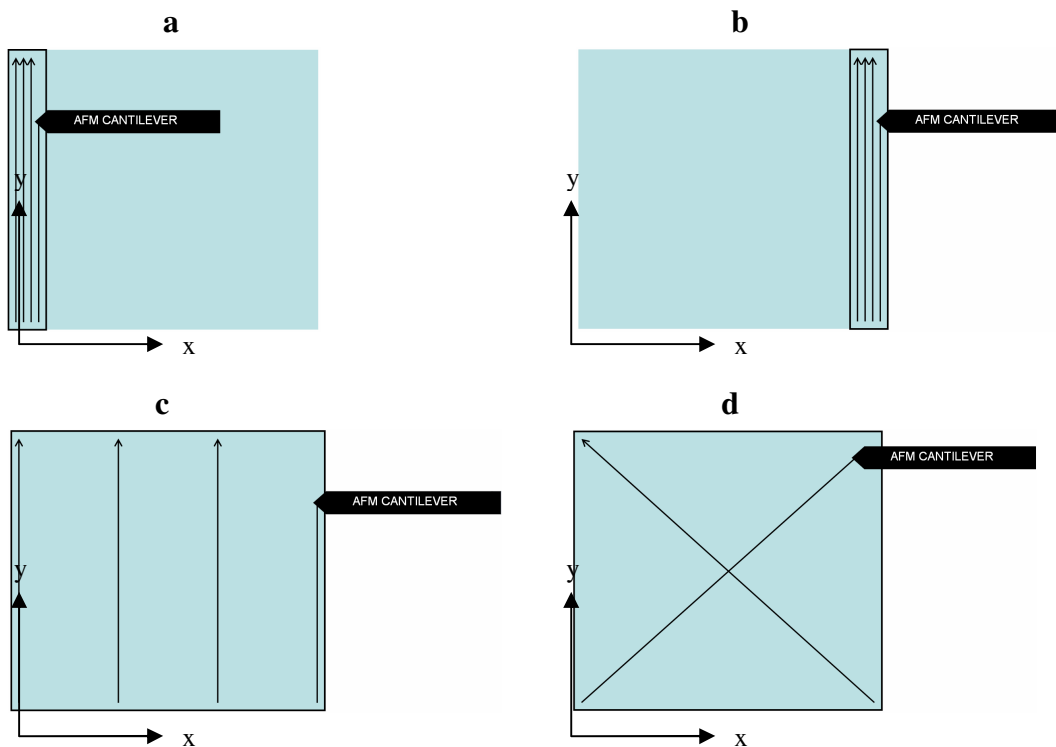

Figure 5.2: AFM imaging process. Alternative measuring strategies considered for the YFD measurement: (a) and (b) uncentered scans; (c) large low resolution scanning; (d) double crossed scanning.

5.2.2 Reconstruction

Thermal drift is a time-dependent source of error, therefore its effect within single profiles can be considered negligible. Conversely, in the slow scan direction, high uncertainties are introduced: information on surface topography is in fact mixed up with scanner system drift. Deviations from true sample topography are further amplified when dust contamination interferes with tip movements. This is picked up by the AFM tip, which is offset vertically and suddenly discharged afterwards.

The XFD scan corresponds to the measurement that is habitually performed on an AFM. Therefore no particular restrictions or recommendations are defined with regard to the instrumental settings, such as x- and y- range and sampling intervals.

As shown in Figure 5.1b, or Figure 5.2, the YFD image only partially covers the region of interest, which is the whole surface imaged in the XFD scan, with obvious advantage in terms of time consumption.

Scanner settings for the YFD image are constrained as illustrated in Table 5.1.

Table 5.1: Scan settings.

YFD x-range= 2-5 % · (XFD x-range)
YFD x-resolution= XFD x-resolution
YFD y-range= XFD y-range
YFD y-resolution= XFD y-resolution

Information from the two images is eventually combined in a single data set, containing the correct topography of the region of interest (Figure 5.3c).

The reconstruction is based on the following assumptions:

- Within the XFD image, single profiles reproduce surface topography with fidelity, because they are not distorted by drift. However, their relative position is not known (Figure 5.3a).

- The YFD image provides this information for vertical leveling, which is missing within the XFD data set (Figure 5.3b).
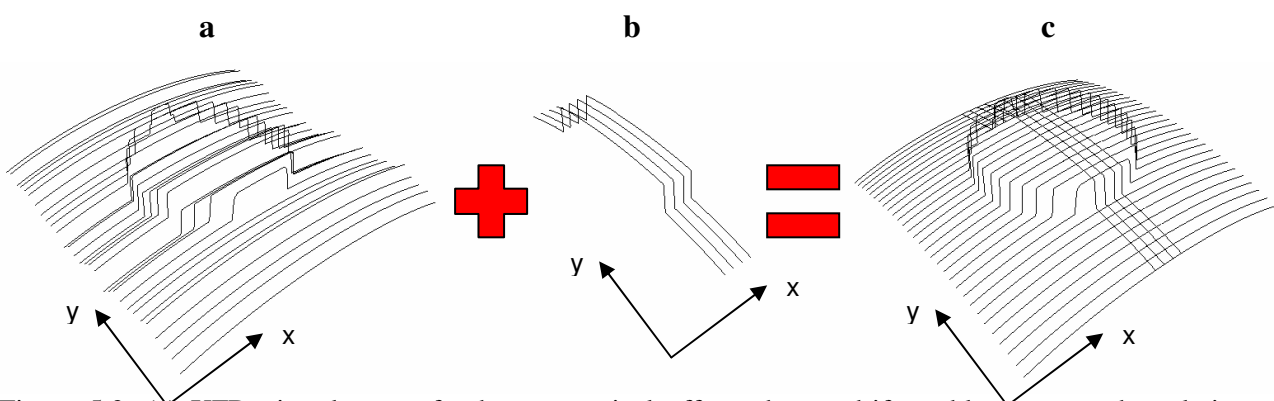

Figure 5.3: (a) XFD virtual scan of a bump: vertical offsets due to drift problems cause the relative vertical position of profiles to be uncertain; (b) the YFD scan brings the shape information on the y-direction; (c) by coupling the XFD and YFD scans, it is possible to reconstruct the bump topography.

Surface topography in the y- direction, i.e. relative positions of the XFD profiles, is calculated by using the YFD scan. As depicted in Figure 5.3, each single XFD profile is re-aligned, through application of equation (5.1):

$$\Delta z_i = \frac{\sum_{j=1}^{J}(z'_{i,j} - z''_{i,j})}{J} \qquad \forall i = 1,...,m \qquad\qquad\qquad (5.1)$$

AFM images can be represented as two-dimensional data arrays, being each value, stored at any pixel location, the local topography elevation value. Let the XFD image be a rectangular array of dimensions: m × n. Let $z'_{i,j}$ indicate the value stored in j-th column and i-th row in the YFD data set; $z''_{i,j}$ the corresponding pixel in the XFD image. Δz_i is eventually the vertical shift to be imposed to the whole i-th profile of the XFD data set.

The method just outlined is easily applicable to any commercially available AFM system, because the sensor can be actuated in any in-plane direction. Its implementation is effective because, no matter what it is, the fast scan direction is negligibly affected by thermal drift. The method causes only a slight increase in the scan time, which can be estimated in a percentage ranging from 1 % to 5 %.
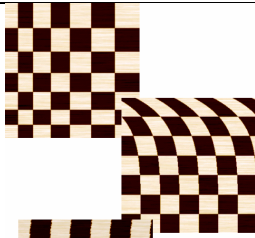
5.2.3 Limits

Main limitations to the developed method are related with horizontal distortions affecting the scanning operation. These result in a discrepancy between the intended and the actual scanned points, caused by uncontrolled relative movements between the tip and the sample. The effect of these deviations is an uncorrected variable offset between XFD pixels and corresponding YFD pixels. As a consequence, the reconstruction carried out by the proposed method can be negatively influenced.

Deviations incoming during scanning operations are mainly due to two components: one is resulting from the actuating system and the other is caused by deformation of the mechanical units. A list of the principal distortions of interest for the present application, which are affecting in particular open loop scanners, is reviewed in Table 5.2.

As already discussed in Chapter 2, piezoelectric actuators show hysteretic behavior, due to the dependence of the scanners on the applied voltage range. Also creep is due to the piezo-actuators: in fact it is an effect of time-dependence caused by the relaxation process in the response to a voltage of the piezoelectric material. Thermal drift influences measurement heavily also in closed loop scanners, in particular when high resolution imaging is achieved by taking many profiles.

In the Table 5.2, an AFM image of a chessboard-like grating undergoing hysteresis, creep and drift is reported (distortions have been magnified on purpose).

Table 5.2: Problems in lateral metrology with AFM (images present emphasized distortions).

Problem	Effects	Typical aspect
Hysteresis	Image content dependence on the scan direction (trace do not coincide with retrace)	
Creep	Scanner extension and therefore traced length variable with scan rate	
Drift	Misalignment of the profiles in the fast scan direction	

A proper instrument calibration can reduce deformations incoming during measurements. As extensively reported in Chapter 3, a mathematical model for lateral calibration, which consider also nonlinearities and systematic component of drift, can be written as follows (5.2):

$$
\begin{bmatrix} x \\ y \end{bmatrix} = \begin{bmatrix} c_{xx'} & c_{xy'} \\ 0 & c_{yy'} \end{bmatrix} \cdot \begin{bmatrix} x' \\ y' \end{bmatrix} + \begin{bmatrix} c_{xx'^2} & c_{xy'^2} & c_{xx'y'} \\ c_{yx'^2} & c_{yy'^2} & c_{yx'y'} \end{bmatrix} \cdot \begin{bmatrix} x'^2 \\ y'^2 \\ x'y' \end{bmatrix} + \begin{bmatrix} u_x \cdot t \\ u_y \cdot t \end{bmatrix}
$$
(5.2)

where the model has been limited to the second order approximation, in the horizontal x-y plane. The offset between XFD pixels and corresponding YFD pixels is evaluated by differentiating model (5.2) applied to the two measurements:

$$
\begin{bmatrix} \Delta x(x,y) \\ \Delta y(x,y) \end{bmatrix} = \begin{bmatrix} x \\ y \end{bmatrix}_{XFD} - \begin{bmatrix} x \\ y \end{bmatrix}_{YFD} =
$$

$$
= \left(\begin{bmatrix} c_{xx'} & c_{xy'} \\ 0 & c_{yy'} \end{bmatrix}_{XFD} - \begin{bmatrix} c_{xx'} & c_{xy'} \\ 0 & c_{yy'} \end{bmatrix}_{YFD} \right) \cdot \begin{bmatrix} x' \\ y' \end{bmatrix} + \left(\begin{bmatrix} c_{xx'^2} & c_{xy'^2} & c_{xx'y'} \\ c_{yx'^2} & c_{yy'^2} & c_{yx'y'} \end{bmatrix}_{XFD} - \begin{bmatrix} c_{xx'^2} & c_{xy'^2} & c_{xx'y'} \\ c_{yx'^2} & c_{yy'^2} & c_{yx'y'} \end{bmatrix}_{YFD} \right) \cdot \begin{bmatrix} x'^2 \\ y'^2 \\ x'y' \end{bmatrix} + \begin{bmatrix} d_x \cdot t \\ d_y \cdot t \end{bmatrix}_{XFD} - \begin{bmatrix} d_x \cdot t \\ d_y \cdot t \end{bmatrix}_{YFD}
$$
(5.3)

With good approximation, the calibration matrix $C_{xy}^{(1)}$ can be considered constant; similarly also the mean drift velocity components can be assumed to be constant when passing from the XFD to the YFD scan. With these premises, the (5.3) can be simplified as follows:

$$
\begin{bmatrix} \Delta x(x,y) \\ \Delta y(x,y) \end{bmatrix} = \left(\begin{bmatrix} c_{xx'^2} & c_{xy'^2} & c_{xx'y'} \\ c_{yx'^2} & c_{yy'^2} & c_{yx'y'} \end{bmatrix}_{XFD} - \begin{bmatrix} c_{xx'^2} & c_{xy'^2} & c_{xx'y'} \\ c_{yx'^2} & c_{yy'^2} & c_{yx'y'} \end{bmatrix}_{YFD} \right) \cdot \begin{bmatrix} x'^2 \\ y'^2 \\ x'y' \end{bmatrix} + \begin{bmatrix} d_x \cdot \Delta t(x,y) \\ d_y \cdot \Delta t(x,y) \end{bmatrix}
$$
(5.4)

where Δt is the time interval elapsing between the first passage (relative to XFD scan) and the second passage (relative to YFD scan) of the tip on (x, y) position.

The offset between corresponding pixels, as described by equation (5.4), is the result of drift and nonlinearities due to creep and hysteresis. Since closed loop scanners are negligibly affected by

creep and hysteresis, a further simplification can be introduced, valid only for metrological AFMs (5.5):

$$\begin{bmatrix} \Delta x(x,y) \\ \Delta y(x,y) \end{bmatrix} = \begin{bmatrix} d_x \cdot \Delta t(x,y) \\ d_y \cdot \Delta t(x,y) \end{bmatrix} \tag{5.5}$$

An ideal reconstruction would be free from errors due to pixels offsets if deviations, expressed by (5.4) and (5.5), were null. In general, an optimal condition is found whenever the same deviations are lesser than half the pixel size, but depending on the dimension and on the geometry of the measured topographies. Acceptable results are also achieved when higher deviations are present.

Some attentions can help the reduction of distortions.

With regard to open loop instruments, a significant reduction can be achieved both for hysteresis and creep deviations. For the hysteresis, two approaches are possible [48]: the first is an off line correction, based on correction functions evaluated on calibration gratings; the second is an on-line correction based on optimization of the scanner control.

For the creep, it decreases logarithmically in time. The easiest way to substantially reduce creep effects is than to consider a "training" of the scan system, repeating the tracking of the probe along the first line, before proceeding with the measurement of the XFD and YFD. An alternative solution is to discard the affected zones (i.e. the margins where driving voltage inversion occurs) and perform reconstruction over zones where creep effect is minor.

Differently from hysteresis and creep, drift equally affects open loop and closed loop scanners. Main distortions are related with the XFD scan: in fact the YFD, which consists only of a few profiles, is very fast, and is negligibly affected by drift.

Since an off line compensation of drift is hardly realizable, the maximum attention has to be paid to the measuring condition. A properly insulated environment, and a "warm-up" time when starting the instrument can help a substantial reduction of drift velocity components.

Some tests were performed on the open loop AFM applied for this study. Scan settings were fixed to a scan speed of 5 µm/s and a scan range 30 × 30 µm with a resolution of 512 × 512 pixels. One hour heating was sufficient to reduce drift velocity components to d_x, $d_y < 0.1$ nm/s: this corresponds to an average misalignment due to drift that is lesser than 5 pixels. Normally a well stabilized instrument can achieve drift velocities less than 0.02 nm/s, corresponding to an average misalignment of 1 pixel, for the same scan conditions.

As already stated these attentions can improve the quality of the reconstruction. Whenever these are not sufficient to reduce pixel offsets under acceptable levels, new reconstruction strategies

are needed, based for example on larger YFD scans and use of cross correlation matching function for the compensation of residual distortions.

5.2.4 Experimental investigation

An investigation was carried out to test the quality of the reconstruction method. An open loop atomic force microscope was then applied for tests on two different surfaces:

- an optical flat, with a reference roughness Sq=0.60 nm;

- a cylindrical sample, with a reference diameter D=124.75 µm.

A supplementary test considered the reconstruction achieved on measurements performed with a metrological AFM on a silicon flat, conducted by DFM (Danish Fundamental Metrology A/S).

5.2.4.1 Method validation with an optical flat

An optical flat surface with a reference three-dimensional root mean square roughness Sq=0.60 nm was measured [92].

Measurements were repeated 5 times with four different lateral ranges: every time two topographies were taken, the XFD scan first and the YFD secondly. Scan settings are reported in Table 5.3.

Table 5.3: Scan settings.

	XFD	YFD
x- range	1, 2, 5, 10 µm	0.05, 0.1, 0.25, 0.5 µm
x- resolution	0.98, 1.95, 4.88, 9.76 nm/pixel	
y- range	1, 2, 5, 10 µm	
y- resolution	0.98, 1.95, 4.88, 9.76 nm/pixel	
Scan speed	1 µm/s	

The mean surface tilt was removed by a least squares plane fitting while no action was performed in order to smooth the single profiles. Of course a leveling of the single profiles would have improved the quality of the scan, but this correction, helpful for flat topographies, is in general not effective when irregular surfaces are studied.

Results in terms of Sq from topographies reconstructed with the proposed method were compared with those coming from uncorrected (apart from mean slope compensation) topographies and with reference values (Figure 5.4).
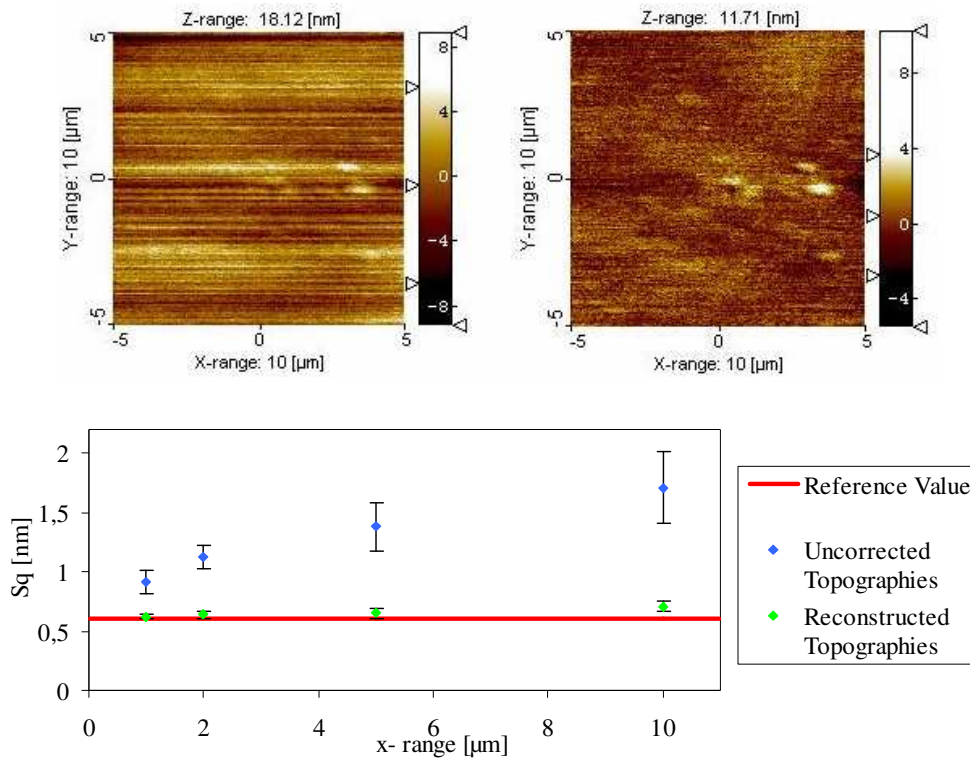
Figure 5.4: Above: a 2D representation of a 10×10 µm uncorrected (left) and of a reconstructed (right) topography. Below Sq roughness evaluated for uncorrected and reconstructed topographies, compared with the reference value. Vertical bars refer to standard deviations.

Because of vertical drift, uncorrected topographies deviate up to 185 % from reference value. The reconstruction provided an almost complete compensation of the drift, with a residual deviation ranging from 3 % to 19 % and a reduction in the best case of 52 %. This latter residual deviation, proportional to the dimension of the scanned topographies, and therefore proportional to the time needed for completing a scanning over one profile, is probably due to two factors:

- the statistically higher presence of defects in the scanned surface;

- a minor vertical drift affecting the scan operation within each single profile.
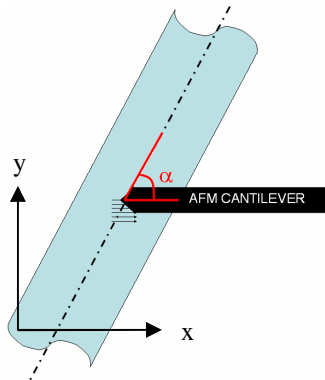
To remove or reduce even this minimal deviation, residual drift could be furthermore cut: additional YFD topographies would be then needed, as for example the ones reported in Figure 5.2a and Figure 5.2b. The implementation of a more complex reconstruction could of course lead to more precise results, but on the other hand measuring and post-processing time would lose out.

5.2.4.2 Method validation with a cylindrical fiber

The cylindrical sample for vertical calibration presented in Sections 4.2 and 4.4, and based on optical fiber technology was applied as a reference surface for the second set of tests. The used fiber (with a diameter of 124.75 µm) was fixed to a rotary table.

Measurements were then carried out, considering modifications in the orientation of the fiber relatively to the AFM scanner.

Table 5.4: Measurements on a fiber.

	XFD	YFD
x- range	30 µm	1.5 µm
x- resolution	29.3 nm/pixel	
y- range	30 µm	
y- resolution	29.3 nm/pixel	
Scan speed	5 µm/s	
Scan angle α	0, 15, 30, 45, 60, 75, 90, 105, 120, 135, 150, 165 degrees	

Defining α as the angle comprised between the cylinder axis and the AFM cantilever direction (Table 5.4), the measurements were repeated three times with 9 different orientations: α=0-165 deg, with 15 deg steps.

Mean curvature was evaluated, perpendicularly to the cylinder axis, and used as a term of comparison. Results from topographies reconstructed with the proposed method were compared with those coming from uncorrected topographies and with reference values (Figure 5.5).
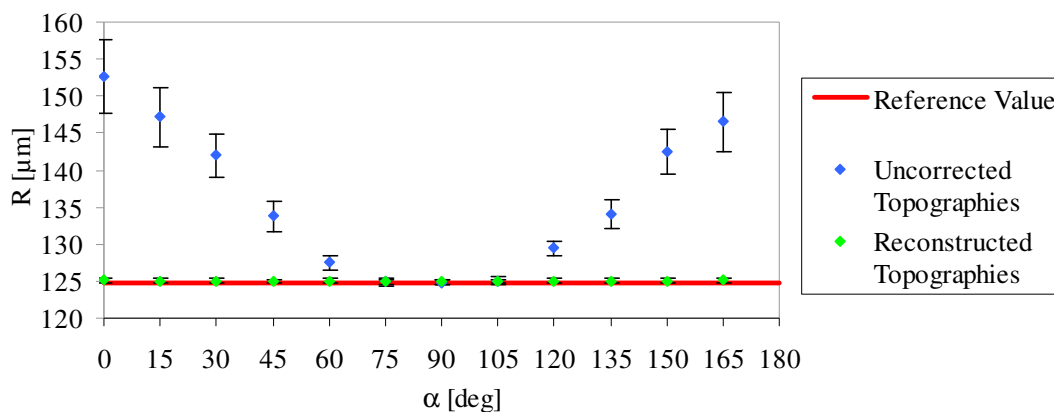

Figure 5.5: Radii of curvature evaluated for uncorrected and reconstructed topographies, compared with the reference value. Vertical bars refer to standard deviations.

Because of vertical drift, uncorrected topographies undergo an apparent flattening due to a wrong relative positioning of subsequent profiles. As already revealed by the previous investigation on the optical flat, the proposed approach allows for an almost complete correction of the problem. Radii deviations, ranging from 0.06 % to a maximum of 22.33 % in the case of the uncorrected topographies, were reduced down to a maximum of 0.29 % in the case of the reconstructed topographies.

5.2.4.3 Measurement with a metrological AFM

A silicon flat surface with a reference root mean square roughness Sq<0.1 nm was measured by means of a metrological AFM, equipped with capacitive distance sensors (see Appendix A). Tests were performed similarly to the ones carried out with the optical flat. No repetitions were considered for this session; scan settings are reported in Table 5.5.

Table 5.5: Scan settings.

	XFD	YFD
x- range	1, 2, 5, 10 µm	16, 31, 78, 156 nm
x- resolution	1.95, 3.91, 9.76, 19.53 nm/pixel	
y- range	1, 2, 5, 10 µm	
y- resolution	1.95, 3.91, 9.76, 19.53 nm/pixel	
Scan speed	1 µm/s	

The mean surface tilt was removed by a least squares plane fitting and again no leveling was performed to smooth the single profiles. Results in terms of Sq from reconstructed and uncorrected topographies, compared with reference value, are reported in Figure 5.6.
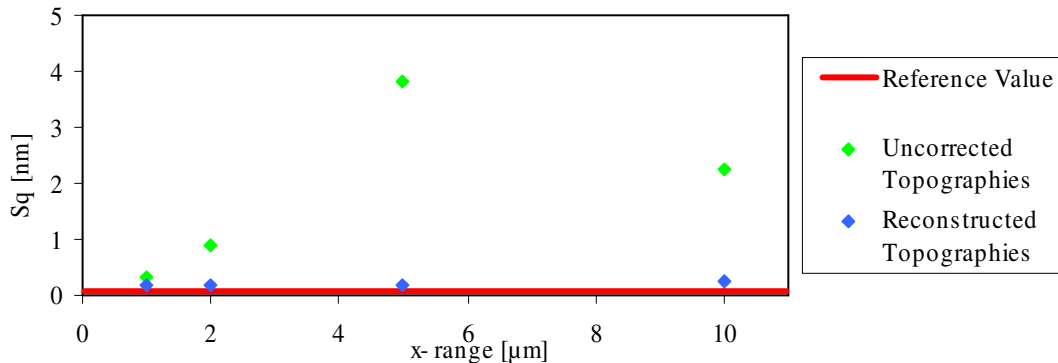

Figure 5.6: Sq roughness evaluated for uncorrected and reconstructed topographies, compared with reference value.

As observed with the open loop scanner, drift affect measurements also with the metrological AFM vertical: uncorrected topographies presented values of mean square roughness up to Sq=3.83 nm. The reconstruction provided a compensation of the drift, reducing the mean square roughness to values down to Sq=0.18 nm. Residual deviations have to be imputed partially to the noise affecting the measurements and only in a minor way to the reconstruction process. It is worth to note that in this case also a leveling of the single profiles would return similar values (Sq=0.14 nm): in fact single profiles leveling generally provides good results whenever flat surfaces have to be processed.

5.3   Applications

In order to complete the investigation, the reconstruction approach was used to characterize two different surfaces, particularly critical for AFM metrology:

- the ruby sphere of a touch probe for coordinate measuring machines;
- the sidewall of the steps on a silicon grating for AFM calibration.

5.3.1 Method application to measurement of a spherical surface

The first investigation took in consideration an accurate ruby sphere of a touch probe for coordinate measuring machines, with a nominal radius of 500 µm. Characterization of CMMs and Nano-CMMs probes, in particular when the dimensions are reduced down to the micro-level, is relevant and definitely not easy [93] [94]. The proposed approach was applied for fine reconstruction of a portion of a probe sphere. In Figure 5.7a, surface topography of the sphere, resulting from AFM imaging, is shown. Traditional AFM imaging technique provides poor results: upon extraction of the sphere diameter from profiles, in the fast and the slow scanning direction respectively, differences of 23 % were seen (Table 5.6). This deviation is in fact due to the thermal drift, affecting accuracy in the slow scanning direction. Moreover, a step is clearly discernible, which is most probably due to surface contamination. The image of the same surface region, after software correction, is shown in Figure 5.7b.
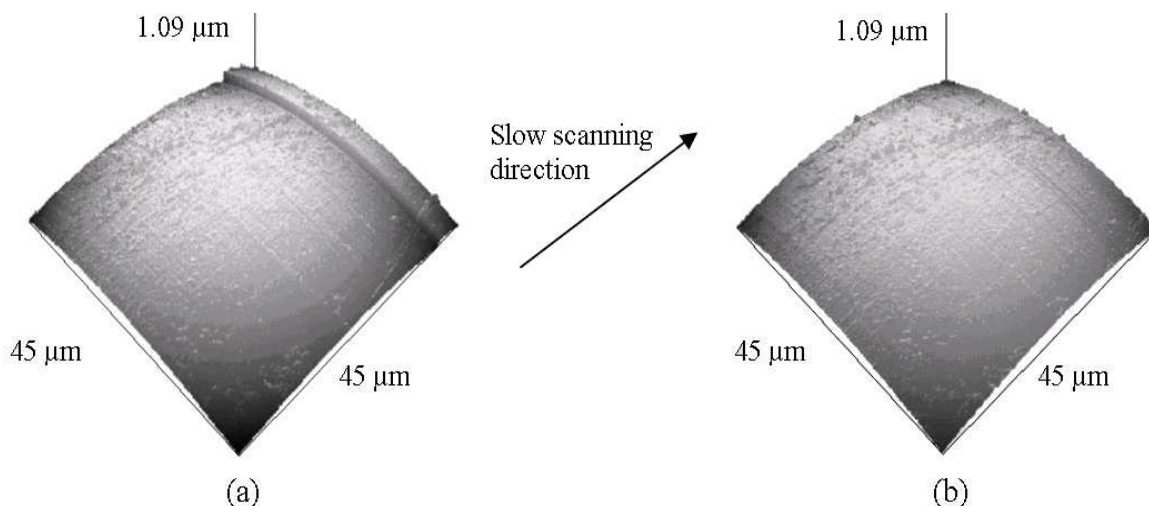

Figure 5.7: AFM image of a sphere: surface topography before (a) and after (b) software compensation.

A quantitative analysis of sphere diameter values, resulting from application of the method, is shown in Table 5.6. Results in terms of diameter deviation from the result obtained in the fast scan direction are summarized. After correction, the deviation of sphere diameters is reduced from 23 % to 0.2 %.

Table 5.6: Diameter evaluation (nominal 1mm)

Evaluated diameter	Before Method Implementation (XFD image)	After Method Implementation (reconstructed topography)
Fast Scan Direction	1072 ± 10 µm	1072 ± 10 µm
Slow Scan Direction	1322 ± 70 µm	1070 ± 10 µm

5.3.2 Method application to measurement of Line Edge Roughness

Line edge and sidewall roughness are critical problems occurring in lithography as pattern size shrinks [95]. Due to its difficult accessibility, detailed pattern flank characterization is no trivial task. The newly developed method was applied to line edge and sidewall roughness analysis on 1-D arrays of rectangular SiO_2 steps on a Si wafer, allowing for accurate characterization of both flank geometry and roughness. Roughness measurements at different heights of the flank from the bottom terrace were also possible [96].

To ensure access of the tip to the step flank, the sample has to be positioned tilted by an angle α:

$$\alpha > \left(\beta + \frac{\delta}{2} - \varphi - 90 \right)$$
(5.6)

With the set up used for this set of experiments, it was considered α > 20 degrees. Then two surface topographies were taken with different scan conditions, according to the described approach (Figure 5.8).

α - sample tilting angle
β - line flank slope
δ - AFM tip cone angle
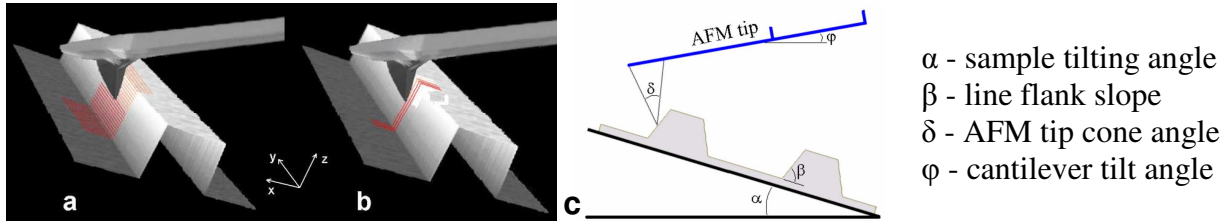φ - cantilever tilt angle

Figure 5.8: Representation of the two measuring operations: a) the first one having fast scan direction parallel to the pattern lines and b) the second one perpendicular. c) Measurement set up, with angles definitions.

The sidewall topography was accurately restored in terms of both roughness and geometry: the improvement in the quality of the scan can be appreciated in Figure 5.9, where the uncorrected and the reconstructed topographies are reported. In the corrected topography the shape of the step is clearly defined: this means that it is possible to precisely associate roughness measurements to different heights of the flank. Roughness values, in terms of root mean square (Sq), were therefore mapped from the bottom terrace. Mean values are reported in Figure 5.10: it is worth noting that the first part of the graph gives information on the SWR, while RMS values relative to the maximum heights are to be regarded as line edge roughness (LER).

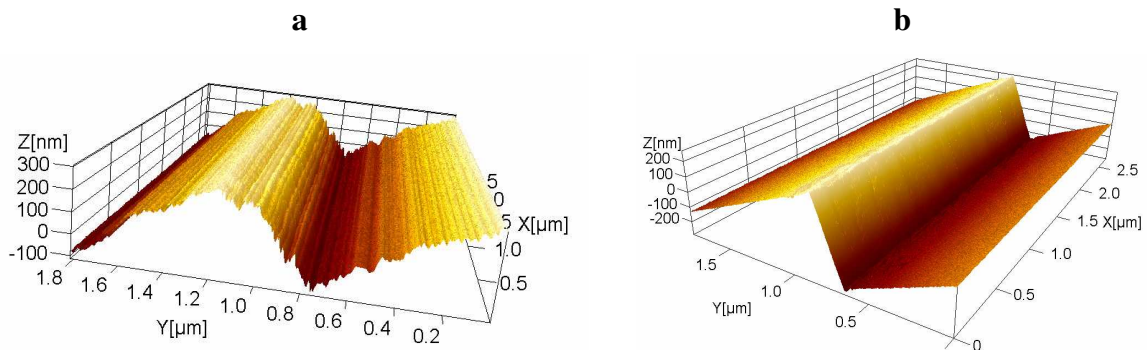**a**   **b**

Figure 5.9: AFM image of a silicon step: surface topography before (a) and after (b) software compensation.
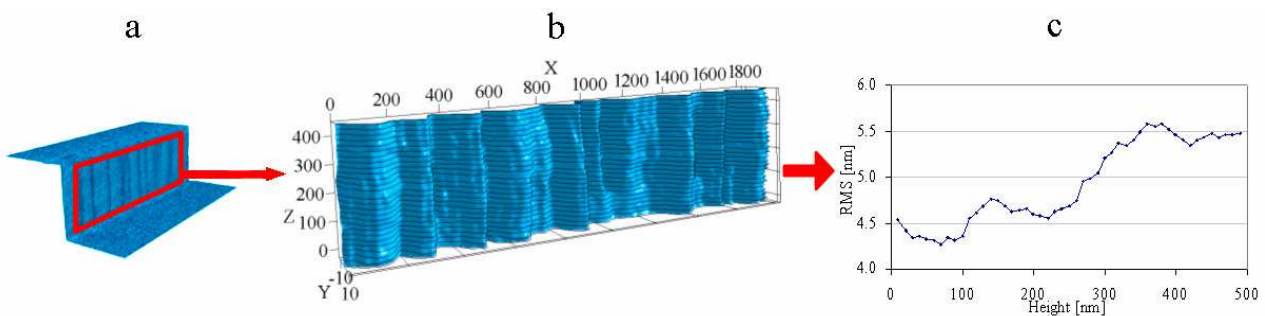
Figure 5.10: a) Reconstruction of the flank geometry with the developed method and b) zoom on the sidewall; c) roughness measurements of the line flank evaluated at different heights from the bottom terrace.

5.4 Horizontal drift

As described in Chapter 3, scanners based on piezoelectric actuation, the most widespread systems, suffer from hysteresis and creep. Additionally, as frequently repeated, all AFMs suffer from drift distortions in the vertical, but also in the lateral plane. Creep is a rate-dependent relaxation of the piezo scanner, introducing heavy artifacts in AFM images. An example of creep-related image distortion is given in Figure 5.11. In the figure (Figure 5.11a), an AFM image of a one dimensional calibration standard is shown. The scan proceeds from the bottom to the top of the image. In the bottom of the figure, lines deviate significantly from being vertical. They get more and more vertical as the scan proceeds. Creep decreases logarithmically in time. What operators usually do in order to avoid creep effects in quantitative measurements is to cut the affected zones out and perform calculations over zones where creep effect is negligible. Depending upon the scan motion, one or both the sides of the images are also affected by creep. Zones where tracing occurs after driving voltage inversion are those most significantly affected. In the same figure (Figure 5.11b), effects of lateral drift on the same topography are riproposed. In this second case, line deviations are different. In fact only a slight average shift on the right is

perceptible, but the distortion is for sure dominated by a random lateral shift, which looks like a noise disturb affecting positioning of profile in the x-direction. This kind of distortion, usually present in a less aggressive way, cannot be avoided. Proper insulation systems can soften its influence, but no methods are known for eliminating it.
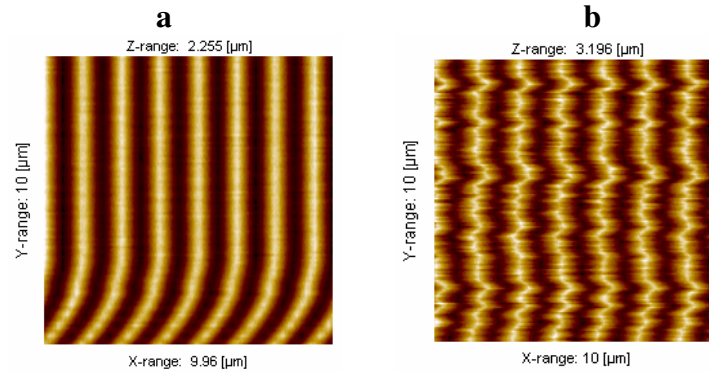

Figure 5.11: AFM image of a one dimensional calibration standard. a) Bending of the vertical lines towards the bottom of the picture is related to creep (The scan proceeded from bottom to top). b) Lateral shifts of profiles due to drift distortions

In this chapter implementation and validation of a method for accurate compensation of lateral distortions, developed for AFM metrology but in principle applicable to the whole family of SPMs is presented. The method is mainly applicable to those topographies which present the same profile along the slow scan direction such as, for instance, the line patterns reported in Figure 5.11. The method provides correction of the undesired lateral shifts, mainly due to creep and thermal drift, with optimized repositioning of profiles in the slow scan direction.

Successful application of the compensation method was proved in [97].

5.4.1 Method for lateral shifts compensation

The method presented hereafter is based on own developed software coded in C++.

The sequence of operations performed by the lateral shifts correction routine is shown in the following figure (Figure 5.12).

First of all the measured topography undergoes to installation slope correction. In fact any tilt can badly influence the matching operation, performed in the following steps, bringing to inconsistent results.
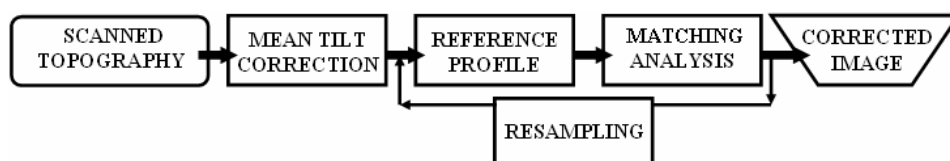

Figure 5.12: Profiles lateral shifts correction procedure.

In the second step a profile is taken as reference for the successive matching analysis. During first iteration the median profile (i.e. the profile scanned after the first half topography is measured) is selected as reference (Figure 5.13). In successive iterations an average x profile is computed and defined as reference. Defined n as the total number of profiles, the average x profile is evaluated according to Equation (5.7):

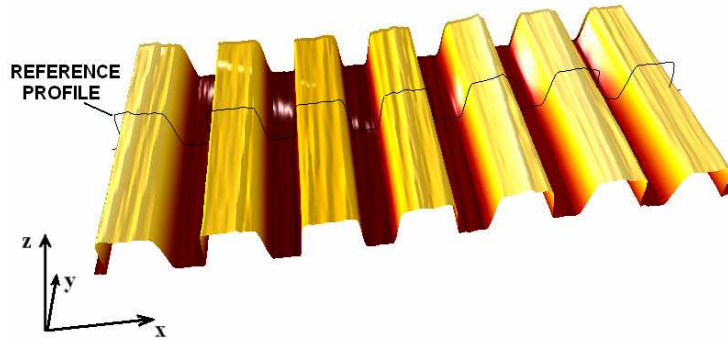$$z(x) = \frac{\sum_{j=1}^{n} x_j}{n}$$
(5.7)

Figure 5.13: The black elevated line represents the profile taken as a reference in the first iteration of the implemented algorithm.

The third step is indicated in Figure 5.12 as "*Matching Analysis*" and constitutes the core part of the correction method. In this phase a matching operation is carried on, in order to define most probable shifts occurred. A comparison window is defined, centered in the reference profile: the number of pixels K constituting the comparison window is set by the user. The comparison window of the reference profile is coupled with all the profiles constituting the topography: from the first (on the bottom of the image) to the last (on the top of the image). During *Matching Analysis*, the comparison window is then "scrolled" over the profile, by imposing single pixel shifts (Figure 5.14). After each shift, a sum of squared differences index s_{ij} (for the i-th position of the comparison window within the j-th profile) between the comparison window and the correspondent part of the investigated profile is evaluated as follows (5.8):

$$s_{ij} = \sqrt{\left[\sum_{k=-K/2}^{K/2} (z'_{(i+k)j} - z''_{(i+k)j})^2 \right]}$$
(5.8)

The coefficient s_{ij} assumes values ranging from 0, for full correlation, up to infinite for no correlation.
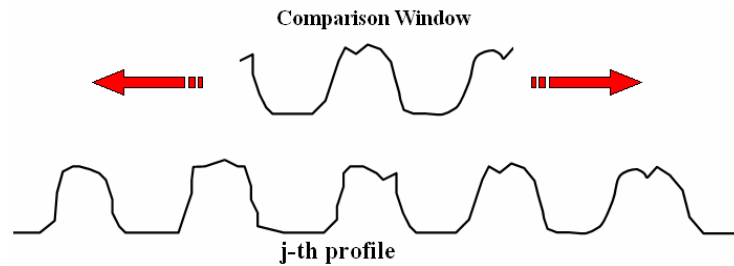
Figure 5.14: The comparison window scrolled over the analyzed profile

The position that minimization the deviation index is used to compute the local shift of the *j*-th profile. The first iteration is completed when all the profiles constituting the scanned topography have undergone to the matching analysis.

Successive iterations can be repeated using the average x profile as reference.

A resampling operation can also be considered for successive iterations: in fact increasing the number of pixels can improve the accuracy of the correction, leading to sub-pixels compensations.

5.4.2 Results

The output of the algorithm is a corrected topography and a matrix of vectors. Each vector represents the shift of the corresponding profile from the position that maximizes correlation with the comparison window of the reference profile. In the figure below (Figure 5.15) these shifts are shown by parallel arrows.
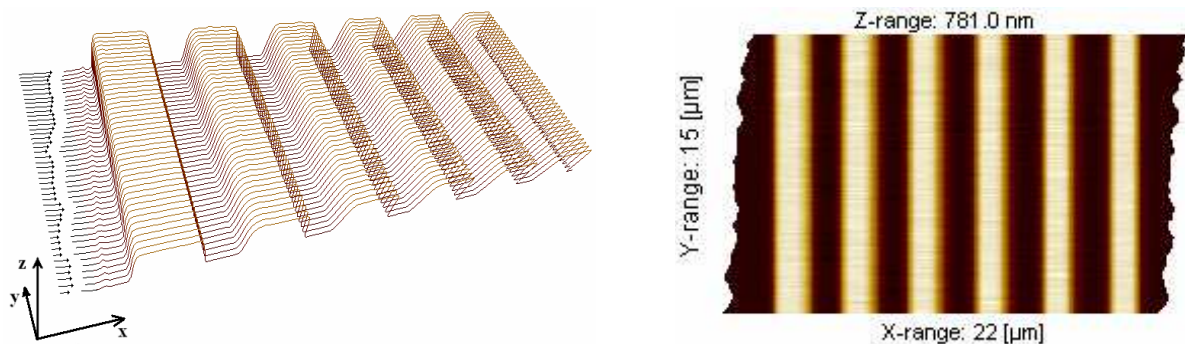

Figure 5.15: Surface after correction: arrows on the left represent the local shift imposed on single profiles in order to compensate misalignments.

Representing the matrix of vectors as a function of the y coordinate, the following graph can be created (Figure 5.16). This gives an idea of the average distortion and can also be useful in order to highlight tendencies. In the present case the best fitting function is drawn in blue; its slope was considered to be descriptive of the average drift velocity in the x direction.
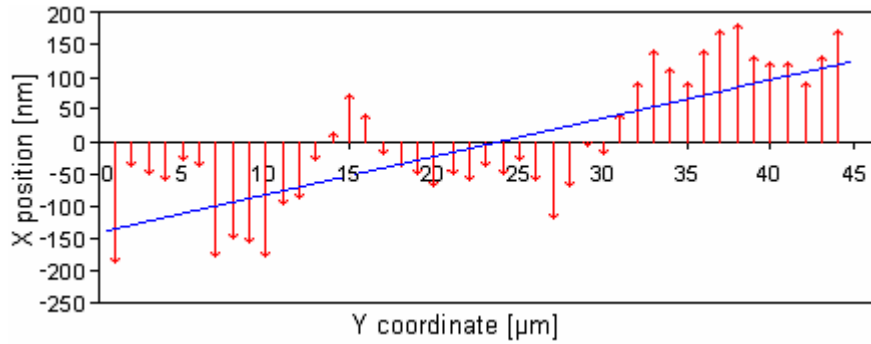
Figure 5.16: Local shift for single profile misalignment with the best fitting line.

At the beginning of this paragraph, it was anticipated that whenever surfaces with highly correlated topography in the y direction are measured, lateral shifts correction is possible. However, it was found that the same method and the same automatic routine can be applied with acceptable results also whenever uncorrelated topographies have to be processed. Only one modification was implemented in the routine settings. The reference profile was not identified in the middle of the topography, but for the *i*-th profile, the (*i-1*)-th profile was taken as reference. Three examples, giving only a qualitative idea of the compensation results, are reported in Figure 5.17. Lateral drift was quite satisfactorily reduced, while some zones still present distortions, sometimes higher than in the original topography. Further investigations in this case would be needed to improve the quality of reconstruction.
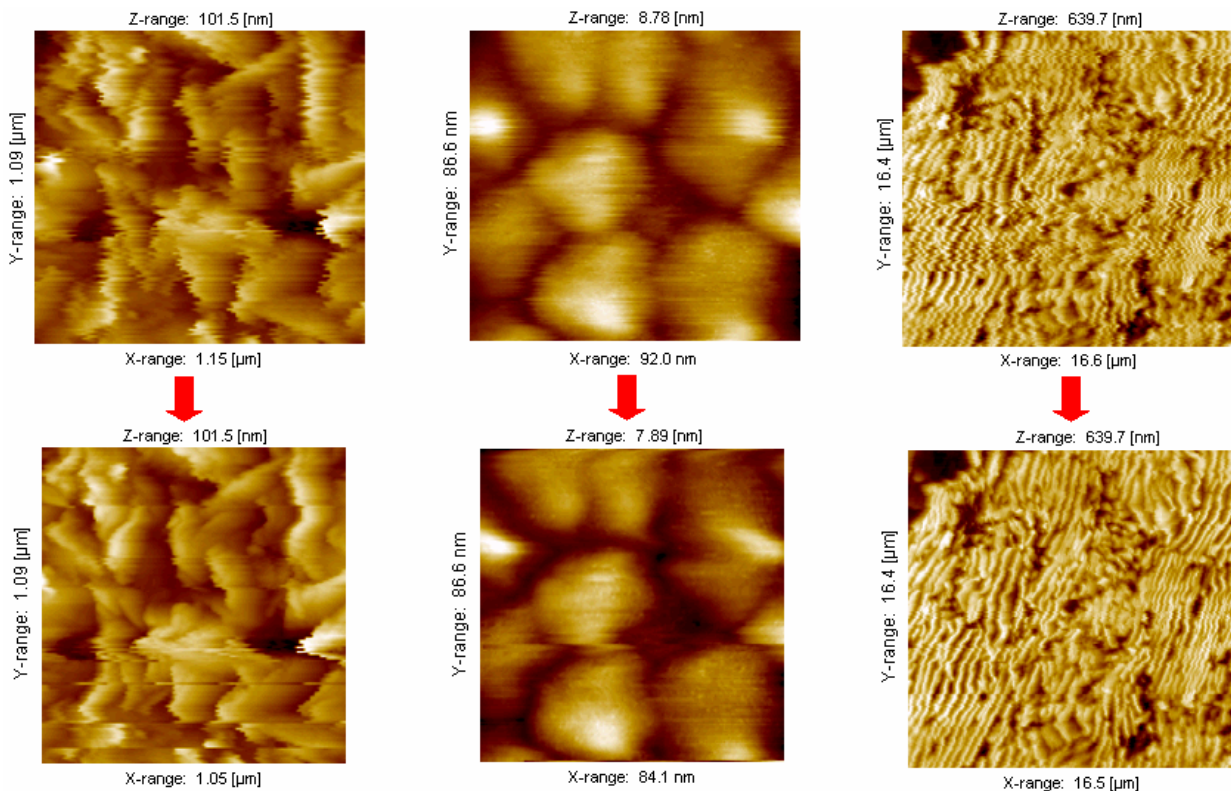

Figure 5.17: Results of the lateral shift compensation on random pattern topographies.

5.5   Tip wear

An Atomic Force Microscope (AFM) measurement is the result of scanning over a surface using a mechanical probe of finite dimensions; the resulting topography including features of both the measurand and the probe shape. This interaction is normally known as convolution effect and introduces distortions that are particularly evident whenever structures with sharp details are measured in the nanometer range (see also Section 3.3.6). This in some way limits advantages brought on by the extremely high lateral and vertical resolutions allowed by the instruments.

Furthermore, the amplitude of these distortions is not constant. Due to physical effects and dynamic interactions, tip shape evolves with time: in particular continuous deterioration is introduced by wear effects. This worsens even more the problem, since a correct compensation, usually called deconvolution operation, would ask for a frequent monitoring of tip dimensions.

In the present chapter, a new method for monitoring and modeling tip wear in contact mode AFM is presented, based on three main steps.

1) Scans over a test structure presenting sharp edges: randomly oriented crystals ensure appropriate reverse imaging of the tip shape.

2) Tip shape deconvolution: geometry reconstruction is achieved through application of a newly developed automatic algorithm.

3) Wear analysis: by comparing successive reconstructions repeated throughout tip lifetime, wear rate and tip radius variation can be monitored and characterized.

5.5.1 Tip reconstruction

Two operations are needed to precisely define the tip shape. The first one consists of one or more scans over a nanostructured surface suitable for tip reverse imaging purposes; the second one is an accurate tip deconvolution procedure able to reconstruct micro- and nano-geometries of the tip.

5.5.1.1 Test structure

An ideal tip characterizer is an infinitely narrow spike, reproducing during AFM scanning a perfect image of the tip. Some samples are available on the market for tip characterization, as for instance the Nioprobe [98], a film densely populated by tiny peaks, resistant to the duress of contact mode scanning. Other samples are available or can be produced, mainly based on growth of nanocrystals. Preliminary tests performed for this study were conducted on nanopowders, produced by electrodeposition of iron-nickel alloy powders [99].

The main characteristic of these samples for the exploitation of tip reverse imaging, is the presence of protrusions and sharp flakes randomly oriented. In fact, whenever an AFM scan is carried out over the test structure, different portions of the tip come into contact with protrusions (Figure 5.18). This means that different information about different portions of tip is contained within the scanned topography. In particular vertical sharp crystals are ideal for reconstructing tip apex curvature.

A number of methods have been suggested for deconvoluting tip shape, i.e. for extrapolating tip geometry data from such scanned topographies [42] [100] [101] [102]. The one implemented by the authors, inspired by the method of blind reconstruction [42] [103], takes advantage of the particular surface structures described above.
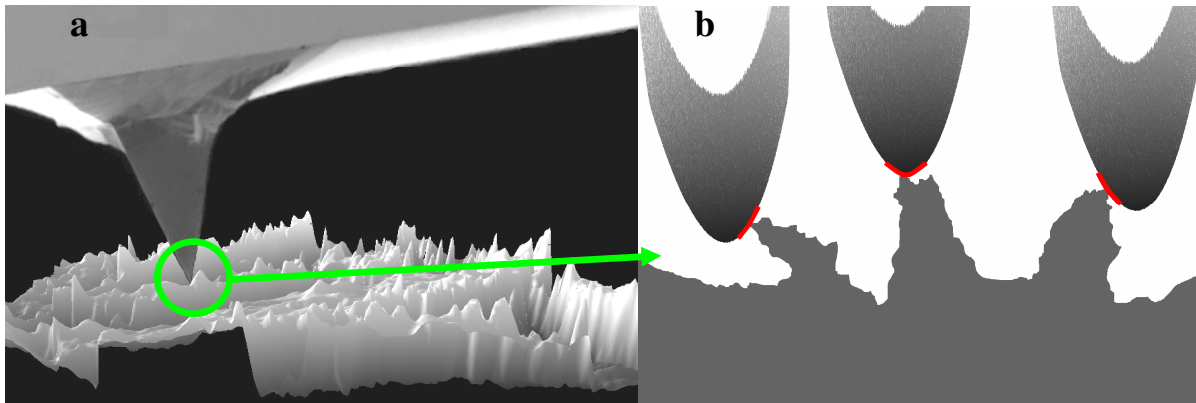

Figure 5.18: Representation of the AFM scan over the tip characterizer surface. a) Scan is performed over the nanostructured surface; b) differently oriented protrusions allow for characterization of different tip portions (red lines).

5.5.1.2 Test structure

During the scanning operation, different portions of the tip enter into contact with the randomly oriented protrusions on the test structure (Figure 5.18b). Some regions of the scanned topography are better describing the right flank of the tip, some others the left flank, and some other else the very apex. Unfortunately, dynamic interaction between the scanning probe and the surface, together with background noise, introduce distortions. Due to their random nature, they are impossible to isolate or filter out, nevertheless, in a first approximation, they can be regarded as disturbing effects deviating the tip shape from its reference geometry.

Based on these considerations, an automatic routine has been developed and implemented into commercial software [35]. Hyperboloid was used as reference geometry, for its interesting properties: this quadratic surface is easily parametrizable, while vertex curvature and asymptotes angles can be controlled for better describing tip geometry.

The implemented software tool's main steps can be summarized as follows:

1) A threshold value is input by the operator, defined as the maximum deviation accepted from the reference shape.

2) Curvatures and slope analysis are carried out all over the scanned topography. Detected asymmetries are used to recognize which parts of the tip were in contact with the test structures and therefore can be reliably applied for tip reconstruction (Figure 5.19).

3) A hyperboloid shape is eventually generated, based on previous analysis and conditions.
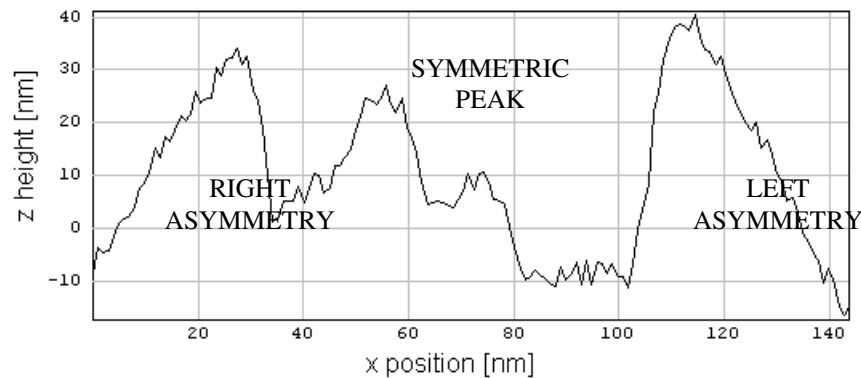

Figure 5.19: A profile extracted by the test surface: right asymmetrical peaks are considered for characterization of tip left flank and vice versa; symmetric peaks are applied for tip vertex reconstruction.

The automatic routine can characterize the area localized in the very apex of the tip, which presumably is the part that more frequently comes into contact with the measured surface and more probably undergoes to wear. Once the geometry is characterized, it is immediate to compare solids, in order to define the curvature reduction or the loss of volume, corresponding to the worn part.

5.5.2 Wear rate model

The wear process was analyzed keeping a reference with approach usually applied in the macro-mechanics fields. Sliding wear can be regarded as a dynamic process, depending on many factors and the prediction of that process as an initial value problem. In macro as well in micro-engineering, sliding wear volume is usually described by Archard's equation (5.9) [104]:

$$V = k \frac{Fx}{H} \tag{5.9}$$

The volume of removed material V is directly proportional to the load F and the sliding distance x and is inversely proportional to the hardness of the surfaces being worn away H; k is a dimensionless number defining the probability that two asperities coming in contact will form a fragment during sliding.

Archard's model has been applied in the recent years to quantification of tip wear rate [105], but some limitations can be recognized. Indeed this model:

1) doesn't take sliding speed into account: this is quite limitative, since high speed could increase tip flights and crashes against the measured surface;

2) doesn't quantify approaching operation: when the tip is first lead into contact with the sample surface at a speed commonly of some 10µm/s, the collision can bring to a peak in the wear rate;

3) is based on surface hardness: while at the macro-level hardness is generally quite constant, in the nanometer range inhomogeneities or different material phases can produce significant variations within the scanned surface;

4) needs evaluation of the wear coefficient k, which is not always easy.

In the model proposed in this work, above described limitations are by-passed by taking all effects into account through the lateral force analysis. Surface topography and lateral force mapping are normally provided by commercial AFMs with no need for set up modifications. Lateral force is measured by computing torsional deformations of the tip. At first instance it can be considered as the result of the deformation friction and the adhesion between the tip and the surface and it has been shown that it is dependent on the defined stick-slip [106] [107].

In the model proposed by the authors, the wear rate effect is hence modeled on the specific measuring task, using average lateral force data as calibration factor. A new equation for the removed volume can thereafter be introduced (5.10):

$$V = k'x \cdot \left(\frac{L_m}{L_{REF}} \right)^3 = k'_{corr} \cdot x \qquad\qquad (5.10)$$

where x is the sliding distance, corresponding to the total path run by the tip, while k' is a coefficient evaluated during a calibration; L_{REF} is the average lateral force measured during calibration and taken as a reference; L_m is the average lateral force, evaluated under working conditions. k'_{corr} is the new coefficient, calibrated for measurement settings in AFM exercise.

In an analogue way, tip radius increase can be evaluated as follows (5.11):

$$r = r_0 + k''x \cdot \frac{L_m}{L_{REF}} = r_0 + k''_{corr} \cdot x \qquad\qquad (5.11)$$

where k'' is again a coefficient evaluated during the calibration task, k''_{corr} is the new coefficient evaluated after calibration and r_0 is the initial tip radius.

The model here presented is meant to be applied to repetitive measurements on the same or similar surfaces. This is not much limitative, since very often atomic force microscopes are applied for characterizing samples of the same type. The calibration process is based on a single series of measurements, during which the test structure and the surface of interest are

alternatively scanned, in order to check evolution of tip wear as a function of the scanned length (the sliding distance *x*): AFM settings reproduce normal operating settings.

5.5.3 Experimental investigations

The developed method was applied to the study of tip wear when measuring a polished steel surface. It is generally recognized [108] how wear volume grows as the sliding distance increases, while the degree of growth in the wear volume reduces with the increase in the sliding distance. The wear process eventually stabilizes to an approximately constant value (Figure 5.20).
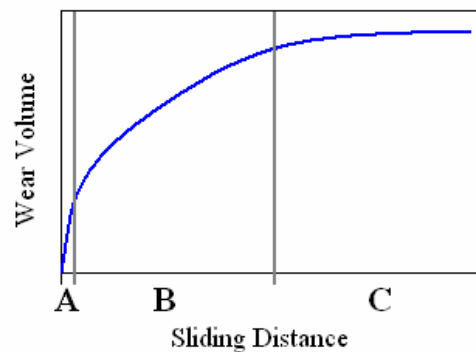

Figure 5.20: The tip wear process: after a first fast wear process (A), the degree of growth in the wear volume reduces (B), till it stabilizes to an approximately constant value (C).

With reference to Figure 5.20, we focused on part B, where the wear process can be approximated to a linear function. A commercial AFM working in contact mode was employed for the study (see Appendix A): three silicon tips were selected with a nominal tip radius <10nm. Quite severe conditions were chosen to accelerate wear process: measuring conditions are reported in Table 5.7.

Table 5.7: AFM measuring settings: scan size was kept at 5µm × 5µm, with a 1024 × 1024 pixels resolution.

	Speed [µm/s]	Contact Force [nN]
Tip 1	5	5
Tip 2	10	15
Tip 3	15	25

Two scans over the steel surface and one over the tip test structure were alternated: this means that 2×1024×5µm ≈ 10 mm sliding distances were considered between subsequent tip characterizations. Tip wear was evaluated as described in the previous section. The lateral force was parallely analyzed during measurements.

The average lateral force L_m was evaluated as follows:

$$L_m = \sum_{i,j=1}^{1024} \frac{L_{i,j}}{1024^2} \qquad (5.12)$$

where i refers to the points in the so called fast scan direction and j to the profiles; $L_{i,j}$ is lateral force local value, relative to the *(i, j)* position; 1024×1024 is the total number of points for each scanned topography.

In Table 5.9, worn material volume and radius results are reported as functions of the sliding distances. As can be appreciated from the first two graphs, wear rate was considered constant: its computation can be easily carried out by evaluating the slope of the best fitting line. Average lateral force is also reported: a slight decrease can be noticed. This could be associated to the wear effect: a reduction of the tip radius results in an increase of the contact area, therefore lower local pressures should lead to lower friction actions.
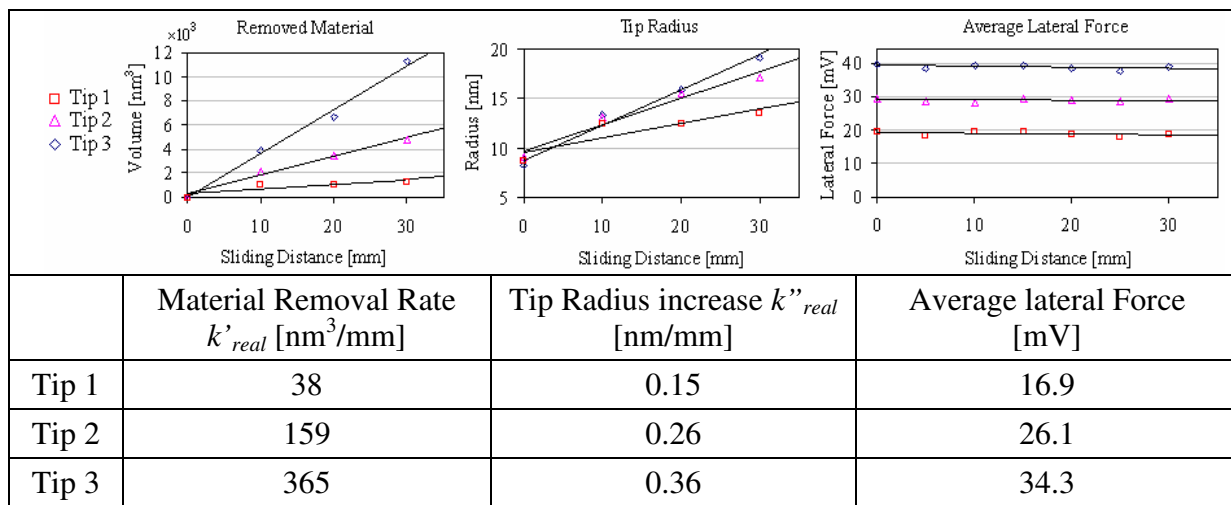
Tip 1 can be taken as the reference case: on the other hand tip 2 and tip 3 can be intended as case studies. According to (5.10) and (5.11), the method is calibrated on the reference case: thereafter coefficients k' and k'' and L_{REF} are evaluated from tip 1 analysis. Respectively we got: k'= 0.15 nm/mm, k''=38 nm^3/mm and L_{REF}=16.9 mV. AFM mV output was kept for the lateral force and no conversion was considered not to introduce further complexity to the problem: this is not bringing approximations to the study.

From tip 2 and tip 3 average lateral force evaluation the following values were achieved: $L_m(tip2)$= 26.1 mV; $L_m(tip3)$=34.3 mV. Calibration factors were eventually computed; corrected coefficients k'_{corr} and k''_{corr} were evaluated and compared with the real ones k'_{real} and k''_{real} measured as the slopes of the lines best fitting wear removal data (Table 5.8 and Table 5.9). From the comparison, slight deviations were recognized: even though further investigations are needed, the proposed relations (5.10) and (5.11) seem to be verified.

Table 5.8: Results of the calibration task

	Tip 2	Tip 3
$\dfrac{L_m}{L_{REF}}$	1.54	2.03
$\left(\dfrac{L_m}{L_{REF}}\right)^3$	3.68	8.36
k'_{corr}	140	318
k'_{real}	159	365
k''_{corr}	0.23	0.30
k''_{real}	0.26	0.36

Table 5.9: Estimated volume of worn material and tip radius evaluated as a function of the sliding distance.

	Material Removal Rate k'_{real} [nm^3/mm]	Tip Radius increase k''_{real} [nm/mm]	Average lateral Force [mV]
Tip 1	38	0.15	16.9
Tip 2	159	0.26	26.1
Tip 3	365	0.36	34.3

5.5.4 Investigation on effects of speed and contact force

A second series of measurements was considered, analyzing effects of speed and contact force on lateral force. 25 measurements were taken, with loads ranging between 5 nN and 25 nN and speeds ranging from 5 µm/s to 15 µm/s on a steel surface with a roughness Sq=153 nm. Some measurement was also taken on a flat glass surface with a roughness Sq=2.3 nm. Results for low and high values of speed and force are reported in Table 5.7.
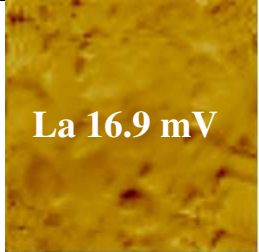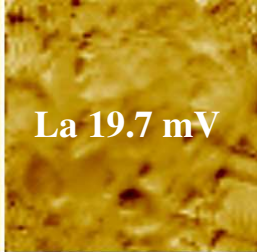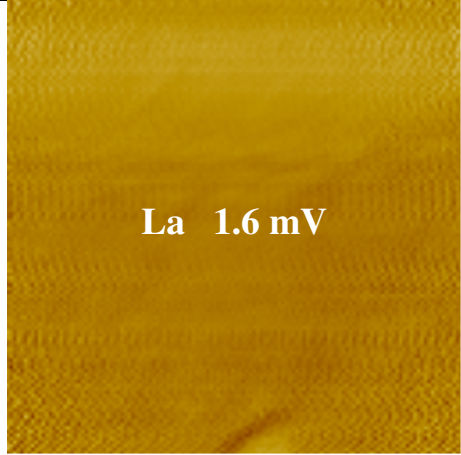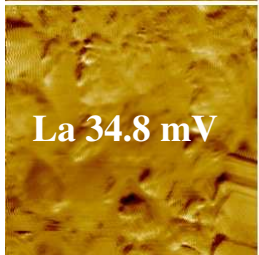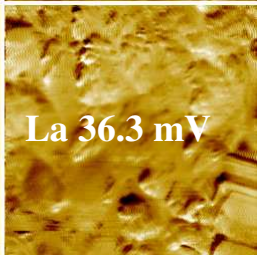
The interest connected with this kind of analysis is double.

First of all it is possible to map the average lateral force for different values of speed and contact parameters: this provides a reference set of values for evaluation of the calibration factors indicated by (5.10) and (5.11).

Secondly, monitoring lateral force can be useful in order to understand how much the tip is being stressed by measurement settings. As a consequence, the user can find the best trade off, between scanned image quality, scan time and tip stress. This is evident also analyzing lateral force for the flat glass surface. In this second case lateral force is greatly reduced: the user should interpret this fact with the possibility (for example) of increasing scan speed, with no danger for tip damage.

Lateral force, studied as a function of different scan settings, can help for proper optimization of AFM measurement.

Table 5.10: Lateral force topography for a rough surface under different speed (5 µm/s and 15 µm/s) and load conditions (5 nN and 25 nN) and for a flat surface (speed 10 µm/s and force 10 nN).

5.6 Conclusions

In the present chapter a new method for accurate imaging of three-dimensional surface topography is presented. Surface topography is compensated for thermal drift in the vertical as well as in the horizontal plane.

In the vertical direction, reconstruction is based on two images, taken with mutually orthogonal scanning directions. The method requires only a slight increase in the scan time from 1 % to 5 %, but provides a reduction of profiles misalignments and a general improvement of the measurement results compared to reference values.

An investigation is presented, involving an optical flat and a cylindrical fiber surface analyzed with an open loop AFM and a silicon flat investigated with a metrological AFM. Two critical case studies were also carried out: on a ruby sphere and on a silicon grating. In the lateral direction, compensation is provided with optimal results in the case of pattern repetitive in the slow scan direction. Improvements were also demonstrated in the case of uncorrelated topographies.

A method for modeling distortions due to tip wear rate in contact mode AFM is eventually proposed. This is of great help whenever quantitative analyses are needed, reducing the time needed for tip-investigations and allowing for proper deconvolution operation. Evolution of tip was observed by reverse imaging of a scanned nanostructured topography, periodically repeated throughout tip lifetime. Lateral force was mapped conjunctly with removed material rate and tip

radius reduction and was applied for calibration purposes. Although further investigations are needed, first experimental results are fairly in accord with the proposed model.

5.6.1 Contributions

Chapter 6

Instrument Enhancement

6.1 Introduction

In Chapter 2 a table was proposed, summarizing the main AFM metrology challenges and barriers. In Table 6.1 below an excerpt is proposed, identifying the most urgent issues in the author's opinion.

Table 6.1: Main SPM/AFM metrology challenges and barriers.

Category	Metrology challenges
Interface	3D characterization Large range measurements
Instrument	High sensitive/high accuracy/high resolution High speed/real time measurement
Probe	Tip influence/deconvolution

This chapter aims to present possible solutions to these problems. In order to reduce the effect of the interaction of the probe with the sample, and thus help the reconstruction of high aspect ratio structures, a double tilt technique has been proposed. Here reconstruction is based on matching and coupling of two surface topographies, scanned with different installation slopes.

A matching automatic routine was also implemented for stitching three-dimensional topography data sets taken on contiguous areas, allowing for surface mosaicking operations. The developed routine fully compensates positioning errors occurring when the measuring instrument is displaced relatively to the surface.

The issue of time reduction is discussed in the last section, where a new measurement approach is investigated for overcoming raster scan limitations. With the new method, the probe is driven over the sample surface along free-form paths, scanning with high resolution only discrete features of interest, collecting only relevant data and allowing for consistent scan time reduction.

6.2   Steep slopes characterization

An issue in surface metrology is the characterization of high aspect ratio features. In particular measure on steep slopes is not an easy task. A lot of instruments fail, when encounter steep slopes during scanning. This is true for optical methods, limited by a maximum detectable slope generally <30°, but is true also for scanning probe microscopes, limited by the finite physical dimensions of the tips.

A lot of efforts have been done for overcoming this limitation, as for instance the realization of ultrasharp tips [109], or the installation of carbon nanotubes at the very end of the probes [110], or the realization of multiprobe systems [111] (Figure 6.1).
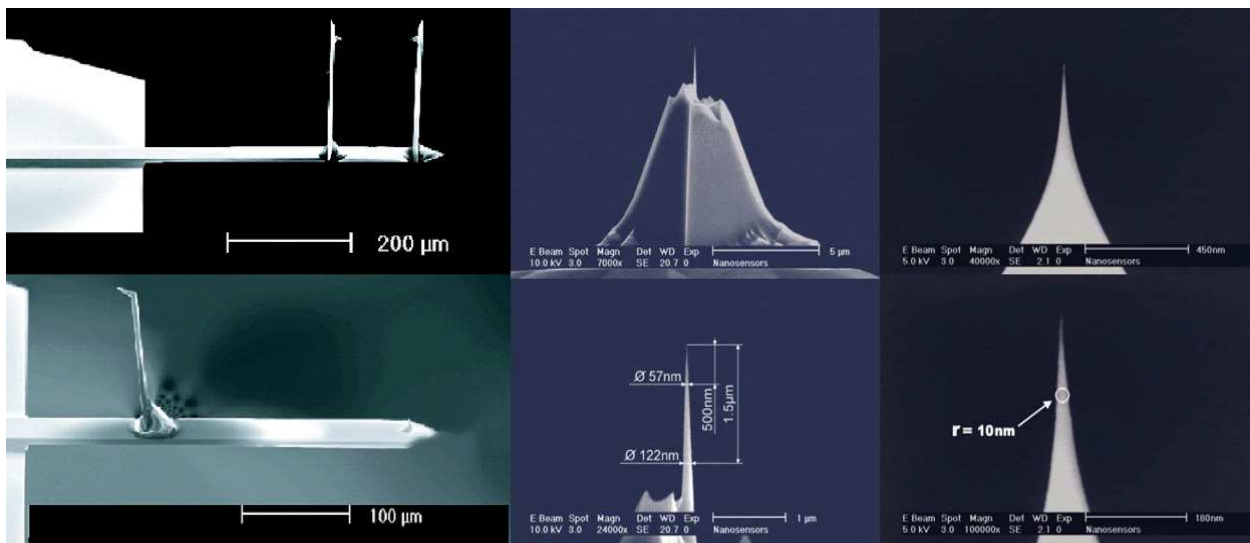

Figure 6.1: Efforts in AFM probes developments, with the realization of multiprobe systems and sharp tips [109] [111].

The problem is even worse for optical profilers, such as confocal microscopes or white light microscopes: local loss of signal, resulting from this limited detection, originates data files containing void pixels, which eventually provide poor surface characterization. A new approach was developed, overcoming instrumental limitation on the maximum detectable slope, based on a software tool, that processes images taken with controlled tilt, and returns a high quality 3D profile of the sample being investigated [112].

The same approach, developed for optical profilers, was seen to be effective also for SPMs.

6.2.1 An issue in optical profilometry

Optical profilers deliver an accurate and fast analysis of surfaces, with sub-micrometer resolution. In particular, those instruments based on vertical scanning methods (vertical scanning

interferometers and confocal profilers) provide extremely fast, non-contact characterization of surface micro-topography [113].

Limitations are mainly related with light properties and its behavior at the interface. In fact material reflectivity influences signal response: maximum detectable slope (from here on indicated with γ) is determined by surface reflectivity, roughness and objective numerical aperture.

Another problem, featuring narrow cavities, is the shadowing effect: surface protrusions mask re-entrances and undercuts which are then not probed.

Local loss of signal, resulting from both a limited maximum detectable slope as well as shadowing, originate data files containing void pixels, which eventually provide poor surface characterization [48] [114].

Lack of valid data may occur, for other reasons with other surface metrology methods. For instance contact probes are limited by lack of access inside pits and tip-convolution, as reported in Paragraph 3.3.7. However, a few solutions have been proposed in the past, focused on the characterization of such "hidden part", which for any reason is not accessed or not measured properly by the sensing means. These mainly consist of development of new more powerful sensing systems [115], use of replica techniques [116] and last repositioning of the sample relatively to the measuring instrument [97]. The approach here investigated, belongs to the latter category.

6.2.2 The void pixels

When using optical instruments for surface characterization, very accurate and highly resolved topography measurement can be achieved. Nevertheless it is common experience to anyone who uses optical 3D profilers, dealing with images containing unsampled parts: in the following, all these invalid measurement points will be referred to as "void pixels", assuming implicitly that artifacts are rejected and somehow filtered out.

An example is given in Figure 6.2, were a bad characterization was achieved on a microchannel (more than 40% of void pixels).
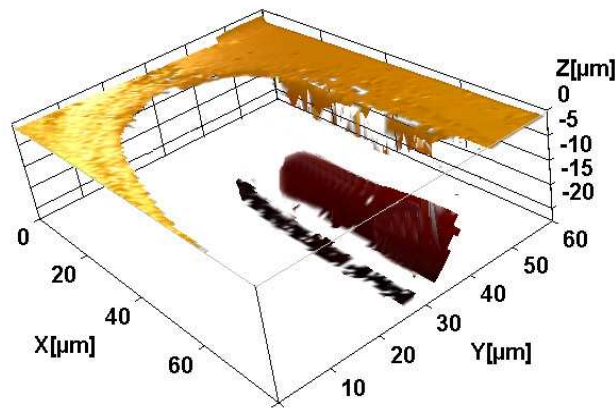
Figure 6.2: Poor measurement exploited by an optical profilometer on a microchannel: more than 40% of the surface results to be unsampled. .

The problem is slightly different for scanning probe microscopy. SPMs in fact normally never generate surface topographies presenting void pixels. This is because a physical position is constantly recognized for the tip, and this is associated to an actual point in the sample surface. Then the problem with SPMs is not the presence of unsampled regions, but is rather associated with the presence of points which are not descriptive of the surface. This happens for instance each time the tip flanks come into contact with the surface and the surface is not scanned by the tip apex. An example is given in Figure 6.3a, were chessboard-like array of square pillars is visibly distorted by tip convolution (indicated by arrows). In this case an appropriate operation would be elimination of parts scanned through tip flank. This is easily achievable, by a simple segmentation of surface topography: measuring local slope and thresholding all the pixels overcoming a certain slope, it is possible to achieve a corrected surface topography, as the one reported in Figure 6.3c, were regions touched by the tip flanks have been substituted by void pixels.
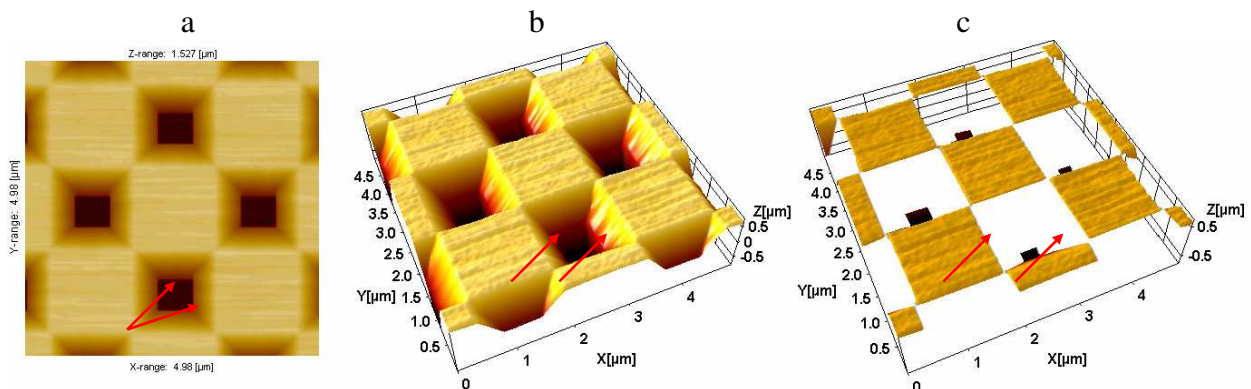

Figure 6.3: Chessboard-like array of square pillars: holes are not well defined since sidewalls are dilated by tip flanks (a and b). A threshold can substitute improperly sampled parts with void pixels (c). Arrows indicate thresholded portions.

Presence of void pixels, or anyhow improperly sampled regions within the measurement file, is of course undesirable. Some methods for remedying to this problem are applied, based on off-line image processing. Following this easy approach, surface topography on the voids is assigned through interpolation between valid pixels surrounding the same voids. This approach is not taken here, as the author believes that this biases measurement results with respect to the true values. Contrary to this, the new method uses actual data, to build up a complete description of the sample surface, measured with two or more positionings of the sample itself.

In the following the two alternatives will be discussed, referring to the surface shown in Figure 6.4. This was generated artificially via software, simulating a typical laser ablated cavity. The volume of the groove was set to $18 \cdot 10^3$ µm³, with a surface micro-roughness of Sq=0.21 µm.

In order to imitate the result of an arbitrary virtual measurement on the groove itself, points having a local slope higher than 30 degs were set as void.
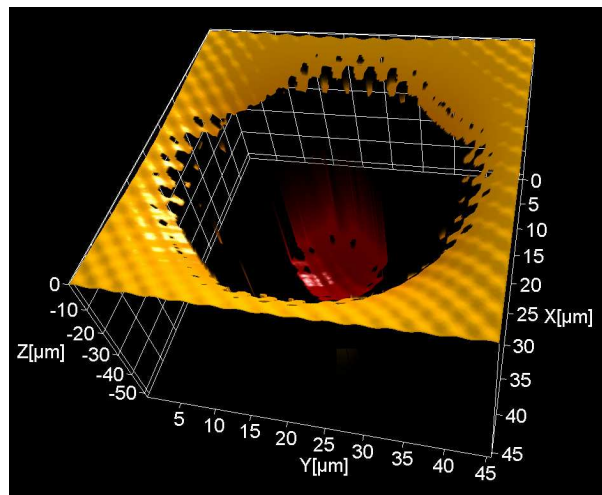

Figure 6.4: Software generated surface, simulating a typical laser grooving operation; points having a local slope higher than 30degs are set as void.

6.2.2.1 Interpolation

The problem of interpolation is by some means correlated to the filtering operations discussed in Paragraph 3.3.11. Interpolation is a mathematical calculation carried out on the surface data set, by fitting a continuous function through the discrete input samples. This operation eventually allows for evaluation of new values at arbitrary positions. Generally interpolation reduces the bandwidth of a signal by low-pass filtering the discrete signal itself. The signal lost during the sampling process is eventually reconstructed by smoothing the data samples with an interpolation function. A number of interpolation kernels have been introduced: linear, median, quadratic, cubic, B-spline, Lagrange, Gaussian, nearest neighbor, fractal, etc. each developed and suitable for some specific applications [117] [118].

By way of example, the described surface was processed through three different interpolation functions: median, linear and cubic.
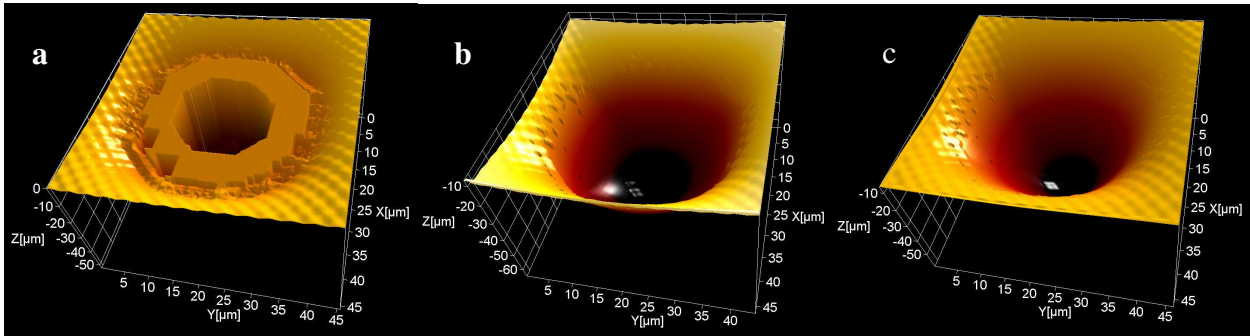

Figure 6.5: Surface topography after interpolation reconstruction, through median (a), linear (b) and cubic (c) function.

Measurements on reconstructed surface were carried out in terms of both groove volume and Root Mean Square roughness. In order to return comparable values, the original surface and the three achieved interpolated images were analyzed in the same way. The same cut-off was applied for roughness evaluation, which filtered out the overall shape of the cavity. Results are reported in Table 6.2. Relative deviations from 22% up to 67% are reported in the case of the volume estimation; similarly deviations ranging from 71% up to 114% were recognized for the roughness evaluation.

Table 6.2: Volume and roughness results on the original and on the interpolated topographies.

	Simulated groove	Median Interpolation	Linear Interpolation	Cubic Interpolation
Groove Volume [µm³]	$18 \cdot 10^3$	$6 \cdot 10^3$	$13 \cdot 10^3$	$14 \cdot 10^3$
Surface Roughness Sq [µm]	0.21	0.45	0.06	0.07

These results shouldn't surprise too much. Although such large deviations could be reduced through a deeper analysis and definition of some wiser interpolation function developed on purpose, still a great uncertainty would persist. This is mainly due to the fact that the content of information of the surface used for the tests is very poor, since almost 47% of the total area was covered by void pixels (Figure 6.4). Furthermore the interpolation method is not adding "true points" to the data set, but is just guessing how the topography could be shaped.

Clearly interpolation is not a recommendable operation and in general from a metrological point of view is not acceptable, in particular when wide areas have not been or have been improperly probed by the instrument.

6.2.2.2 Tilting

The tilting solution here described, is at the base of the new developed method.

When a sample is tilted, all the points of the surface increment their local slope of a fixed quantity, equal to the imposed tilting. As a result, new void pixel zones are generated, while actual points are sampled in the areas previously void. This behavior is described in Figure 6.6, where effects of: 0, 15, 30, 45 and 60 degs tilts have been simulated on the image shown above in Figure 6.4.
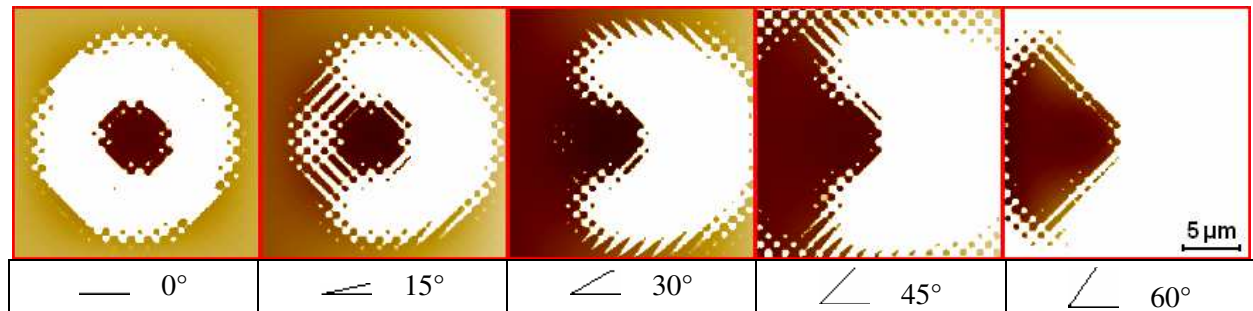

Figure 6.6: Simulation of surface topography detection as revealed with a sample tilted by different angles; the color equalization is linear with topography. Darker regions are deeper, lighter lies above while void pixels are white.

Information pieces retrieved from differently tilted measurement simulations can be considered in some way complementary. This expedient was used as a starting point for the development of a method for improving instrument performance, with regard to the tip accessibility or maximum detectable slope limitations.

6.2.3 Maximum detectable slope enhancement

The developed method is based on the use of a 3D scanning instrument, a closed-loop single axis tilt stage [119] and software routine, coded on purpose, within a commercially available image processing package [35]. No modifications are whatsoever introduced or needed into the instrument hardware.

6.2.3.1 Working principle

The measurement procedure is the following. Two or more 3D profiles are recorded, with the sample tilted at controlled angles, each single image containing diversely distributed unsampled portions. All the images are then aligned on a virtual reference plane by a software routine developed on purpose.

Two differently tilted images shall represent some common surface region. Under such circumstances, the two images can be matched, and a new image generated, which contains valid topography from the two images matched, and less invalid-void pixels.

Recursive application of this procedure provides enhanced surface topography imaging. It is intended, how the method is best suited for instruments which are fast in delivering a single scan, which is only one of the n steps to get the final image. Atomic Force Microscopes generally have long scanning times: for this reason reconstructions based on three or more steps have generally to be considered inconvenient in terms of total measuring time.

The principle is shown below (Figure 6.7), by processing the same computer-generated topography seen before, simulating an optical measurement on the laser grooved surface.
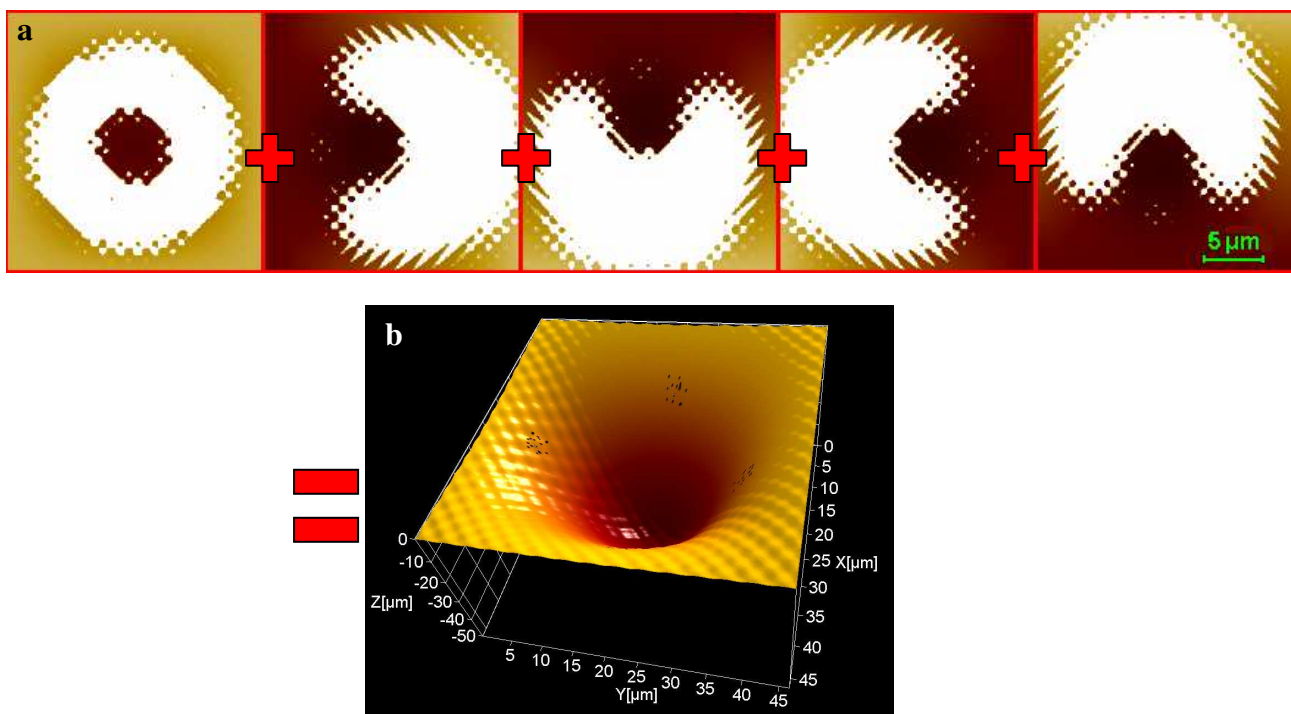

Figure 6.7: a) Simulation of surface topography detection as revealed with a sample tilted by 0 degs, +15 degs and -15 degs about the x,y- coordinate axis. b) The result of the application of the image processing routine, allowing for a reduction of void pixel down to 0.1%.

Figure 6.7a shows five surface topographies, with many void pixels (those with local slope higher than 30 degs, having simulated simulating γ=30 degs).

3D Profiles were simulated, with either 0 degs or 15 degs tilt angles about x,y- coordinate axes. With reference to Figure 6.7a from left to right, the sample is tilted of respectively: 0 degs, -15 degs about y, -15 degs about x, +15 degs about y, +15 degs about x.

Application of the image processing routine, to the five images of Figure 6.7a, returns the image shown in Figure 6.7b. The latter features a remarkably lower content of voids. Surface roughness

RSQ and groove volume, compared with reference values, showed deviations within respectively 0.1% and 0.07%.

6.2.3.2 The software

The software routine, developed for matching and stitching multiple 3D profiles can be schemed through the following flowchart (Figure 6.8).
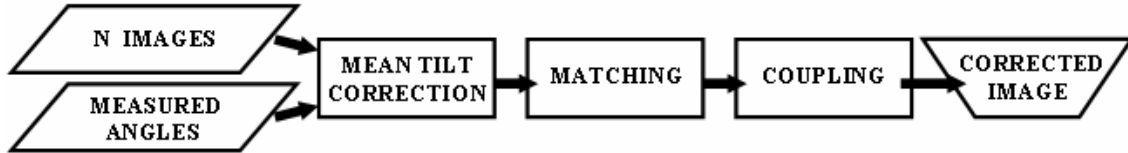

Figure 6.8: The developed procedure.

The n images are aligned on a common virtual reference plane: this operation is achieved through rotation of the surfaces about the tilt axis. It is stressed that a metrological rotation is performed, not a planar fitting which would otherwise cause cosine error. The exact rotation amount is known, (with 10^{-3} deg accuracy) through the servo-controlled rotating device.

In order to reduce uncertainty on the tilt angle, given as an input to the automatic routine, it is very important to pay the maximum attention to the alignment of the tilting axis with the microscope axes coordinate system. The maximum accuracy is in fact achieved when the tilting axis is perpendicular to the microscope vertical axis and is parallel to one of the two horizontal axes.

We assume that, even when wide surface portions are covered by void pixels, nevertheless some regions, with valid measurement points can be found, common to two or more images. These consistent profiles portions, in the following, will be referred to as overlapping areas. They are processed in order to detect the best matching relative position. Least square method is applied at this level (6.1):

$$\sigma(x, y) = \sqrt{\sum_{i,j \neq void} \frac{\left(I_1(i, j) - I_2(i, j)\right)^2}{n}} \tag{6.1}$$

where I_1 and I_2 refer to respectively the points of the first and of the second image in the overlapping area. i,j are the coordinates of the points on the overlapping areas; n is the number of pixels used in the computation. Best matching relative position is eventually found by minimizing a least square function [48] [120].

In the following step, scans are stitched in a single data file. This has been addressed in the flowchart as "coupling operation".

Since different images have void areas located in different positions, during the coupling operation complementary contributes allow for a significant reduction of void pixels in the final data set.

6.2.4 Experimental investigation and results

In order to complete the investigation, the new approach was applied to characterization of real profiles, obtained with actual measurements.

Two different tests were carried out. The first was done on a Vickers hardness microindentation, on a steel surface, characterized through a 3D optical profiler; the second one was on a 1-D array of rectangular SiO_2 steps on a Si wafer, measured through an AFM.

6.2.4.1 Reconstruction of a Vickers indentation

Vickers microindentations are generally done for hardness evaluation. A square-based diamond pyramid is smoothly loaded, without impact, and held in place for 10 or 15 seconds. An indentation of approximate depth 30µm was produced on a steel surface.

The microindentation was measured by means of an interference microscope (Fogale Nanotech PhotoMap 3D [121]), equipped with a 50× Mirau type interference objective (see Appendix A).

Sample tilt was performed with a closed-loop single axis rotation stage: PI M-037 DG Rotation stage driven by linear DC motor and controlled through a Mercury C 862.00 controller (see Appendix A).

With an indentation angle α of approximately 136degs, local slopes in the range 20-30degs were achieved. Three measurements were performed by means of the Interference microscope, with three tilt angles: 0degs +10degs and -16degs. Measurement results, along with final result, after processing of the data sets through the developed software, are reported in Figure 6.9.
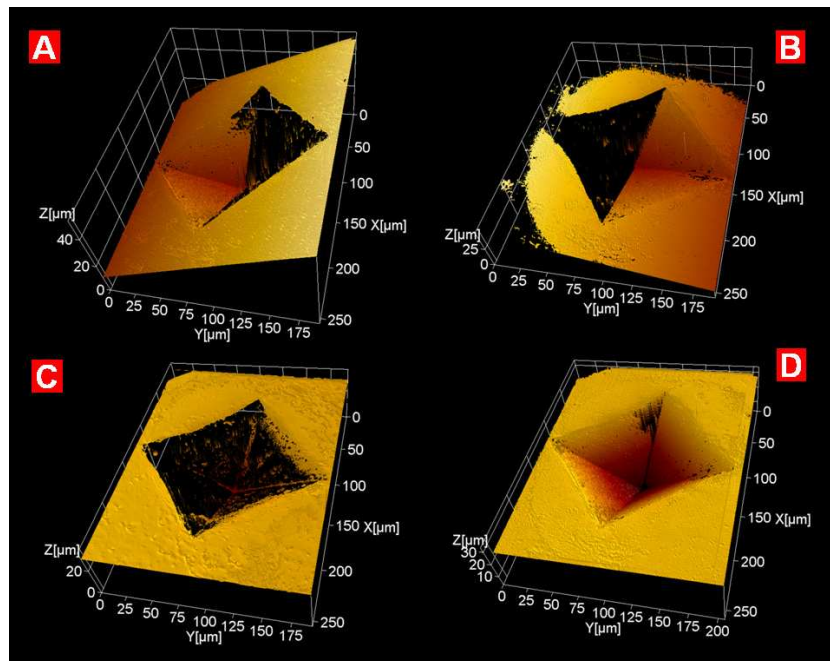
Figure 6.9: 3D topographies of the indented surface. a) -16 degs installation slope. b) 10 degs installation slope. c) Profile of the indentation with no tilt. d) Indentation reconstructed matching and stitching a) and b).

It is seen how the quality of the profile, obtained without any tilt of the sample (Figure 6.9c) is very poor. Inside the indentation almost 90% of the surface has not been sampled and many void pixels are present. Figure 6.9d reports the result of the image processing routine described above, achieved by coupling only two scans (Figure 6.9a and Figure 6.9b). The quality of this topography is definitely higher; in fact the number of void pixel has been reduced down to 6%. This percentage could be reduced in principle even further, by using a third profile, taken with another tilt angle and combined with the image shown in Figure 6.9d.

6.2.4.2 Reconstruction of a silicon grating

Linewidth measurements are performed in semiconductor manufacturing, data storage industry and micro-mechanical engineering. Continuous development has brought the critical dimension of semiconductors devices below 100 nm. This trend places an ever tighter tolerance on the variability of the manufacturing processes and increases demands upon the accuracy of lines measurements.

A method for evaluation and reconstruction of lines sidewall has been already described in Section 5.3.2: the applicative test of the present paragraph is instead focused on sidewall reconstruction and linewidth measurement. A similar analysis was also proposed in [122].

The silicon line pattern was a 1-D array of rectangular SiO_2 steps on a Si wafer, with a nominal 500 nm step height and 3.0 µm pitch [61]. It was measured by means of an open loop atomic force microscope, DME Dualscope 95-200 (see Appendix A).

Two measurements were performed by means of the AFM, with two tilt angles: -19 degs and +21 degs. Measurement results, along with final result, after processing of the data sets through the implemented automatic routine, are reported in Figure 6.10.
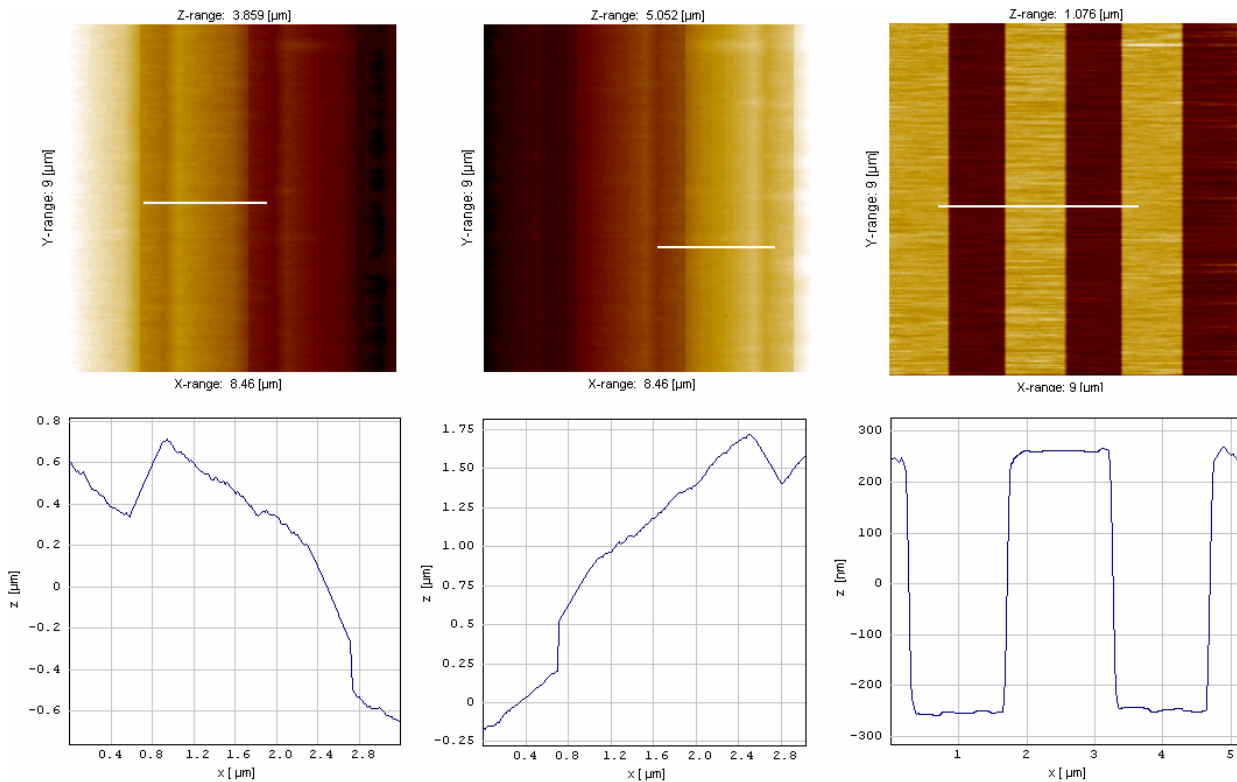

Figure 6.10: Surface topographies and profiles of the silicon line pattern. a) +21 degs installation slope. b) -19 degs installation slope. c) Indentation reconstructed matching and stitching a) and b).

The quality of the final reconstructed image can be appreciated by comparing geometry parameters with values coming from standard measurements performed with the same AFM on the same sample (Figure 6.11). The mean value for groove width in the reconstructed topography was 1.602 µm (Figure 6.10c), with an improvement ranging from 10% to 40% if compared with other results coming from a single standard scan. Similarly, an average sidewall angle of 87.2° was found, with an increase bigger than 20% (Figure 6.10 and Figure 6.11).
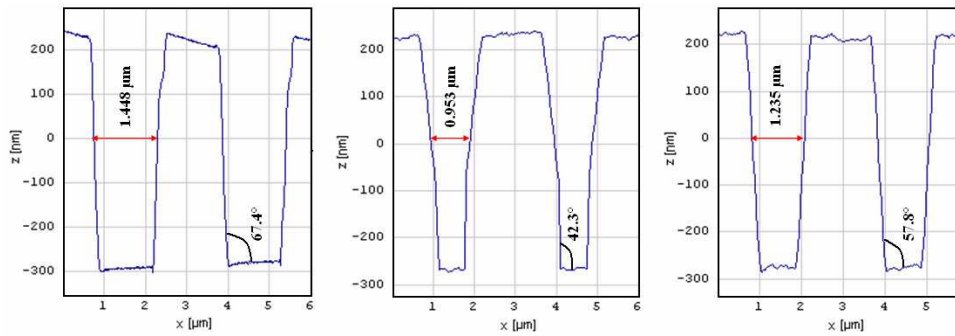
Figure 6.11: Lines pattern measurements performed with the same AFM on the same sample, with a single standard measurement. Differences are due to differently worn tips.

This apparent line shrinking is easily explicable. When the scan is performed on the tilted sample one of the two opposite sidewalls is much accessible to the tip, and convolution effect is strongly reduced. The reduced convolution effects in a reduced sidewall dilation: therefore the apparent line shrinking is due to a reduced distortion of the final topography (Figure 6.12).
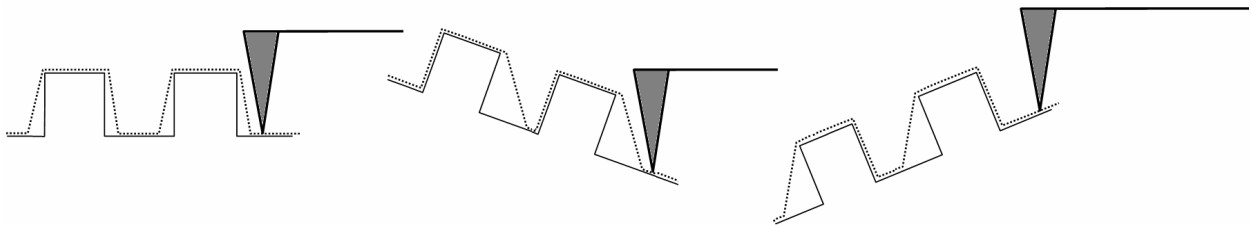

Figure 6.12: The installation slope allows the tip to reach one of the sidewalls, with no interference of the flanks on the measurement.

6.3 Stitching

In the previous chapter, matching and coupling operations were used to reconstruct images where bad sampling had occurred. The same principle can be applied in order to enlarge the maximum instrument scan range. In fact AFMs have scanning ranges limited up to about one hundred micrometers, which is often not sufficient in the context of micro-technology, where dimensions in the order of hundreds of micrometers are often to be measured with nanometric resolution. Large range AFMs have been developed through implementation of laser interferometers for controlled probe displacement [123] [124]: but complexity and costs related with this architecture rend it hardly applicable in the industrial field. An alternative solution is then Surface Mapping, a measurement strategy consisting in repositioning of the stage after each measurement [125] [126], whereby topography data files are merged into a single large-range high-resolution image. The resulting range depends on the number of images stitched together, as tiles in a mosaic.

Moreover, a relevant advantage of Surface Mapping is seen in connection with instruments based on lateral scanning devices. Any set-up based on scanning a probe in a raster fashion, as the large majority of topography measuring instruments, is inherently slow. Tracking velocity is limited by inertial constraints and the imaging process is sequential. Imaging slowness results in large thermal drift affection of the measured topography [127]. This can be overcome by merging a few short scans rather than performing a single long one.

Limitations of the strategy are related to time consumption resulting from the many interruptions for sensor relocation, and processing large data files, in addition inaccuracies of the probing sensor combine with those from the positioning systems. Merits and limitations of surface mapping are summarized in Table 6.3.

Table 6.3: Surface Mapping merits and limitations.

Advantages	Limitations
• Large measurement range with no compromise as to resolution • Reduction of drift	• Time consumption • Generation of large data files

A software solution for surface topography stitching was developed and implemented, based on maximization of a cross-correlation function. Detailed descriptions were given in previous publications ([48] [120] [128] [129]), therefore here only main developments, results and applications are reported.

6.3.1 Stitching procedure

With the algorithm here presented, it is possible to achieve a complete compensation of the offsets occurring during repositioning.

The stitching principle here presented is based on the adoption of an overlapping area between two consecutive scans to be merged into a single data file. Best matching relative position of the two images is found within the overlapping region.

Matching allows compensating the positioning errors from the stage. Measurements are eventually performed on a data file resulting from a mosaic of single AFM scans. The sequence of operations is described in Figure 6.13.
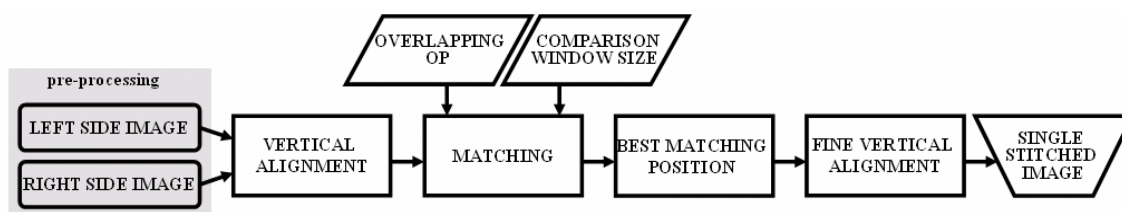

Figure 6.13: Stitching procedure.

Some parameters are not constant:

• overlapping percentage OP;

• comparison windows size.

The amount of overlap needed depends on the accuracy of the positioning device, which for a stepper motors driven table is of few micrometers. However, overlap does not affect the resulting image as stitching position is based on matching rather than on the input displacements.

Nominal overlap between two images is indicated by the index OP:

$$OP[\%] = \frac{\Delta x}{L_x} \cdot 100 \qquad (6.2)$$

where L_x is the range imaged within the left side scan and Δx is the nominal overlap in the direction of the axis that is displaced during the measurement.

Topography in the overlapping region results from probing the same physical surface portion. The approximate amount of overlap, input by the user as an OP index is used by the vertical alignment procedure within the code. This is shown in Figure 6.13: after the pre-processing operation for the compensation of possible tilts (due for example to pitch or roll stage movements), the stitching software proceeds with the vertical alignment. The vertical offset is corrected by adding the average offset to the left side image, computed within the overlapping region, to the topography values of the whole right side image. Once the images are globally leveled, matching is calculated, and then a fine vertical alignment is performed. The latter is based only on z coordinates within local windows defining the best matching position, and stitching is eventually performed. These windows will be described in the following, when a detailed discussion of the matching operation is made: as a result a single image of the half sphere is obtained. Stitching of data sets aligned along the y axis is also possible, by calling a subroutine performing similar calculations.

In Figure 6.14 two images are sketched, taken on neighbor regions. There, surface features are illustrated by geometrical elements: circles, triangles, and squares. The overlapping area is gray colored. In an ideal case no positional errors occur during sensor displacement.
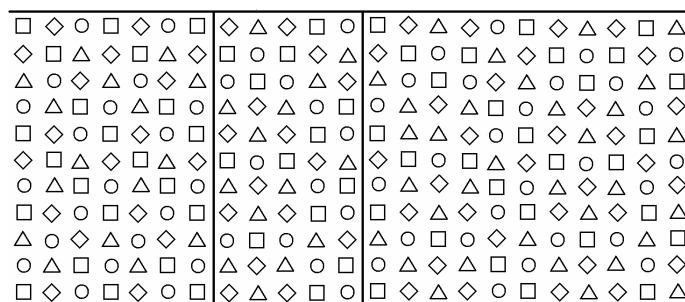

Figure 6.14: Overlapping area between two neighbor regions.

When translational or rotational errors resulting from displacement are considered, as shown in Figure 6.15, the common probed area gets smaller. As long as inaccuracies in the positioning do not compromise the presence of some surface portions common to the two images, correct stitching is still possible.
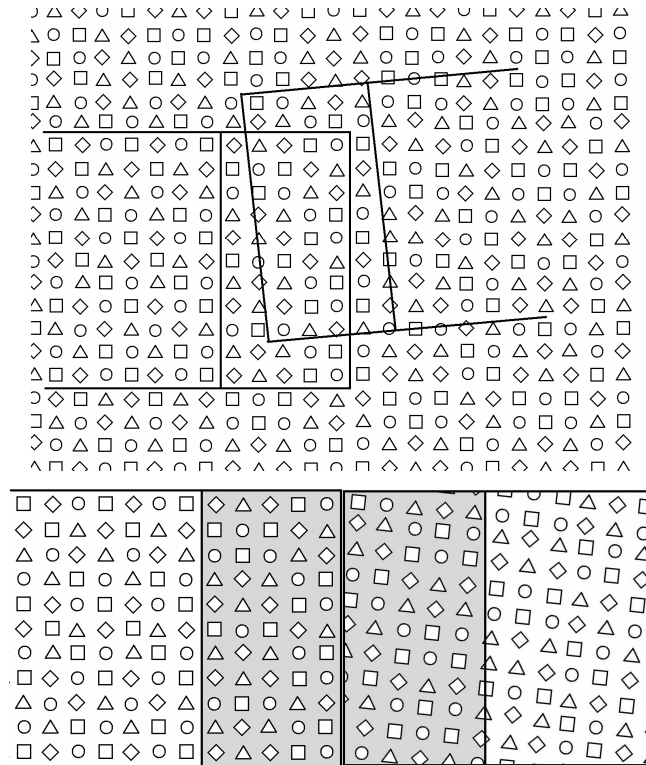

Figure 6.15: Top: the probed surface region common to the two scans is reduced as consequence of positioning errors. Bottom: Features contained in the two data files. The gray colored regions are those defined by the OP index.

If no errors had occurred during sensor positioning, the two gray areas would have had the same features on them. Since the two images result from erroneous probe displacement, they do not contain the same information.

Matching is based on the definition of two comparison windows within the overlap [130] [131]. The last parameter, which is relevant for calculation of stitching position, is the size of the comparison windows. These windows are four rectangular pixels arrays. Two are defined on the left side image, in the overlapping region; the other two are on the right side image and move during matching calculation. Windows dimensions are defined as fractions of the overlapping region dimensions. The matching procedure is sketched in Figure 6.16, where the comparison windows are gray colored. Two arrays with the same dimensions are taken on the right-side image, at the top left corner of the comparison area. Two matching indexes are calculated between compared regions, then, as described in the same figure by the red arrows, the

rectangles are shifted along the area defined by the OP index and new matching goodness coefficients are calculated.
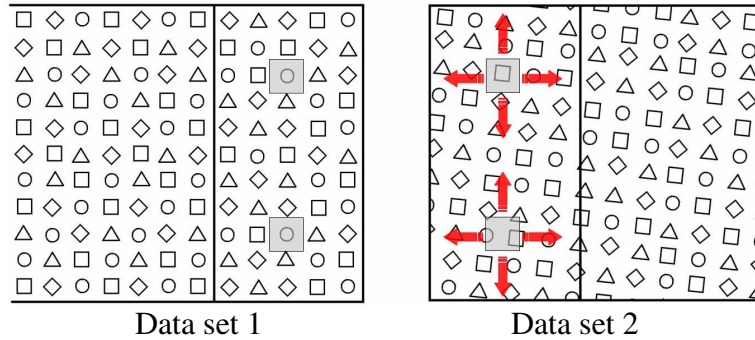

Figure 6.16: Data set 1 with the shaded rectangles indicating the current comparison regions. Data set 2 shows the corresponding comparison region in its initial position, while arrows indicate lateral shift for detection of the best matching position.

The matching procedure implemented in the stitching software was based on the cross correlation function [132]. Assuming that the comparison areas consist of $m \times n$ pixels, with nominally equidistant values because of the instrument raster scan operation, each pixel contains the information about the local surface height, z_{ij}, the cross correlation coefficient c is given by:

$$c = \frac{\sum_{i=1}^{m}\sum_{j=1}^{n}(z_{ij}^{I} - \overline{z^{I}}) \cdot (z_{ij}^{II} - \overline{z^{II}})}{\sqrt{\left[\sum_{i=1}^{m}\sum_{j=1}^{n}(z_{ij}^{I} - \overline{z^{I}})^{2}\right] \cdot \left[\sum_{i=1}^{m}\sum_{j=1}^{n}(z_{ij}^{II} - \overline{z^{II}})^{2}\right]}} \qquad (6.3)$$

$0 \le c \le 1$

The coefficient c accepts values ranging from 0, for no correlation, up to 1 for full correlation. The superscripts I and II in (2) refer to the left and the right side images respectively. $\overline{z^{I}}$ and $\overline{z^{II}}$ are respectively the average height values calculated in the two compared areas.

Maxima of c are used for determination of the matching position depending on which subroutine is called for the calculation.

The result of the two comparisons is a couple of vectors, each describing local relative shifts. Each vector is calculated as the distance between the initial centered position of the correspondent comparison window and the relative best matching position. By analyzing these two vectors it is possible to define the total rototranslational movement occurred during probe displacement. Final stitching of the two images can then be performed (Figure 6.17).
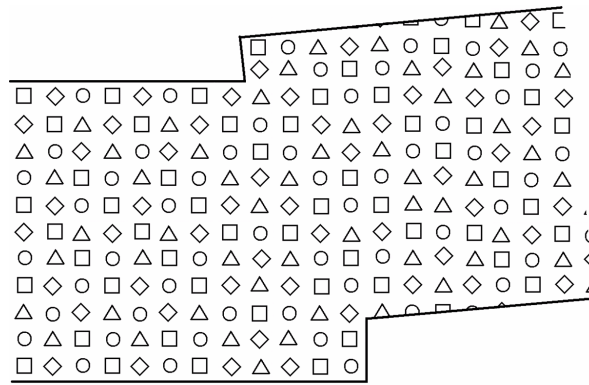
Figure 6.17: Final stitching result.

6.3.2 Stitching software performance verification

The automatic routine was implemented into commercially available software for surface topographies analysis [35] [133]. A set of experiments was done in order to evaluate efficiency of the matching algorithm and of the subsequent stitching.

6.3.2.1 Matching algorithm

Investigations on the matching algorithm were performed by applying the developed software tool to surface topographies couples, reproducing a finely controlled rototranslational motion. This was eventually compared with the automatic routine output. In the figure below, main results regarding evaluated translation and rotation vectors are presented (Figure 6.18).
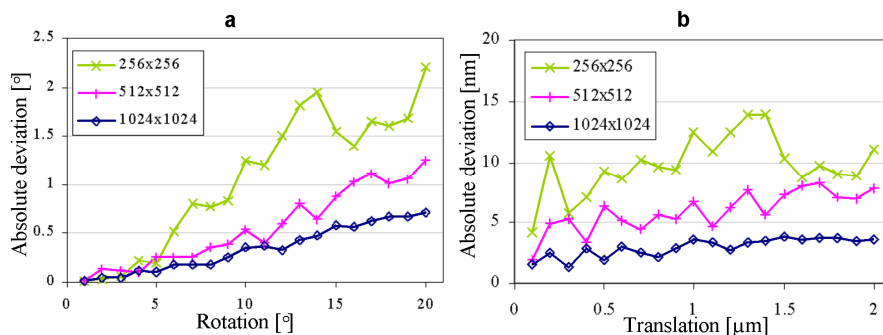
Figure 6.18: Absolute deviation between actual and evaluated rotation (a) and translation (b) [130].

The automatic routine results are here summarized.

1) The developed method is based on an approximated algorithm: comparison areas are horizontally and vertically shifted in order to find local motions. In case of big rotations, rotational shifts should be taken into account: therefore the method is much incorrect as well as bigger rotations have occurred (Figure 6.18a). This can be considered quite a minor problem, since stages can normally ensure an angle control with an accuracy smaller than 1°.

2) Routine output is influenced by surface topographies resolutions: in fact higher deviations were detected whenever lower resolution topographies were analyzed (Figure 6.18a and Figure

6.18b). This problem can be overcome by considering a resolution software increase: in this way sub pixel accuracy can be achieved.

3) The developed method is not considering and evaluating possible deformations occurring after probe displacement, due for instance to scanner artifacts (see Chapter 3). These can lead to staggered results, and therefore should be compensated or corrected before proceeding with the matching routine.

6.3.2.2 Stitching result

Stitching performance verification was in particular focused on results after compensation of translational errors, in the horizontal x-y plane and in the vertical z direction, which usually constitute the biggest source of error when the sensor is repositioned relatively to the surface.

Single and multiple stitching operation performance have been already profusely described in [48]. Therefore here only analysis on sub-pixel stitching is described.

The interest on sub-pixel algorithms is related with the possibility of increasing the accuracy of the stitching process. The strategy for the detection of the best matching position was the same already described. A modification was introduced by increasing the resolution within the comparison areas. This is achieved through a resampling operation: locally, third degree polynomial interpolating curves are calculated, in order to generate new points. Afterwards the matching routine is normally applied to the new high resolution comparison areas. Best matching and stitching are eventually given, with an accuracy of the final results that depends on the resolution increase set by the user.

Tests were performed to analyze results produced by the improved method. Investigations were carried on couples of surface topographies, reproducing 40×40 bumps spread with a quadratic grid distribution [48]. The overlap percentage was set to 2.5% (one period in the overlapping area). Starting resolution was always 512×512 pixels, while in the comparison area a resolution increase was applied: 2×, 4×, 8× and 16×.
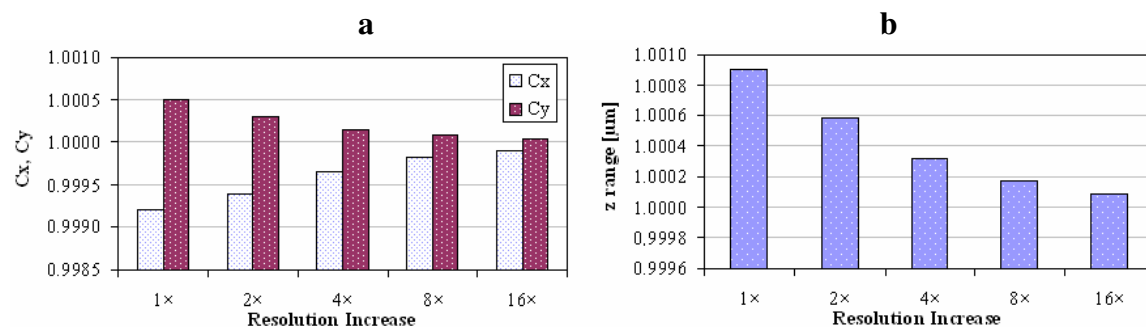

Figure 6.19: Performance of the stitching software with sub-pixel accuracy, after resolution increase: (a) x axis and y axis scaling factors and (b) average step height after stitching.

As reported in Figure 6.19a, the calibration coefficients Cx and Cy exhibit a clear improvement (values equal to one have in fact to be considered representative of a perfect stitching). Increasing the resolution, calibration coefficients proportionally show an improvement in the stitching operation, and a similar behavior was found with regard to the height of the resulting stitched topography (Figure 6.19b).

On the other hand, negative effects were also recognized. The main disadvantage was detected with the time needed by the automatic routine to perform the stitching, which grows with the square of the resolution increase. This means that if a 16× improvement is wished, computational time rises up to 256 times, and tens of minutes may be needed to complete the stitching.

6.3.3 Application to three dimensional surface topography characterization

The investigation was completed with application of the software to stitching of real surfaces. Two samples were selected for evaluation:

- a calibration sample, consisting of chromium patterned glass substrate.

- a roughness standard type D1 as defined by ISO 5436-1 [65].

The patterned glass sample is an artifact designed for optical instrument calibration, presenting several geometrical features. The area chosen for the test was 460×250 µm^2 wide, containing three circles with different diameter, 50 µm, 100 µm and 200 µm respectively. Results were compared with those obtained through stitching images without any matching calculation. The latter procedure, which relies on positioning stage accuracy, was used before development of the stitching software [60].

Eight areas were probed with a large range Atomic Force Microscope based on an AFM scanner mounted on the z axis of a Coordinate Measuring Machine (CMM) (see Appendix A).

The measurement strategy is shown in Figure 6.20: numbers indicate scan sequence.

In order to build up the mosaic, the AFM sensor was repositioned after each single scan. Upon displacing the CMM table, positioning errors occur. A region of the optical calibration artifact was imaged performing surface mapping, respectively with and without stitching software. When using the stitching software, single image scan range was set at 128 µm × 128 µm, with an overlap OP=6%.

Surface mapping was also performed with no overlap, with a scan range of 120 µm × 120 µm. The mosaic image was built by simply merging single data sets. Each AFM data set, regardless the surface mapping procedure, was corrected from thermal drift, by single profiles leveling. First order polynomial fitting was then applied, to correct any accidental tilt of the surface.
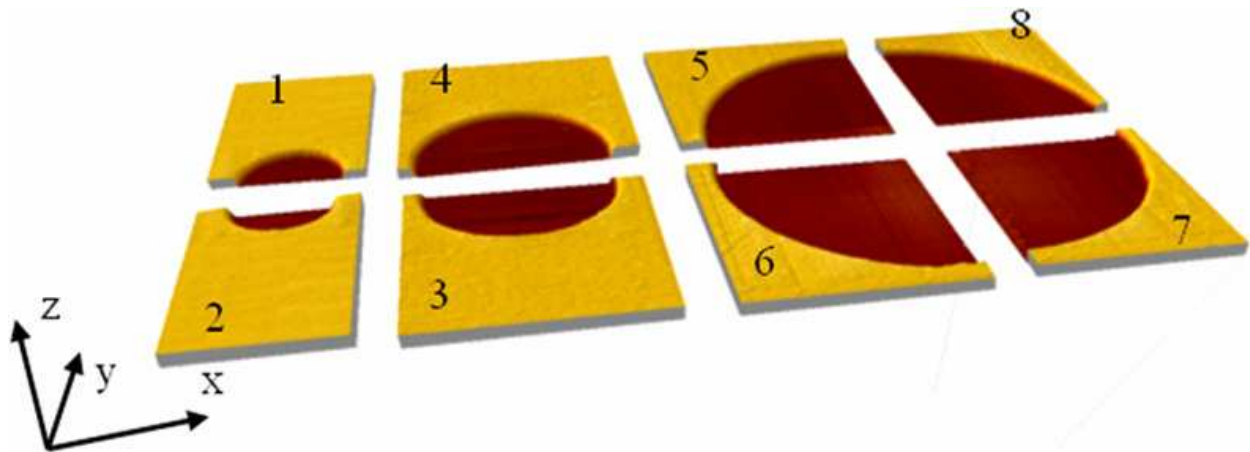
Figure 6.20: Imaging strategy.

Images resulting from surface mapping are shown in Figure 6.21 while the image stitched with the software is shown in Figure 6.21b, and the image stitched without matching calculation is shown in Figure 6.21a. Chromatic scaling is linear with vertical elevation: lower regions are dark, while top terraces are bright. The first image does not show relevant discontinuities in correspondence of the borders. In the second image some misalignments can be clearly discerned, due mainly to the positioning errors occurred during CMM table displacement.
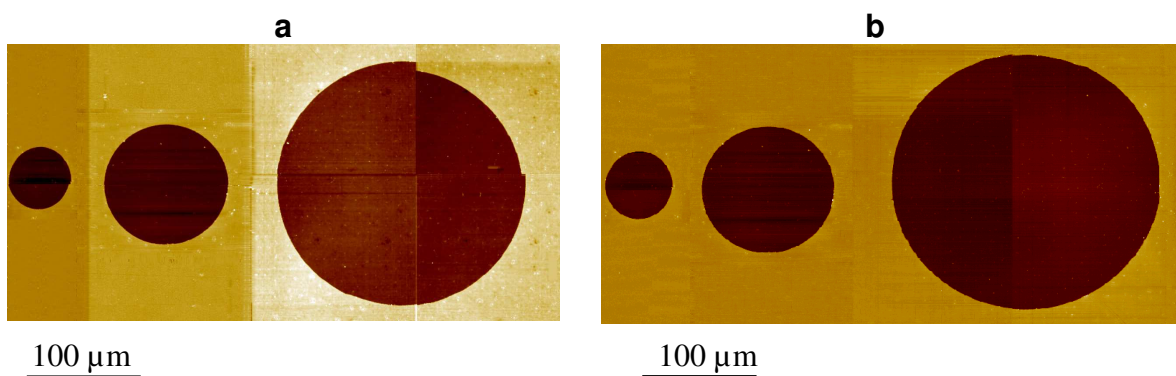
Figure 6.21: Surface mapping of the calibration artifact resulting from simple merging (a) and from stitching software application (b).

With reference to Figure 6.21a, the four parts composing the big circle are vertically offset. This error is mainly due to single scans topography influence on vertical leveling: it occurs when data sets are merged without any software correction. The scans, from which the big circle was obtained, were in fact taken without any vertical repositioning of the sensor. The mean height of the four images differs by about 10 nm, as shown in Figure 6.22, which is not discernible by the instrument through the surface approaching procedure. Single scans arithmetic mean values are represented with dotted lines in Figure 6.22. Upon stitching such images, dramatic vertical discontinuities appear at the borders (Figure 6.22). The stitching software provides compensation

of the above described boundary discontinuities. These are eliminated through vertical alignment, based only on topography of border regions, as described before.
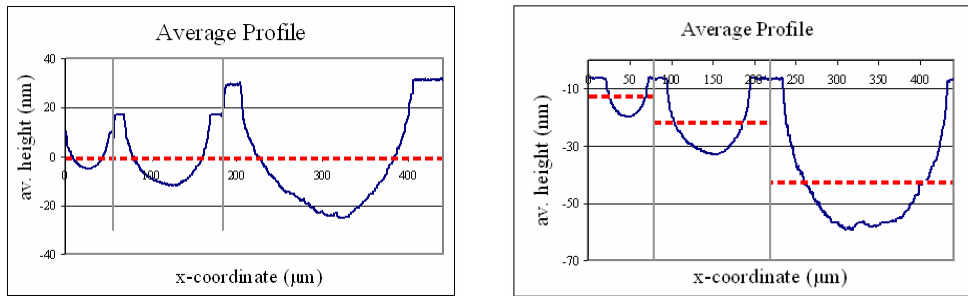
Figure 6.22: Average profiles: for a given x value, the average height is the mean z coordinate in the y direction.

The second sample analyzed was a type D1 roughness standard (Figure 6.23), with nominal roughness amplitude parameters [65] [134] [135]:

- Ra=0.209µm;
- Rz=1.505µm.
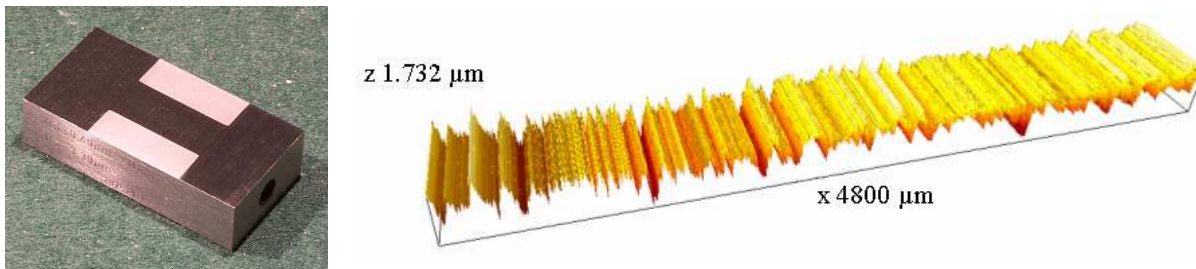
Figure 6.23: The type D1 roughness standard and the performed surface mapping.

An area of $4800 \times 32 \mu m^2$ was measured by means of two instruments:

- a stylus profilometer, provided with a with a 2µm radius tip (see Appendix A);
- a large range AFM (see Appendix A).

Measuring conditions are summarized in Table 6.4.

Table 6.4: Measurement conditions.

Instrument Properties	Stylus Profilometer	Large Range AFM
Scan range [µm × µm]	2410 × 32	128 × 32
Number of Scans	2	40
Total Scanned Range [µm × µm]	4800 × 32	
Stitching Software Applied	Yes	

Analyses regarded both single profiles and whole surfaces. Figure 6.24a shows results of stitching operation applied respectively to stylus profilometer and to atomic force microscope measurements.

Figure 6.24: Results from the investigation on the roughness standard: a) measured profiles; b) calculated parameters. Error bars refer to expanded uncertainty for the certificate and to standard deviation of the measurements for the 2 instruments [136].

Even with such a huge number of stitching operations (31 in the case of AFM scans), very good agreement was found between measurements performed with the two instruments. Further confirmation of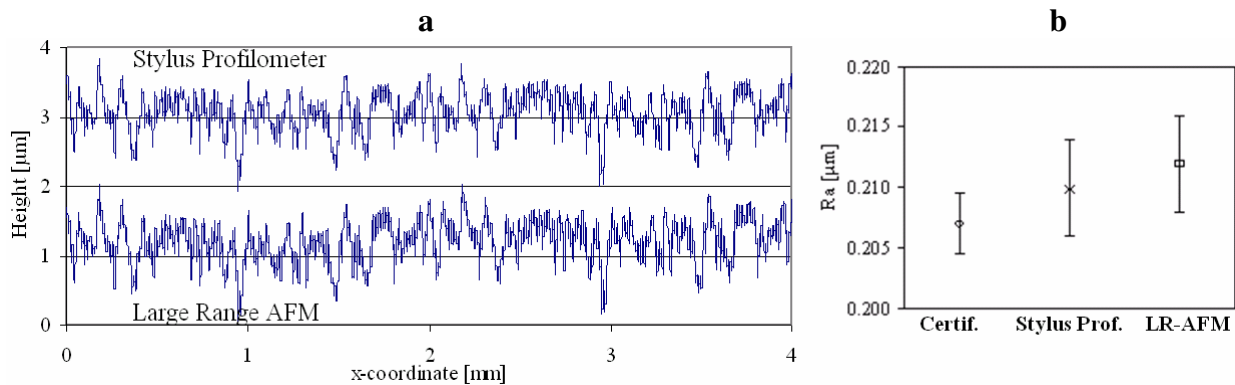 agreement was proved by cross-correlation (equation 2) larger than 90%, calculated between the two entire surfaces. No misalignments or discontinuities were detected at the borders: the implemented routine fully compensated positioning error occurred during stage displacements.

Estimated average roughness parameter (Ra) from AFM and stylus instruments were in full agreement with the nominal ones. Mean deviations <1.5% and maximum deviation <2% were calculated (Figure 6.24b).

A clear tendency was evidenced in the case of AFM: larger and deeper valleys were generally sensed, causing a light increase in average roughness Ra evaluation. This phenomenon was attributed not only to the stitching process, but also to the presence of a tip definitively sharper for the atomic force microscope with respect to the stylus profilometer (whose radius of curvature is ~100 times bigger).

6.4 Feature oriented scanning

AFM scanner systems build up images sequentially, by scanning in a raster fashion over the surface [53]. This traditional approach, common to the large majority of topography measuring instruments, is inherently slow. Imaging slowness results in large thermal drift affection of the measured topography. Furthermore, due to physical effects and dynamic interactions, tip

undergoes continuous deterioration, caused by wear effects [108]. Tracking speed is limited by inertial constraints as well as feedback loop bandwidth. Upon approximating the AFM probe as an harmonic oscillator, the bandwidth of the resonant peak is inversely proportional to the so called Q factor of the sensor, according to (6.4):

$$\tau_{resp} = \frac{Q}{f_0} \qquad\qquad\qquad (6.4)$$

Where: τ_{resp} is the inverse of the bandwidth and f_0 is the cantilever resonance frequency. Numerous efforts have been done, in order to solve, overcome or compensate these limitations. Solutions to decrease imaging time maintaining quality have included use of cantilevers with high resonance frequency, optimization of Q-factor and high performance feedback, and Frequency modulation [37]. All of these approaches still produce surface topographies through standard raster-pattern scanning. Instrument settings are adapted to the measurand only in terms of range, resolution, scan rate and a few other parameters. This approach can be considered as a "blind" control model, satisfactory whenever distributed analyses are needed: this is the case of roughness measurement, or lattice constant evaluation on repetitive samples. However this blind control is inefficient for other measurement tasks; often the sample reproduces highly oriented textures, spotted or localized distributions, string-like appearance, sculptured shapes or well defined geometries. This is the case of deposits, crystals, biological samples, micro-machined or micro-formed components, microfluidic parts, MEMS, etc. For these samples, the raster-pattern control represents a time-consuming approach, badly characterizing the features of interest and moreover providing uninteresting data about marginal portions of the sample comprised within the scanned area.

A novel feature-oriented approach was then developed, for collecting data from a region of interest following a predefined path. This method is designed to optimize efficiency and effectiveness of the measuring operation by driving the probe over the sample surface along free-form paths, and collecting only relevant information.

6.4.1 A new measuring approach

A new measurement approach was developed and tested for atomic force microscopy, but in principle applicable to the whole family of scanning probe microscopes. According to this method, the probe is driven over the sample surface along free-form paths, in order to scan with high resolution only discrete features of interest and collecting data only on relevant positions of the sample to be analyzed. Furthermore data coming from the on-going scan operation can be used as a feed-back for a real-time control of the measurement. The aim of this new approach is

to optimize the instrument use, in terms of measuring time and length, instrument full performance exploitation and content of information of gathered data. This is achieved through an intelligent tip motion, made possible by re-programming of the control system. By means of a software interface with the instrument control, more advanced and complex paths than the simple raster scan are possible. This kind of control is not new: studies and applications have been reported for nanolithography purpose.
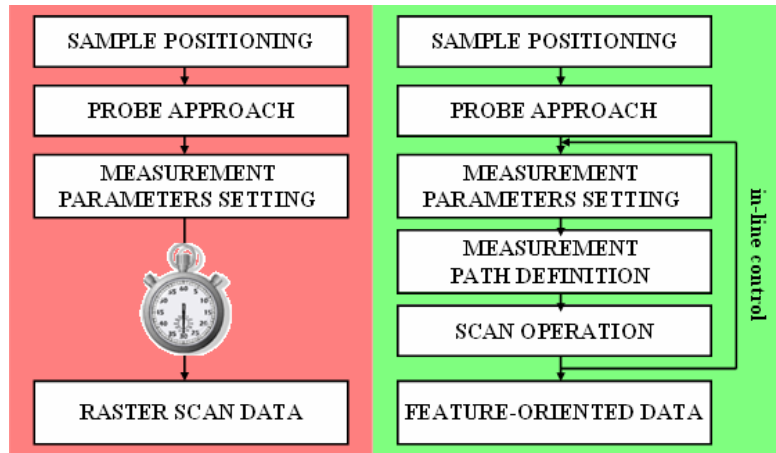

Figure 6.25: Feature-oriented and raster scan operations.

Figure 6.25 reports a comparison between the traditional raster scan and the feature-oriented method. The new feature oriented method is not introducing a radical change in the instrument set up: it only redefines the measure strategy. At its basis stands a very simple concept: measuring only what is needed. A very simple example can be usefully considered to explain the new method: a "J" shaped micro-feature (Figure 6.26). A proper micro-geometry characterization needs accurate evaluation of width, length and height of the two perpendicular segments. AFM raster scan can be of choice for the purpose. In order to improve the quality of the measurement, a high number of profiles has to be set. Despite the length of the measure, the evaluation of the geometry dimensions is very accurate in x and z direction but very poor in y direction. In fact, due to the parallelism between the lines and the edges, top and bottom bounds (red-circled in Figure 6.26a) were not properly characterized. The feature-oriented approach is proposed in Figure 6.26b: after two perpendicular lines, traced to localize the feature, the scan operation is performed in the two perpendicular directions, with equidistant lines. In this way the same accuracy is ensured along both x and y axis, a resolution no worse than the raster scan is achieved and time needed for the whole measurement is at least one or two orders of magnitude lower.

The J shaped micro-feature is only an example of measurement optimization. In general great benefits can be achieved whenever the interest of the measure is not spread on a whole

rectangular area, but is localized on isolated portions. In such cases it is profitable to follow the feature or the geometry and carry the measurement on only where scanned data can bring a real benefit to the geometry characterization.
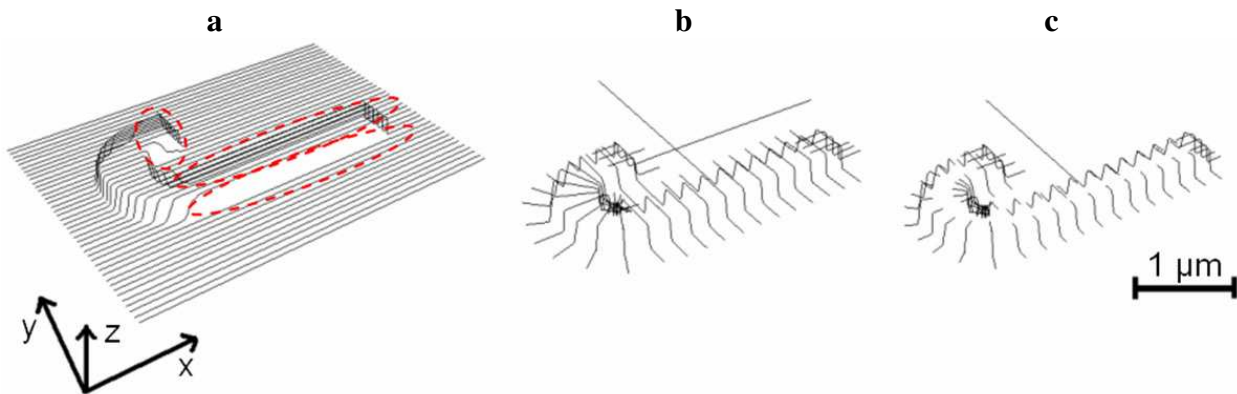

Figure 6.26: J-shaped micro-feature: a) raster scan (red circles localize under-sampled zones); b) and c) two examples of feature-oriented method.

An extremization of this concept is represented in Figure 6.26c: once the localization line meets the feature, recognized through a sudden change of height, the instrument follows the feature boundary. Similarly to the feature localization method, the corner positions can be recognized through topography properties (such as the height) changes, and used as an input in a feedback control for modifying the scan direction.

6.4.2 Performance verification

For the present study a commercially available Nanosurf Easy Scan 2 AFM was applied [137].

This is an instrument based on voice coil actuators, providing fairly linear probe drive (see appendix A). Measurements were carried out in dynamic force mode (vibrating the probe over the sample surface at approximately its resonance frequency). A script-interface to program the instrument control was available, allowing advanced scanning modes. It is worth to note that scanning systems are designed to produce raster paths, and effects of non-raster scan on measurement aren't reported in literature. For this reason the AFM was put through a number of tests, to characterize the behavior of the actuation system under stressing conditions.

6.4.2.1 Background noise

Noise was evaluated by taking a measurement over a polished silicon flat surface.

For the raster pattern method, a measurement was performed over a 200 x 200 nm area. In order to simulate the free positioning, noise associated with the feature-oriented method was evaluated as follows: 200 nm long profiles with a random orientation on the horizontal plane were

randomly localized and scanned on a 10 x 10 µm region. Topographies were subsequently analyzed with commercially available software [35]. Root mean square roughness (Rq) was eventually evaluated for the two cases. The raster scan produced an Rq of 0.572 nm, not much different from the 0.577 nm value obtained with the feature-oriented simulation. This difference, lesser than 1%, can be considered uninfluent for the new method application.

6.4.2.2 Positioning repeatability

The proposed method relies on a precise steering of the probe on the surface. In order to achieve an accurate characterization of the surface topography, it's important that the positioning error is as low as possible. In fact this constitutes a major source of uncertainty for the measurement operation.

In piezo tube based atomic force microscopes, positioning error can be mainly related to hysteresis and creep phenomena. Those effects produce a non-linear behavior of the scanning system, causing a discrepancy between the intended and the actual position of the scanned points. Apart from the non-linearity sources described above, an additional positioning error source is given by thermal drift. This is not compensated by the instrument metrology frame, and results in a non controllable tip-sample relative positioning error. The entity of thermal drift depends mainly on the mechanical construction of the microscope, the shorter the mechanical tip-sample loop, the lighter this problem. Usually any AFM has to be "warmed up" for some time until thermal drift appears to be negligible in comparison with the scanning speed.

Repositioning error was evaluated on a reference chessboard like grid, as depicted in Figure 6.27.
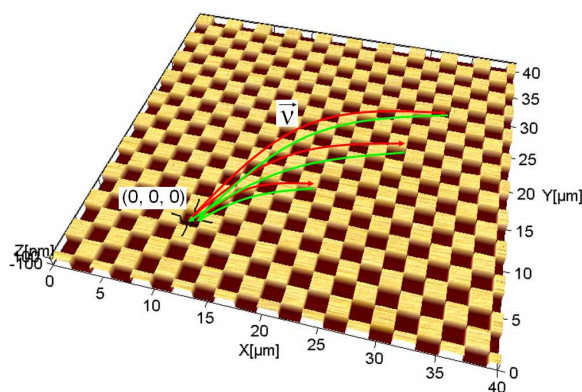

Figure 6.27: Evaluation of repositioning error.

The following operations were repeated for error evaluation:

- a reference square hole was chosen as (0, 0, 0) position, and two perpendicular profiles were taken including the reference position;

- a certain displacement was given to the probe through the actuation system, as defined by (6.5):

$$\vec{v}(\vec{x}, \vec{y}), |x| = |y| \land 0 \le x, y \le 30 \mu m \tag{6.5}$$

- the probe was brought back to the (0, 0, 0) position: some residual misalignment (Δx, Δy, Δz) was present;

- the misalignment (Δx, Δy, Δz), which constitute the positioning error, was evaluated for different values of v, by means of the same software routine presented in Section 5.4.

Evaluated misalignments are descriptive of positioning repeatability; nevertheless a contribution due to thermal drift is also present in the reported results.
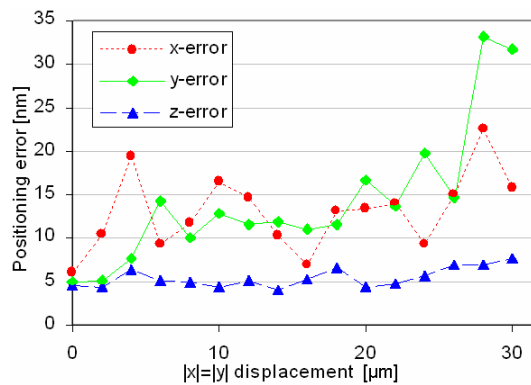

Figure 6.28: Positioning error.

The instrument was kept in standard operating condition. Of course a better insulation system could have reduced the detected errors. Mean values are reported in Figure 6.28. An average positioning error lesser than 15 nm was detected both for x and y direction and lesser than 6 nm was evaluated for the vertical direction. This is quite acceptable if compared with a standard measurement: for a 20×20 µm measurement, sampled through 512×512 pixels, the resolution, equivalent to the pixel size is about 20nm. As a consequence the detected error is lesser than the pixels size. As a general statement, the positioning error can be considered negligible or at least acceptable for measurements bigger than 1×1 µm.

6.4.2.3 Thermal drift

Thermal drift is a time dependent phenomenon, therefore influences measurement in particular when high resolution imaging is achieved by taking many profiles. Differently from hysteresis and creep, this problem affects also closed loop scanners, whereas tip position is controlled with respect to a reference frame, while the sample one is affected by time-depending deformations.

An analysis was performed with the purpose of evaluating the influence of drift on measurements. A single 1 µm profile was continuously and regularly measured over a long lapse of time (more than 8 hours). Drift was measured by evaluating misalignments occurring on subsequent profiles. Measurements were repeated in order to calculate drift contribute on x, y

and z directions: drift velocities < 0.15 nm/min were evaluated (Figure 6.29). For a thirty minutes scan, which can be considered as a slow time in scanning probe microscopy, the total deformation amounts to approximately 7 nm. Considerations similar to the ones discussed in the previous paragraph can be done. This deviation can be considered acceptable for any measurement in a range bigger than 0.5×0.5 µm. The possibility of performing feature-oriented measurements, ensures scan times up to one or two orders of magnitude lesser, allowing for a remarkable reduction of drift influence on measurement.
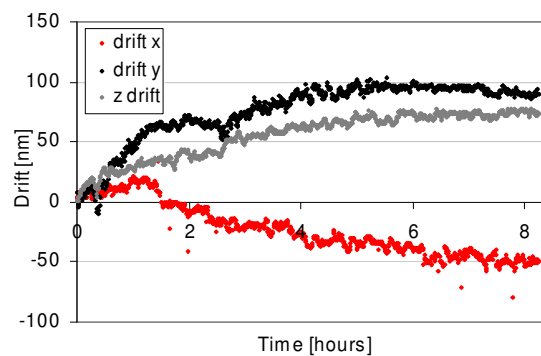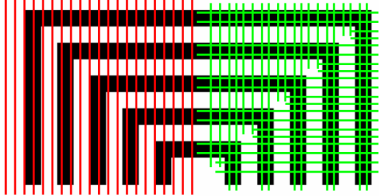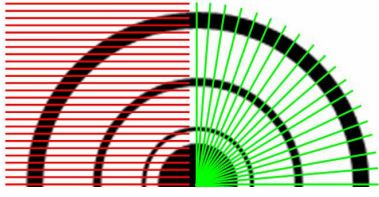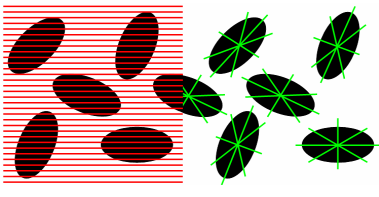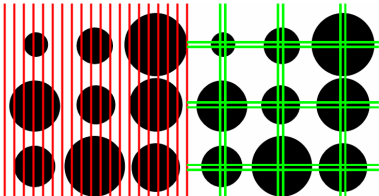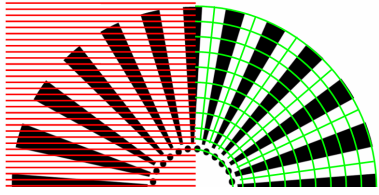
Figure 6.29: AFM drift on the three axes.

6.4.3 Test geometries

A grid reproducing different geometries was applied, in order to verify the feature-oriented method performance. This standard is made by a chrome layer on a quartz substrate [138]. Five of the geometries were used within the tests: concentric squares and circles, elliptical and spot arrays and an asterisk-like structure. These are reproduced in Table 6.5, together with a representation of the scan paths: red resembles raster, while green resembles the feature oriented method. The same table reports also the evaluation of one or more geometry dimensions, and the number of relevant points, i.e. the number of intersections between the scanned profiles and the features boundaries.

Table 6.5: Application of the feature oriented method to different test geometries. Dark areas on the figures indicate the opaque chrome layer. Red and green lines represent a sketch of the raster and of the feature-oriented scan paths [139].

Raster scan mode	Test Geometry	Feature oriented mode

Total scan length: 4.4 mm
Total scan time: 28 minutes
Relevant points: 266
Measurement of x pitch:
  4.98 µm (σ = 0.17 µm)
Measurement of y pitch:
  4.95 µm (σ = 0.06 µm)
		Total scan length: 3.8 mm
		Total scan time: 23 min
		Relevant points: 220
		Measur. of x pitch:
		  4.96 µm (σ = 0.07 µm)
		Measur. of y pitch:
		  4.97 µm (σ = 0.06 µm)

Total scan length: 2.6 mm
Total scan time: 9 minutes
Relevant points: 108
Measur. smallest circle rad.:
  6.48 µm (σ = 0.32 µm)
Measur. largest circle rad.:
  25.05 µm (σ = 0.14 µm)
		Total scan length: 1.6 mm
		Total scan time: 6 minutes
		Relevant points: 144
		Measur. smallest circle rad.:
		  6.15 µm (σ= 0.11 µm)
		Measur. largest circle rad.:
		  25.12 µm (σ = 0.10 µm)

Total scan length: 5.1 mm
Total scan time: 34 minutes
Relevant points: 392
Measur. of aspect ratio:
  1.98 (σ = 0.02)
		Total scan length: 1.3 mm
		Total scan time: 18 minutes
		Relevant points: 360
		Aspect ratio:
		  2.00 (σ = 0.02)

Total scan length: 3.7 mm
Total scan time: 24 minutes
Relevant points: 364
Measur. of x pitch:
  9.90 µm (σ = 0.08 µm)
Measur. of y pitch:
  9.92 µm (σ = 0.05 µm)
		Total scan length: 2.3 mm
		Total scan time: 15 minutes
		Relevant points: 216
		Measur. of x pitch:
		  9.92 µm (σ = 0.06 µm)
		Measur. of y pitch:
		  9.91 µm (σ = 0.06 µm)

Total scan length: 1.3 mm
Total scan time: 8 minutes
Relevant points: 212
Measur. of angle:
  5.1deg (σ = 0.3deg)
		Total scan length: 0.5 mm
		Total scan time: 5 minutes
		Relevant points: 154
		Measur. of angle:
		  5.0deg (σ = 0.1deg)

The concentric squares include 6 squares, with sides comprised between 10 µm and 60 µm and 5 µm lines width. The raster scan characterization is very effective for the description of the lines extending along x direction, but poorly reproduces the other features, which are parallel to scan direction. This has an effect on pitch measurement: standard deviation evaluated for y-oriented lines (x-pitch) is almost the triple than the x-oriented one (y-pitch). The problem is avoided

through a feature-oriented approach, which keeps scan direction always perpendicular to the features.

The second test geometry consists of concentric circles. The benefits brought by the feature oriented method are remarkable: scan time is reduced and the number of relevant points is increased by more than 20%. This is achieved by avoiding measurements on irrelevant regions (as the area external to the largest circle), and keeping the scan direction always perpendicular to the lines direction. Evidently the sampling also results to be more homogeneous, with relevant points equally distributed on larger as well as on smaller circles.

Figure 6.30 shows how the same topography is reproduced by Cartesian and Polar coordinates. In Polar coordinates the diameter of the smaller circle is measured by the width of the central line.
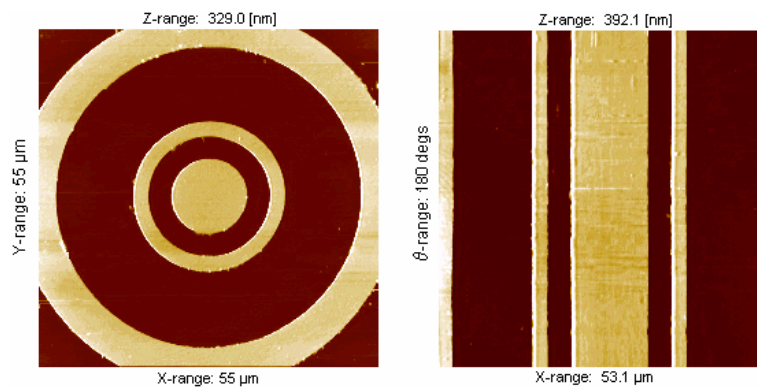
Figure 6.30: Concentric circles, represented in Cartesian (left) and in Polar (right) coordinates.

The array of elliptical features consists of rotated ellipses, with a nominal aspect ratio of 2. With raster scanning characterization, a high resolution (which corresponds to a high number of profiles) is needed in order to provide a proper sampling in the bottom and upper parts of the ellipses. Evaluation of aspect ratio and rotation is easily achieved through a radial scanning, consisting of 5 degrees shifted profiles. Moreover the feature-oriented scanning provides a scan time reduction of almost 50% and a homogeneous distribution of the "relevant points", with no problems of over- and under-sampled areas. In the figure below (Figure 6.31) Cartesian and Polar coordinates are given for one of the measured ellipses. The eccentricity of the ellipse can be found comparing the largest (i.e. the major axis) and the thinnest (i.e. the minor axis) polar profile. The relative rotation is simply found through detection of the largest profile on the Polar angle axis.
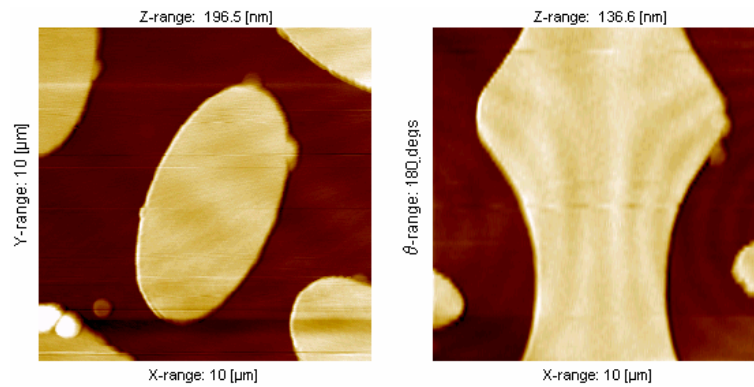
Figure 6.31: Concentric circles, represented in Cartesian (left) and in Polar (right) coordinates.

The circles array reproduces equidistant spots of different size. Raster scan well localizes features in y direction, but is in general less efficient for localization along x direction. Good results are achieved through a grid sampling, as shown in Table 6.5, allowing for a reduction of scan time up to 35%.

The asterisk-like geometry is very representative. Raster scan provides a sampling distribution that is not efficient; in fact, most of the relevant points are involved in the characterization of the upper slices, while only a few relevant points are localized in the lower slices (the amount is six times lower). This bad characterization is reflected by the high standard deviation on angles evaluation. In the feature-oriented method the circular scanning distribute equidistant relevant points on the slices. Thus geometrical dimensions can be evaluated with the same accuracy on all the parts of the test structure. A sequence of radial profiles has also been taken; this is helpful for evaluation of surface roughness.

6.4.4 Investigation on a microfluidic system

A microfluidic like system was produced, for investigating the new feature oriented approach.

This was produced through Micro-Electrical Discharge Machining (µEDM), an accurate process enabling manufacturing of complex geometries. In EDM, material removal is due to a rapid series of repetitive electrical discharges: this is also at the origin of the typical craterized topography. In the figure below (Figure 6.32a and Figure 6.32b) a SEM measurement and a 3D reconstruction of the sample are reported.

In microfluidic systems, interest is generally focused on grooves width and roughness. For this sample an intelligent approach would be then the one depicted in Figure 6.32c, where red lines are meant for the evaluation of the groove width, while the light blue lines are indicative of grooves roughness measurements.
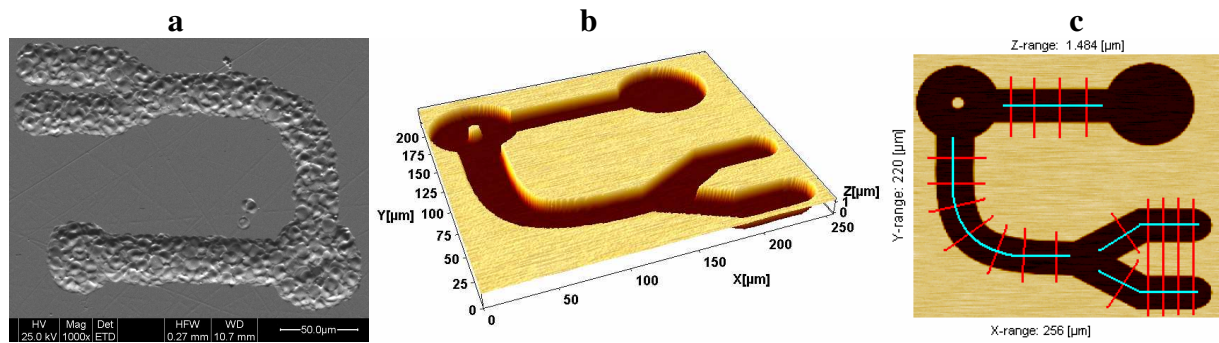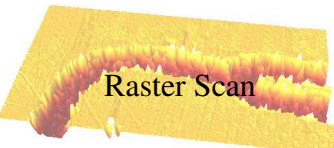
Figure 6.32: SEM measurement (a) and a 3D model (b) of the sample used for investigations. In (c) an example of optimized feature oriented approach

Measurements were also carried on with the traditional raster scanning approach. Negligible differences were appreciated in terms of topographical characterization, but definitely higher was the waste of time (Table 6.6).

Table 6.6: Raster scan and feature oriented measurements on the microfluidic like system.

	Width [nm]	σ [nm]	Ra [nm]	σ [nm]	Total scan time [s]
Feature Oriented Scan	23.78	0.50	162	44	32'
Raster Scan	24.02	0.55	155	37	84'

6.5   Conclusions

The merits of Scanning Probe Microscopes make them the best choice for many applications. However, some limitations are present, however, mainly related to finite tip dimensions, limited instrument scan range and inherent raster scan slowness.

This chapter presents original approaches to overcome the above instrumental limitations.

A method for characterization of high aspect ratio structures with steep sidewalls is described, based on cross-correlation matching operations and subsequent coupling. The implemented software tool processes images taken with controlled tilt and returns a high quality 3D profile of the sample being investigated.

Experimental evidence is provided with reference to two cases: a Vickers indentation on steel, measured with an optical profilometer, and a silicon line pattern, measured with a commercial Atomic Force Microscope. Reduction of void pixels percentage from 90% to 6% was recorded by the authors, as a result of application of this method.

A coupling operation based on cross-correlation matching is also used for enlarging measured scan range. An automatic routine implemented into commercial software provides compensation of positioning errors, occurring when performing surface mapping, for instance through a motorized table.

Routine performance was tested by using software gauges: sub-pixel level inaccuracies, with absolute deviations <0.2%, were detected for single stitching operation. Moreover, the method was applied to measurement of two real surfaces, with two different topography measuring instruments. Qualitative analysis on a patterned glass demonstrates almost complete compensation of misalignments and discontinuities. Results obtained from the application of the stitching routine in the case of a roughness standard measurement are in full agreement with certificate values.

A new measurement approach for Scanning Probe Microscopy is finally presented, where the probe is driven over the sample surface along free-form paths, in order to scan with high resolution only discrete features of interest and collect only relevant data. The proposed method was applied and tested with the characterization of complex micro-structures. Results are discussed compared to traditional raster scanning measurements. It is demonstrated how the new approach optimizes measurement, allowing for considerable scan time reduction (up to 50%, or more). Benefits are presented also in terms of more effective sampling strategies.

6.6.1 Contributions

Chapter 7

Conclusions

7.1 Summary

The following summarizes the main results of the Ph.D. They are grouped into five points, according to the topics of the five main chapters (Chapter 2 - Chapter 6).

The thesis addresses Atomic Force Microscopy (AFM), an important measuring technique, belonging to the family of Scanning Probe Microscopy (SPM). AFMs are instruments primarily designed for the characterization of surface topographies with a very high spatial resolution. In the first part SPMs are globally reviewed. The description focuses on AFM, probably the most relevant quantitative measuring technique for the nanoscale. Working principles are rapidly described and a classification is proposed of the different industrial fields benefiting from AFM applications.

Typical AFM sources of error are described, mainly arising from the scanning system, the probe, the environment and from data processing subsequent to measurement. Scaling and crosstalk, creep and hysteresis, noise, drift, tip convolution and software are some of the discussed error sources. When possible, distortions are described through a mathematical model: all contributions are eventually unified in a single reference model, which in principle completely describes AFM scanning. This model, quite complex, was designed to define a reference framework, able to give a mathematical *collocation* to the different distortions occurring. Possible compensations for some of the distortions described are discussed in the subsequent chapters.

The following section is devoted to AFM calibration issue.
A new concept of calibration standards is presented, based on optical fiber technology. It is shown how fibers, used as micro-cylinders, can be applied for performance verification of a

number of instruments for topographical characterization in the microscale. In particular the possibility of accurately calibrating horizontal and vertical AFM axes is described: results are seen to substantially agree with values coming from traditional techniques. The merit of the new procedure for vertical calibration is the possibility of calibrating the instrument with continuity over the full vertical range. The same task in common practice would require a number of measurements on different step heights of a fixed height. Lastly, the chapter discusses orthogonality, presenting a software tool developed for estimation and correction of crosstalk errors.

The work continues with a section discussing the possibility of compensating drift distortions and predicting tip wear effects.

In the vertical direction, reconstruction of three-dimensional surface topographies affected by vertical drift is proposed, based on two images, taken with mutually orthogonal scanning directions. The method provides a reduction of profile misalignments and a general improvement of the measurement results compared to reference values: evidence of improvements is provided through investigation carried out on optical flat (with a reduction of mean square roughness from Sq=3.83 nm down to Sq=0.18 nm against the reference Sq=0.14 nm) and cylindrical fiber surfaces (radii deviations from a maximum of 22.33% down to 0.29% were proved). In the lateral direction, compensation is provided through an alignment of profiles in the slow scan direction. Optimal results were reported in the case of repetitive patterns in the slow scan direction.

A method for modeling distortions due to tip wear rate in contact mode AFM is eventually proposed. Evolution of tip was observed by reverse imaging of a scanned nanostructured topography, periodically repeated throughout tip lifetime. Lateral force was mapped conjunctly with removed material rate and tip radius reduction and was applied for calibration purposes.

The last part addresses possible solutions to three typical AFM problems: difficult tip access to steep slopes, limited measurable range and long scanning times.

In order to reduce the effect of the interaction of the probe with the sample, and thus help the reconstruction of high aspect ratio structures, a double tilt technique has been proposed. Here reconstruction is based on matching and coupling of two surface topographies, scanned with different installation slopes. Reduction of void pixels from 90% to 6 % was reported in the case of a Vickers microindentation, measured with a White Light Interferometer.

A matching automatic routine was also implemented for stitching three-dimensional topography data sets taken on contiguous areas, allowing for surface mosaicking operations. The developed

routine fully compensates positioning errors occurring when the measuring instrument is displaced relatively to the surface. Sub-pixel level inaccuracies, with absolute deviations <0.2%, were detected for single stitching operation.

The issue of time reduction is discussed in the last section, where a new measurement approach is investigated for overcoming raster scan limitations. With the new method, the probe is driven over the sample surface along free-form paths, scanning with high resolution only discrete features of interest, collecting only relevant data and allowing for consistent scan time reduction (up to 50% and more).

7.2   Further work

Suggestions for further activities dealing with Atomic Force Microscopy are listed below:

- Tip shape and tip wear characterization are perhaps one of the crucial aspects still not completely resolved in Scanning Probe Microscopy. A large campaign would be necessary in order to better model tip wear phenomena in contact, non contact and intermittent AFM scan modes. A systematic analysis would consider a number of influencing parameters: not only scanned length, but also speed, force, gain, amplitude, materials, etc.

- Integration with other instruments is seen as a strategic improvement. Atomic Force Microscopy can't provide all the metrological answers: therefore a better integration with other sensing technique would improve the quality of results.

- The trend for future of Scanning Probe Microscopy is toward development of new scanning and new probes architectures. Effect of free scan patterns and complex multi-probes implementation should be better investigated, in order to better understand the loss of accuracy due to non-standard measurement set-ups.

References

Chapter 1 – Introduction

[1]   Feynman R.P., There's plenty of room at the bottom, Engineering and Science, Vol. 23, pp 22-36, 1960.

[2]   www.nanotech-now.com/nanotechnology-art-gallery.htm , www.itg.uiuc.edu/exhibits , www.veeco.com/library and others (accessed on December 2006).

[3]   Roco M.C., International Strategy for Nanotechnology Research and Development. Senior Advisor for Nanotechnology, National Science Foundation.

[4]   Carneiro K., Position paper on The need for measurement and testing in nanotechnology, Report to the EC High Level Expert Group on Measurement and Testing, Fifth European Framework Programme for Research and Development, 2002.

[5]   Leach R., Cui Z., Flack D., Microsystems Technology Standardisation Roadmap, Standardisation for Microsystems Technology: The Way Forward, Report prepared under EU MEMSTAND, 2001.

[6]   Instrumentation and Metrology for Nanotechnology, National Nanotechnology Initiative Workshop, Gaithersburg, 2004.

[7]   Moritab S., Yamada H., Ando T., Japan AFM roadmap 2006, Nanotechnology, Vol. 18/8, pp 1-10, 2007.

[8]   The National Nanotechnology Initiative – Research and development leading to a revolution in Technology and Industry- Supplement to the president's FY 2007 budget, 2006.

[9]   Binnig G., Rohrer H., Scanning Tunneling Microscopy – from birth to adolescence, Nobel lecture, December 8, 1986.

[10]   Binnig G., Rohrer H., Gerber C., Weibel E., 7×7 Reconstruction on Si(111) Resolved in Real Space , Phys. Rev. Lett., Vol. 50, pp 120-123, 1983

[11]   Binnig G., Quate C.F., Geber C., Atomic Force Microscope, Phys. Rev. Letters, Vol. 56/9, pp 930-933, 1986.

[12]   Martin Y., Williams C.C., Wickramasinghe H.K., Atomic Force Microscope-Force Mapping and Profiling on a sub 100-Å scale, J. of Appl. Phys., Vol. 61/9, pp 4723, 1987.

Chapter 2 – Scanning Probe Microscopy

[13]   Bariani P., Marinello F., Savio E., De Chiffre L., Caratterizzazione geometrica di microcomponenti, Atti del IV congresso Metrologia e qualità, Torino, pp 169-177, 2005.

[14]   Stevens G.C., Baird P.J., Nano- and Meso-measurement Methods in the Study of Dielectrics, IEEE Trans. on Dielectrics and Electrical Insulation, Vol. 12/5, pp 979-992, 2005.

[15]   Lonardo P.M., Lucca D., De Chiffre L., Emerging Trends in Surface Metrology, Keynote paper, Annals of the CIRP, Vol. 51/2, pp 701-723, 2002.

[16]   Howland R., Benatar L., A practical guide to Scanning Probe Microscopy, Park Scientific Instruments, Sunnyvale, 1996.

[17]   Vorburger T.V., Dagata J.A., Wilkening G., Iizuka K., Industrial Uses of STM and AFM, Annals of the CIRP, Vol. 46/2, pp 597-620, 1997.

[18]   Wilkening G., Bosse H., Nano- and micrometrology – State-of-the-art and future challenges, J. of Metrology Society of India, Vol. 20/2, pp 125-151, 2005.

[19]   Hansen H.N., Carneiro K., Haitjema H., De Chiffre L., Annals of the CIRP, Vol. 55/2, pp 721-744, 2006.

[20]   Marinello F., Bruschi S., Microstructure control using large range AFM techniques, Proc. of 7th Lamdamap Int. Conf., Cranfield, pp 293-303, 2005.

[21]   Pesavento S., Applicazione del microscopio a forza atomica nell'indagine microstrutturale, M.Sc. Thesis, DIMEG, 2005.

[22]   Ruaro E., Studio di fasi secondarie di superleghe a base nichel mediante microscopio a forza atomica, M.Sc. Thesis, DIMEG, 2006.

[23]   Tognon A., Analisi microstrutturale di acciaio trip mediante microscopio a forza atomica, M.Sc. Thesis, DIMEG, 2006.

[24]   Bariani P, Bissacco G., Hansen H.N., De Chiffre L., Experimental characterization of micromilled surfaces by large range AFM, Nanoscale Calibration Standards and Methods: Dimensional and Related Measurements in the Micro- and Nanometer Range, Ed. by G. Wilkening and L. Koenders (Berlin: Wiley-VCH), pp 413-423, 2004.

[25]   International Technology Roadmap for Semiconductors, http://public.itrs.net/, 2005 (accessed on July 2006).

[26]   Marangoni M., Studio e caratterizzazione della line edge roughness, M.Sc. Thesis, DIMEG, 2006.

[27]   Roadmap Report Concerning the Use of Nanomaterials in the Medical & Health Sector, nanoRoad nanomaterial roadmap 2015 reports, 2006.

[28]   La Storia A., Ercolini D., Marinello F., Mauriello G., Characterization of bacteriocin coated antimicrobial polyethylene films by atomic force microscopy, Submitted to Applied Microbiology and Biotechnology, 2007.

[29]   Duparré A., Kaiser N., Heaton M.G., Using Atomic Force Microscopy (AFM) for Engineering Low-Scatter Thin Film Optics, Digital Instruments, Santa Barbara, 1998.

[30]   Wienss A., Persch-Schuy G., Vogelgesang M., Hartmann U., Scratching resistance of diamond-like carbon coatings in the sub-nanometer regime, Appl. Phys. Lett., Vol. 75, pp 1077-1079, 1999.

[31]   Brugger J., Vettiger P., Despont M., Durig U., Lutwyche M., Binnig G., Drechsler U., Haberle W., Rothuizen H., Stutz R., Widmer R., Ultrahigh density, high-data-rate NEMS-based AFM data storage system, J. of Microelectronic Engineering, Vol. 46/1, pp 11-17, 1999.

[32]   Golek F., Mazur P., Ryszka Z., Zuber S., Morphology of alkali halide thin films studied by AFM, Surface Science, Vol. 600/8, pp 1689-1696, 2006.

[33]   Tosello G., Gava A., Hansen H.N., Lucchetta G., Marinello F., Micro-Nano integrated manufacturing metrology for the characterization of micro injection moulded parts, Accepted for presentation at 7th euspen Int. Conf., Bremen, 2007.

[34]   Tosello G., Gava A., Hansen H.N., Lucchetta G., Marinello F., Characterization and analysis of weld lines on micro injection moulded parts using Atomic Force Microscope, Accepted for presentation at 11th Int. Conf. on Metrology and Properties of Engineering Surfaces, Huddersfield, 2007.

Chapter 3 – AFM Modeling

[35]   Scanning Probe Image Processor (SPIP™), developed by Image Metrology A/S, www.imagemet.com (accessed on December 2006).

[36]   Window Scanning x Microscope (WSxM), developed by Nanotec Electronica, www.nanotec.es (accessed on December 2006).

[37]   Danzebrink H.U., Koenders L., Wilkening G., Yacoot A., Kunzmann H., Advances in Scanning Force Microscopy for Dimensional Metrology, Annals of the CIRP, Vol. 55/2, pp 841-878, 2006.

[38]   Gainutdinov R.V., Arutyunov P.A., Artifacts in Atomic Force Microscopy, Russian Microelectronics, Vol. 30/4, pp 219–224, 2001.

[39]   Griffith J.E., Grigg D.A., Dimensional metrology with scanning probe microscopes, J. of applied physics, Vol. 74/9, pp 83-109, 1993.

[40]   Edwards H., McGlothlin R., Vertical metrology using scanning probe microscopes: Imaging distortions and measurement repeatability, J. of Applied Physics, Vol. 83/8, pp 3952-3971, 1998.

[41]   Kühle A., Sørensen A.H., Zandbergen J.B., Bohr J., Contrast artifacts in tapping tip atomic force microscopy, Appl. Phys. A, Vol. 66, pp 329-332, 1998.

[42]   Villarrubia J.S., Algorithms for Scanned Probe Mocroscope Image Simulation, Surface Reconstruction, and Tip Estimation, J. of Res. Natl. Inst. Stand. Technol., Vol. 102/4, pp 425-454, 1997.

[43]   Standard Practice for Measuring and Reporting Probe Tip Shape in Scanning Probe Microscopy, American Society for Testing and Materials, E 1813-96, pp1-11, 1998.

[44]   Villarrubia J.S., Morphological estimation of tip geometry for scanner probe microscopy, Surface Science, Vol. 321/3, pp 287-300, 1994.

[45]   Davì I., Characterization of deep, nanometer scale diffraction grating with Atomic Force Microscope, M.Sc. Thesis, DIMEG and IPL, 2005.

[46]   Dongmo L.S., Villarrubia J.S., Jones S.N., Renegar T.B., Postek M.T., Song J.F., Experimental test of blind tip reconstruction for scanning probe microscopy, Ultramicroscopy , Vol. 85/3, pp 141-153, 2000.

[47]   Bukharaev A.A., Berdunov N.V., Ovchinnikov D.V., Salikhov K.M., Three dimensional probe and surface reconstruction for atomic force microscopy using a deconvolution algorithm, Scanning Microscopy International, Vol. 12, pp 225-234, 1998.

[48]   Bariani P., Dimensional metrology for microtechnology, Ph. D Thesis, IPL-DTU, 2005.

[49]   Mokaberi B, Requicha A.A.G., Towards automatic nanomanipulation: drift compensation in scanning probe microscopes, Proc. of IEEE Int. Conf. on Robotics and Automation, pp 416-421, 2004.

[50]   Calliari R., Development and implementation of software tools for surface processing and analysis, M.Sc. Thesis, DIMEG and IPL, 2005.

[51]   Garnæs J., Kofod N., Kühle A., Nielsen C., Dirscherl K., Blunt L., Calibration of step heights and roughness measurements with atomic force microscopes, Precision Engineering, Vol. 27/1, pp 91-98, 2003.

[52]   Borsetto F. Advanced characterization of micro optical components with atomic force microscopy, M.Sc. Thesis, DIMEG IPL and DFM, 2004.

[53]   Garnæs J., Kule A., Nielsen L., Borsetto F., True three-Dimensional Calibration of closed loop scanning probe microscopes, Nanoscale Calibration Standards and Methods: Dimensional and Related Measurements in the Micro- and Nanometer Range, Ed. by G. Wilkening and L. Koenders (Berlin: Wiley-VCH), pp 193-204, 2004.

Chapter 4 – AFM Calibration

[54]   Dziomba T., Koenders L. and Wilkening G., Towards a guideline for SPM calibration, Nanoscale Calibration Standards and Methods: Dimensional and Related Measurements in the Micro- and Nanometer Range, Ed. by G. Wilkening and L. Koenders (Berlin: Wiley-VCH), pp 173-192, 2004.

[55] Misumi I., Gonda S., Sato O., Sugawara K., Yoshizaki K., Kurosawa T., Takatsuji T., Nanometric lateral scale development using an atomic force microscope with directly traceable laser interferometers, Meas. Sci. Technol., Vol. 17, pp 2041-2047, 2006.

[56] Dai G., Koenders L., Pohlenz F., Dziomba T., Danzebrink H.U., Accurate and traceable calibration of one-dimensional gratings, Meas. Sci. Technol., Vol. 16, pp 1241-1249, 2005.

[57] Feige V.K.S., Balk L.J., Calibration of a scanning probe microscope by the use of an interference–holographic position measurement system, Meas. Sci. Technol., Vol. 14, pp 1032-1039, 2003.

[58] Jørgensen J.F., Jensen C.P., Garnæs J., Lateral metrology using scanning probe microscopes, 2D pitch standards and image processing, J. of Appl. Phys., Vol. 66, pp 847-852, 1998.

[59] Kim J.A., Kim J.W., Park B.C., Eom T.B., Measurement of microscope calibration standards in nanometrology using a metrological atomic force microscope, Meas. Sci. Technol., Vol. 17, pp 1792-1800, 2006.

[60] Kofod N., Validation and industrial application of AFM, Ph. D Thesis, IPL-DTU, 2002.

[61] www.spmtips.com (accessed on December 2006).

[62] Rasia M., Sviluppo di un campione per la taratura verticale di microscopi a scansione elettronica, DIMEG, 2005.

[63] Garnæs J., Kofod N., Joergensen J.F., Kuhle A., Besmens P., Ohlson O., Rasmussen J.B., Lindelof P.E., Wilkening G., Koenders L., Mirande W., Hasche K., Haycocks J., Nunn J., Stedman M., Nanometre scale transfer standards, Proc. of 1st euspen Int. Conf., Ed. by P. McKeown, J. Corbett, Vol. 2, pp 134-137, 1999.

[64] Rerkkumsup P., Aketagawa M., Takada K., Watanabe T., Sadakata S., Direct measurement instrument for lattice spacing on regular crystalline surfaces using a scanning tunneling microscope and laser interferometry, Rev. Sci., Instrum., 74, pp 1205-1210, 2003.

[65] ISO 5436-1:2000 Geometrical Product Specification (GPS) – Surface Texture: Profile method: Measurement standards – Part 1: Material measures. International Organization for Standardization, Geneva, Switzerland, 2000.

[66] ISO 4287: 1997 Geometrical Product Specification (GPS) – Surface Texture: Profile method – Terms, Definitions and Surface Texture Patameters, International Organization for Standardization, Geneva, Switzerland, 1997.

[67] Meli F., Thalman R., Long range AFM profiler used for accurate pitch measurements, Meas. Sci. Technol., Vol. 9/7, pp 1087-1092, 1998.

[68] Dziomba T., Koenders L., Danzebrink H.U, Wilkening G., Lateral and vertical calibration of SPM and their measurement uncertainty, Proc. of XI Int. Colloquium on Surfaces, Chemnitz, Ed. by M. Dietzsch, pp 117-128, 2004.

[69] Ritter M., Hemmleb M., Sinram O., Albertz J., Hohenberg H., A versatile 3D object for various micro-range measurement methods, Proc. of 20th ISPRS 2004, Istanbul, Vol. 35/b, pp 696-701, 2004.

[70] www.microparticles.de/research_particles.html (accessed on October 2006).

[71] Marcolongo N., Studio di un artefatto per la taratura verticale di microscopi a scansione mediante sonda, DIMEG, 2005.

[72] Jensen K., Ulrich R., Drawing glass fibers with complex cross section, J. of Lightwave Technology, Vol. 9/1, pp 2-6, 1991.

[73] www.ofs.dk (accessed on September 2006).

[74] www.corning.com/opticalfiber (accessed on September 2006).

[75] www.amp.com (accessed on September 2006).

[76] www.belden.com (accessed on September 2006).

[77] Marinello F., Savio E., Use of optical fiber sections for AFM lateral calibration, Proc. of the 6th euspen Int. Conf., Baden, Vol. 1, pp 378-381, 2006.

[78] Marinello F., Savio E., Use of cylindrical artefacts for AFM vertical calibration, Meas. Sci. Technol., Vol. 18/2, pp 462-468, 2007.

[79] Marinello F., Savio E., Carmignato S., High aspect-ratio artefacts for lateral and vertical calibration, Accepted for presentation at 11th Int. Conf. on Metrology and Properties of Engineering Surfaces, Huddersfield, 2007.

[80] Marinello F., Savio E., Carmignato S., Artefatto per la taratura e il controllo di microscopi, Patent n. PD 2006 A 000211, 2006.

[81] Garnæs J., Kofod N., Kuhle A., Nielsen C., Dirscherl K. and Blunt L., Calibration of step heights and roughness measurements with atomic force microscopes, Prec. Eng., Vol. 27, pp 91-98, 2003.

[82] Meli F., Thalmann R., Z-calibration of a metrology AFM scanner using an interferometer and a tilting device with a linear stage, Proc. of the third Seminar in Quantitative Microscopy, Lyngby, PTB-F-34, pp 61-67, 1998.

[83] Min X., Pohlenz F. and Dai G., A correction method for the non-linear behaviour of the height measuring system in an SPM, Proc. of 5th euspen Int. Conf., Montpellier, Vol. 1, 181-184, 2005.

[84] Cossi S., Sviluppo e validazione validazione software software di di analisi analisi delle delle superfici superfici per le per le nanotecnologie M.Sc. Thesis, DIMEG, 2006.

[85]   Guide to the Expression of Uncertainty in Measurement, GUM, International Organization for Standardization, Geneva, Switzerland.

[86]   Zanoni S., Development and implementation of software tools for surface processing and analysis, M.Sc. Thesis, DIMEG and IPL, 2005.

Chapter 5 – Artifacts Correction

[87]   Zhang H., Huang F., Higuchi T., Dual unit scanning tunneling microscope-atomic force microscope for length measurement based on reference scales, J. of Vacuum Science & Technology B: Microelectronics Processing and Phenomena, Vol. 15/4, pp 780-784, 1997.

[88]   Jorgensen J.F., Madsen L.L., Garnæs J., Carneiro K., Schaumburg K., Calibration, drift elimination, and molecular structure analysis, J. of Vacuum Science & Technology, Vol. 12/3, pp 1698-1701, 1994.

[89]   Yaofeng S., Pang J.H.L., AFM image reconstruction for deformation measurements by digital image correlation, Nanotechnology, Vol. 17, pp 933-939, 2006.

[90]   Bariani P., Marinello F., De Chiffre L., True three-dimensional surface topography imaging with AFM, Proc. of 7th Lamdamap Int. Conf. , Cranfield, pp 286-292, 2005.

[91]   Marinello F., Bariani P., De Chiffre L., Savio E., Fast technique for AFM vertical drift compensation, Meas. Sci. Technol., Vol. 18/3, pp 689-696, 2007.

[92]   Blunt L., Stout K.J., Three-Dimensional Surface Topography, Penton Press, London, 2000.

[93]   Brand U., Kirchhoff J., A micro-CMM with metrology frame for low uncertainty measurements, Meas. Sci. Technol., Vol. 16/12, pp 2489-2497, 2005.

[94]   Küng A., Meli F., Self calibration method for 3D roundness of spheres using an ultra-precision coordinate measuring machine, Proc. of 5th euspen Int. Conf., pp 193-196, 2005.

[95]   Orji N.G., Vorburger T.V., Fu J., Dixson R.G., Nguyen C.V., Raja J. Line edge roughness metrology using atomic force microscopes, Meas. Sci. Technol, Vol. 16/11, pp 2147-2154, 2005.

[96]   Marinello F., Savio E., A method for line edge and sidewall roughness characterization, Proc. of the 6th euspen Int. Conf., Baden, Vol. 1, pp 426-429, 2006.

[97]   Garnæs J., Hansen P.E., Agersnap N., Daví I., Petersen J.C., Kühle A., Holm J., Christensen L.H., Determination of sub-micrometer high aspect ratio grating profiles, Advanced Characterization Techniques for Optics, Semiconductors, and Nanotechnologies II, Proc. of SPIE, Vol. 5878, pp 23-31, 2005.

[98]   www.aurorand.com (accessed on December 2006).

[99]   Chu C.M., The effect of complexing agents on the electrodeposition of Fe-Ni powders, J. Chinese Inst. Chem. Eng., Vol. 34/6, pp 689-695, 2003.

[100]   Czerkas S., Dziomba T. and Bosse H., Comparison of different methods of SFM tip shape determination for various characterisation structures and types of tip, Nanoscale Calibration Standards and Methods: Dimensional and Related Measurements in the Micro- and Nanometer Range, Ed. by G. Wilkening and L. Koenders (Berlin: Wiley-VCH), pp 311-320, 2004.

[101]   Machleidt T., Katsner R., Franke K.H., Reconstruction and geometric assessment of AFM tips, Nanoscale Calibration Standards and Methods: Dimensional and Related Measurements in the Micro- and Nanometer Range, Ed. by G. Wilkening and L. Koenders (Berlin: Wiley-VCH), pp 297-310, 2004

[102]   Hubner H., Morgenroth W., Meyer H.G., Sulzbach T., Brendel B. and Mirandé W., Downwards to metrology in nanoscale: determination of the AFM tip-shape with well-known sharp-edged calibration structures Appl. Phys. A , Vol. 76/6, pp 913-917, 2003.

[103]   Carli L., Shape and wear of Atomic Force Microscope (AFM) tips, M.Sc. Thesis, DIMEG IPL and DFM, 2007.

[104]   Archard J.F., Contact and Rubbing of Flat Surfaces, J. of Appl. Phys., Vol. 24, pp 981-988, 1953.

[105]   Chung K.H., Lee Y.H., Kim D.E., Yoo J. Hong S., Tribological Characteristics of Probe Tip and PZT Media for AFM-Based Recording Technology IEEE Transactions on Magnetics, Vol. 41/2, pp 849-854, 2005.

[106]   Zhang X., Meng Y., Wen S., Micro contact and stick-slip number between AFM probe tip and sample surface, Science in China Series E-Technological Sciences, Vol. 46/5, pp 537-545, 2003.

[107]   Fu J., Li B., Han Y., Molecular motions of different scales at thin polystyrene film surface by lateral force microscopy, J. of Chem. Phis., Vol. 123, pp 1-9, 2005.

[108]   Maw W., Stevens F., Langford S.C., Dickinson J.T., Single asperity tribochemical wear of silicon nitride studied by atomic force microscopy, J. of Appl. Phys., Vol. 92/9, pp 5103-5109, 2002.

Chapter 6 – Instrument Enhancement

[109]   www.nanosensors.com (accessed on December 2006).

[110]   Pasquini A., Picotto G.B., Pisani M., STM carbon nanotube tips fabrication for critical dimension measurements, Sensors and Actuators A: Physics, Vol. 123-124, pp 655-659, 2005.

[111]   Dai G., Wolff H., Xu M., Pohlenz F., Danzebrink H.U., Nanoscale surface measurements at sidewalls of nano- and micro-structures, Meas. Sci. Technol., Vol. 18/2, pp 334-341, 2007.

[112] Marinello F., Bariani P., Pasquini A., De Chiffre L., Bossard M. and Picotto G.B., Increase of maximum detectable slope with optical profilers, through controlled tilting and image processing, Meas. Sci. Technol., Vol. 18/2, pp 384-389, 2007.

[113] Schwenke H., Neuschaefer-Rube U., Pfeifer, T. and Kunzmann H., Optical methods for dimensional metrology in production engineering, Annals of the CIRP, Vol. 51/2, pp 685-699, 2002.

[114] De Chiffre L., Kunzmann H., Peggs G.N., Lucca D.A., Surfaces in Precision Engineering, Microengineering and Nanotechnology, Annals of the CIRP, Vol. 52/2, pp 561-577, 2003.

[115] Liang-Chia C., Development of white light confocal microscopy with innovative fringe projection for full-field micro surface profilometry, IEEE Int. Conf. on Mechatronics, pp 301-306, 2005.

[116] Davis F.A., Replica techniques in the study of crankshaft journal topography, Automot. Eng., Vol. 4/2, pp 46-47, 1979.

[117] Lehmann T.M., Survey: interpolation methods in medical image processing, IEEE Trans. on Medical Imaging, Vol. 18/11, pp 1049-1075, 1999.

[118] Price J.R., Resampling and reconstruction with fractal interpolation functions, IEEE Signal Processing Letters, Vol. 5/9 , pp 228-230, 1998.

[119] www.physikinstrumente.com (accessed on November 2006).

[120] Marinello F., Development and implementation of a software tool and test on an integrated system for surface mapping at nanometre scale, M.Sc. Thesis, DIMEG and IPL, 2003.

[121] www.fogale.fr (accessed on September 2006).

[122] Chu W., Zhao X., Fu J., Vorburger T.V., Study of an image stitching method for linewidth measurement, Photomask and Next-Generation Lithography Mask Technology XI Proc. of SPIE, Vol. 5446, pp 776-783, 2004.

[123] Dai G., Pohlenz F., Danzebrink H.U., Xu M., Hasche K., Wilkening G., A novel metrological large range scanning probe microscope applicable for versatile traceable topography measurements, Proc. of the 4th euspen Int. Conf., Glasgow, pp 228-229, 2004

[124] Dai G., Pohlenz F., Danzebrink H.U., Xu M., Hasche K., Wilkening G., Metrological large range scanning probe microscope, Rev. of Scientific Instruments, Vol. 75/4, pp 962-969, 2004.

[125] Wyant J.C., Schmit J., Large Field of View, High Spatial Resolution, Surface Measurements. International Journal of Machine Tools & Manufacture 1998, Vol. 38/5-6, pp 691-698, 1998.

[126] Yanagi K., Hasegawa M., Hara S., A computational method for stitching a series of 3D surface topography data measured by microscope-type surface profiling instruments. Proc. of 3rd euspen Int. Conf., Eindhoven, Vol. 2, pp 653-656, 2003.

[127] Dai G., Koenders L., Pohlenz F., Dziomba T., Danzebrink H.U.. Accurate and traceable calibration of one-dimensional gratings, Meas. Sci. Technol., Vol. 16, pp 1241-1249, 2005.

[128] De Chiffre L., Marinello F., Bariani P., Hansen H.N., Surface Mapping with an AFM-CMM Integrated System and Stitching Software, Proc. of 4th euspen Int. Conf., Glasgow, pp 326-327, 2004.

[129] Marinello F., Bariani P., De Chiffre L., Hansen H.N., Development and analysis of a software tool for stitching three dimensional surface topography data sets, Accepted for publication in Meas. Sci. Technol., 2006.

[130] Marinello F., Savio E., De Chiffre L., A software tool for surface topography relocation, Proc. of 6th euspen Int. Conf., Baden, Vol. 1, pp 398-401, 2006.

[131] Marinello F., Savio E., De Chiffre L., A software tool for sub-pixel surface topography relocation, Proc. of 7th AITeM Conf., pp 51-52, 2005.

[132] Thomas M., Misra S., Kambhamettu C., Kirby J.T., A robust motion estimation algorithm for PIV, Meas. Sci. Technol., Vol. 16/3, pp 865-877, 2005.

[133] Baggio M., Studio delle prestazioni di procedure software per l'analisi di superfici, M.Sc Thesis, DIMEG, 2005.

[134] Baroncelli O., Sviluppo di procedure per la taratura di un rugosimetro da laboratorio e campioni di rugosità, M.Sc Thesis, DIMEG, 2004.

[135] Bianco R., Sviluppo di procedure di prova e taratura nella misura dello stato della superficie, M.Sc Thesis, DIMEG, 2005.

[136] Marinello F., Bariani P., De Chiffre L., Hansen H.N., Roughness measurements with an AFM-CMM instrument, Proc. of 5th euspen Int. Conf., Montpellier, Vol. 1, pp 229-232, 2005.

[137] Nanosurf® Easy Scan 2, by Nanosurf Ag., www.nanosurf.com (accessed on December 2006).

[138] NPL Optical Dimensional Standard, www.npl.co.uk/length/dmet/ (accessed on October 2006).

[139] Savio E., Marinello F., Bariani P., Carmignato S., Feature-Oriented Measurement Strategy in Atomic Force Microscopi, Provisionally accepted for publication in the CIRP Annals, Vol. 56/1, 2007.

Appendix A

Instruments description

A.1   Scanning Probe Microscopes

In this section the main instruments used within experimental sessions are described. This part has been intentionally excluded by the main body, to stress the fact that proposed solutions are generally independent from the used instruments and can be in principle used to a wide range of instruments available in the market.

A.1.1 AFM-CMM integrated instrument

During the past few years, a set-up has been constructed at IPL-DTU based on an AFM scanner mounted on the z axis of a three axis CMM. The CMM works as positioning stage for the AFM scanner. The set-up has been extensively described in [48] and [60].

A.1.1.1 CMM

The CMM is a three-coordinate measuring machine produced by SIP, on which movement and detection of axis positions are performed manually. The CMM has a working volume of 400 mm, 100 mm and 75 mm respectively on x, y and z direction (Figure B.1).

The integrated system is provided with electronic scales on the X and Y axes of the CMM. No scales are installed on the Z axis, since this axis is only used for the rough positioning of the AFM probe. The scales are manufactured by Heidenhain, produced in Zerodur material (LIP-series). The X-scale has a total length of 370 mm and the Y-scale is 120 mm. They have a fine signal period of 2 µm which permits measuring steps down to 50 nm.
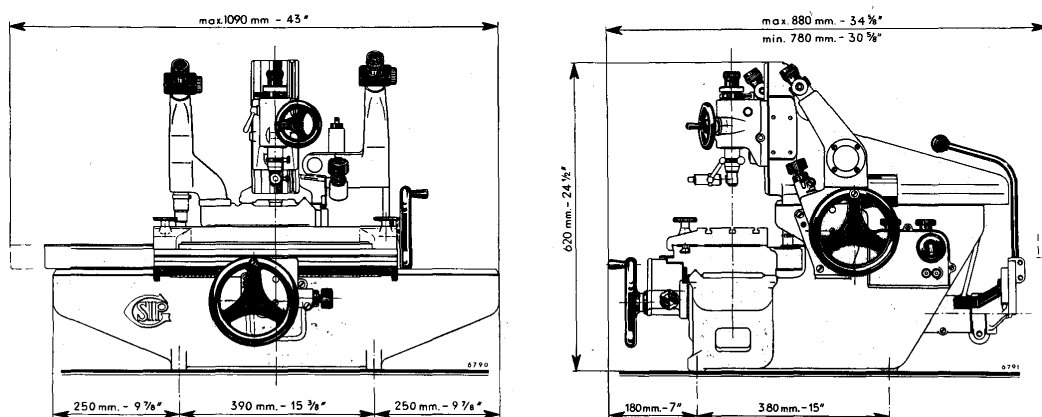

Figure B.1 The CMM used as positioning means for the AFM scanner in the Large range AFM developed at IPL -DTU.

A.1.1.1 AFM

An Atomic Force Microscope scanner DME DS 95-200 is mounted on the z axis of the CMM (Figure B.2). The AFM sensor has a nominal scanning range of 200×200 µm². Lateral scan is realized through a tube piezoelectric scanner; z readout based on laser triangulation. However, no further constructive details of the vertical detection system was given, being of strategic importance for the manufacturer. The instrument data sheet is shown in Table B.1.

Table B.1: AFM technical specifications.

Technical specifications for DME 95-200 AFM scanner:	
Scanner	· X, Y scan size: 200×200 µm · X, Y resolution: < 1 nm · Z range: 15 µm · Z resolution: < 0.5 nm · Z-linearization: 0.5% on full-scale scan · Maximum sampling: 1024×1024 pixels
Approach	· Type: Automatic · Length: > 1.5 mm
Operation	· Mode: AC, DC, LFM, MFM · Optional mode: STM, E-probing · Imaging: Topography, Phase, Lateral Force
Objective	·Type: Bright Field · Focal length: 95 mm · Magnification: 15X

The integrated instrument (Figure B.2) cab basically work in three different ways:

• The CMM positions the AFM probe and a measurement covering max 40 µm $\times$ 40 µm is performed (correspond-ing to the maximum scan area of the AFM).

• The CMM positions the AFM probe at different places for spotwise investigation of larger areas within the CMM working volume (X $\times$ Y $\times$ Z max 400 mm $\times$100 mm $\times$ 75 mm).

• The CMM is used to reposition the AFM probe in between surface roughness measurements to cover continuous areas larger than 40 µm $\times$ 40 µm (called surface mapping).

Figure B.2: A picture of the Large range AFM during operation. The AFM is mounted on the z axis of the CMM. On top of the scanner, a CCD camera is used for positioning. The readout of the electronic scales can be discerned on the right side.

A.1.2 Open loop AFM

An identical DME DS 95-200 Atomic Force Microscope, mounted on the z axis of a conventional stage for optical microscopes, was also present in the Geometrical and Industrial Metrology Laboratory at DIMEG -University of Padua (Figure B.3). This scanner, together with the AFM-CMM integrated instrument, was applied to run the big majority of experiments presented in this thesis.

Figure B.3: A picture of the open loop AFM mounted on a conventional stage.

A.1.3 Metrological AFM

In connection with investigations presented in Paragraph 5.2.4, a set of measurements were produced by DFM (Danish Fundamental Metrology Ltd) with a metrological AFM. This was a Dimension™ 3100 with metrology head, produced by Digital Instruments, now Veeco. Scanning is obtained and controlled by a closed loop system based on feedback from capacitive distance sensors. Actuation is ensured by piezo-electric ceramics, with a parallelogram architecture (Figure B.4). The AFM sensor data sheet is shown in Table B.2.

Table B.2: AFM technical specifications.

Technical specifications for DI Dimension™ 3100 AFM scanner:
· X, Y scan size: 70 × 70 µm · X, Y resolution: < 1 nm · Z range: 6 µm · Z resolution: < 0.5 nm · Z-linearization: 0.5% on full-scale scan · Maximum sampling: 512 × 512 pixels

a   **b**
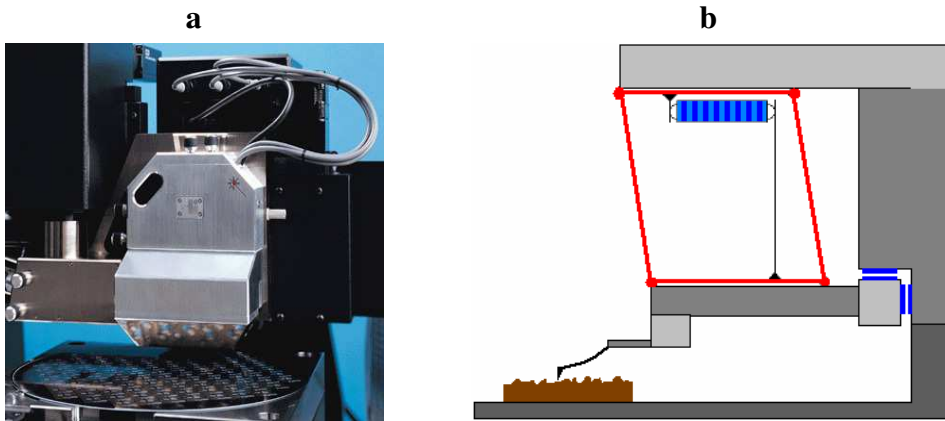

Figure B.4: a) Image of the metrology AFM and b) Sketch of the metrology system, with parallelogram architecture.

A.1.4 AFM with control interface.

For the study presented in Chapter 6.4, a commercially available instrument was applied (Nanosurf® Easy Scan 2, developed by Nanosurf Ag. [137]). This is an instrument based on a electromagnetic scanner (voice coil actuators), providing fairly linear probe drive (Figure B.5). A script-interface to program the instrument control was available, allowing advanced scanning modes, such as free pattern probe steering, useful for feature oriented analyses. Measurements were carried out in dynamic force mode (vibrating the probe over the sample surface at approximately its resonance frequency). The AFM sensor data sheet is shown in Table B.3.

Table B.3: AFM technical specifications.

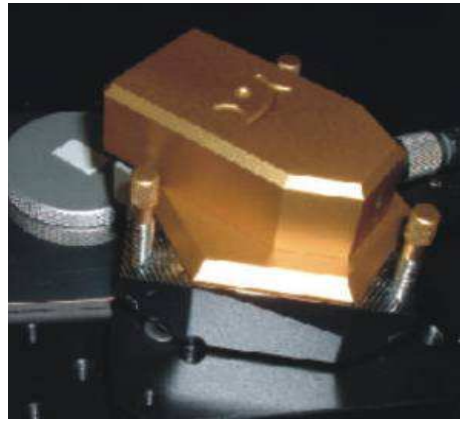| Technical specifications for Nanosurf Easy Scan 2 AFM scanner: |
| --- |
| · X, Y scan size: 70 × 70 µm
· X, Y resolution: 1.1 nm
· Z range: 14 µm
· Z resolution: 0.21 nm
· X Y linearity: <1.2%
· Z noise level: 0.5 nm
· Maximum sampling: 2048 × 2048 pixels |

Figure B.5: A picture of Atomic Force Microscope used for feature oriented measurements.

A.2   White Light Interferometer

In connection with double tilt technique for surface reconstruction, a set of experiments was conducted, involving use of optical based instruments. In particular for the results reported in Paragraph 6.2.4, a white light interferometer was used. The 3D optical profiler, used for our tests was a Fogale Nanotech PhotoMap 3D interference microscope [121]. The microscope was equipped with a 50X Mirau type interference objective. The instrument data sheet is shown in Table B.4.

Table B.4: Interference microscope specifications.

Technical specifications for Fogale Nanotech PhotoMap 3D microscope:
· X, Y resolution: 0.6 µm · Z range: 500 µm · Z resolution: 0.2 nm rms (Monochromatic light phase shifting technique) · Z resolution: 6 nm rms (White light scanning technique) · 8µm step height repeatability: 20nm · 50µm step height repeatability: 30nm

Sample tilt was performed with a closed-loop single axis rotation stage: PI M-037 DG Rotation stage driven by linear DC motor and controlled through a Mercury C 862.00 controller (Figure B.6). The stage was supplied with an integrated spring preload eliminates backlash. The worm gear ratio is 180:1, corresponding to a turntable rotation of 2 degrees per revolution of the drive shaft: 0.1 degree graduations. The rotation stage data sheet is shown in Table B.5. The complete integrated system, optical profilometer and tilting stage, is reproduced in the figure below (Figure B.6).

Table B.5: Rotation stage specifications.

Technical specifications for PI M-037 DG Rotation stage:
· Design resolution: 0.59 µrad (34 x 10^{-6} deg) · Min. incremental motion: 3.5 µrad · Unidirectional repeatability: 30 µrad · Backlash: 200 µrad · Maximum velocity: 6 °/s · Wobble: <150 µrad · Maximum axial force: ±300 N · Encoder resolution: 2000 counts/rev. · Worm Gear ratio : 180:1

Figure B.6: A picture of the rotational stage, integrated with the optical profilometer.

A.3   Stylus Profilometer

In Paragraph 6.3.3 a technique is proposed for stitching of topographic images. This is reported as an enhancement for atomic force microscopy, but is in principle applicable to all instrument for surface profilometry. An example is in fact reported involving measurements made by a stylus profilometer at CGM. The traceable roughness profilometer is a RTH Talysurf 5-120, specially constructed for 3D roughness measurement. The stylus profilometer data sheet is reported in Table B.6.

Table B.6: Stylus profilometer specifications.

Technical specifications for PI M-037 DG Rotation stage:
· X resolution: 0.1 µm · X range: 120 mm · Y resolution: 0.5 µm · Y range: 150 mm · Z resolution: 0.1 nm · Z range: 0.6 mm

Appendix B

Filters

B.1   Filtering masks

Data processing through specific filtering masks can help very much surface characterization. In particular noise filtering and edge detection tools are of primary importance for a lot of analysis operations. This appendix is devoted to the description of an automatic routine implemented into commercial software [35], for supporting some topography analyses. Nevertheless filtering masks are not always recommendable, since they produce a convolution operation, inevitably introducing distortions in the processed data (see Paragraph 3.3.11).

B.1.1 Statistical filters

Not many words will be spent for statistical filters, commonly applied for noise removal. Plenty of tools is already available into commercial software: in particular Gaussian and Fourier Based Filters are exceptional tools for surface topographies "cleaning".

The following masks are implemented in the developed software tool.

Smoothing 3x3

$$\frac{1}{9}\begin{array}{|c|c|c|}\hline 1 & 1 & 1 \\\hline 1 & 1 & 1 \\\hline 1 & 1 & 1 \\\hline\end{array}$$

Smoothing 5x5

$$\frac{1}{15}\begin{array}{|c|c|c|c|c|}\hline 1 & 1 & 1 & 1 & 1 \\\hline 1 & 1 & 1 & 1 & 1 \\\hline 1 & 1 & 1 & 1 & 1 \\\hline 1 & 1 & 1 & 1 & 1 \\\hline 1 & 1 & 1 & 1 & 1 \\\hline\end{array}$$

Gaussian

$$\frac{1}{159}\begin{array}{|c|c|c|c|c|}\hline 2 & 4 & 5 & 4 & 2 \\\hline 4 & 9 & 12 & 9 & 4 \\\hline 5 & 12 & 15 & 12 & 5 \\\hline 4 & 9 & 12 & 9 & 4 \\\hline 2 & 4 & 5 & 4 & 2 \\\hline\end{array}$$

B.1.2 Gradient edge detection

An edge can be defined as a place of transition from one object to another: no perfect borders are generally detectable, but probable transitions are clearly recognizable.

Edge detection is a critical issue whenever grain analysis is needed.

An edge detector is generally based on local gradient evaluation. Gradient operation, applied to a generic function f, is generally referred as (B.1):

$$\nabla f = \begin{bmatrix} \dfrac{\partial f(x, y)}{\partial x} \\[2ex] \dfrac{\partial f(x, y)}{\partial y} \end{bmatrix} \tag{B.1}$$

∇f is a vector bringing to relevant kind of information:

- the intensity (or magnitude) defines the relevance of the edge, by amounting the difference between the given pixel and neighbour points.

- the direction defines the maximum slope direction, generally orthogonal to the edge.

Prewitt: quantifies the central difference. It is averaged on three lines, but is quite noise sensitive. Here below the x-direction and y-direction masks.

$$\frac{1}{3} \begin{bmatrix} -1 & 0 & 1 \\ -1 & 0 & 1 \\ -1 & 0 & 1 \end{bmatrix}$$

$$\frac{1}{3} \begin{bmatrix} -1 & -1 & -1 \\ 0 & 0 & 0 \\ 1 & 1 & 1 \end{bmatrix}$$

Sobel: this filter is based on central difference, as well, but gives double weight to central line when averaging. It can be seen as derivative of a function after Gaussian smoothing is (B.2):

$$\frac{\partial(f \circ G)}{\partial x} = f \circ \frac{\partial G}{\partial x} \approx f \circ Sobel(x) \tag{B.2}$$

Here below the 3x3 and 5x5 x-direction and y-direction masks.

$$\frac{1}{4} \begin{bmatrix} -1 & 0 & 1 \\ -2 & 0 & 2 \\ -1 & 0 & 1 \end{bmatrix}$$

	-1	-2	-1
$\frac{1}{4}$	0	0	0
	-1	-2	-1

	1	2	0	-2	-1
	4	8	0	-8	-4
$\frac{1}{48}$	6	12	0	-12	-6
	4	8	0	-8	-4
	1	2	0	-2	-1

	-1	-4	-6	-4	-1
	-2	-8	-12	-2	-2
$\frac{1}{48}$	0	0	0	0	0
	2	8	12	8	2
	1	4	6	4	1

<u>Diagonal Arrow:</u> developed for enhance diagonal discontinuities.

-1	-2	0	0	0
-2	-3	0	0	0
0	0	0	0	0
0	0	0	-3	-2
0	0	0	-2	-1

<u>Mrnl:</u> experimental mask developed for edge fine detection.

1	2	2	2	1
2	3	3	3	2
0	0	0	0	0
-2	-3	-3	-3	-2
-1	-2	-2	-2	-1

B.1.3 Curvature edge detection

Laplacian function is mathematically defined as (B.3):

$$\nabla^2 f = \nabla(\nabla f) = \frac{\partial^2 f}{\partial x^2} + \frac{\partial^2 f}{\partial y^2} \tag{B.3}$$

Edges are detected where Laplacian function goes to zero: these points corresponding to gradient maxima i.e. to those positions where local curvature changes from positive to negative or viceversa.

Laplacian 3x3: second derivative can be expressed as (B.4):

$$\frac{d^2 f}{dx^2} \approx [f(x+1) - f(x)] - [f(x) - f(x-1)] = f(x+1) - 2f(x) + f(x-1) \tag{B.4}$$

A simple [1,-2,1] operator can be therefore applied to approximate second derivative.

The following mask is eventually achieved:

0.5	0	0.5
1.0	-4	1
0.5	0	0.5

$+$

0.5	1	0.5
0	-4	0
0.5	1	0.5

$=$

1	1	1
1	-8	1
1	1	1

Laplacian 5x5: Laplacian operator may detect edges as well as noise: for this reason it may be desirable to smooth the image first by convolution with a Gassian operator. Since convolution is associative amd commutative, Goussian and Laplacian operator can be combined in a single edge finding operator.

By differentiating the Gaussian function, it is found (B.5):

$$G(x, y) = e^{-r^2/2\sigma^2} \qquad \rightarrow \qquad \nabla^2 G(x, y) = \left(\frac{r^2 - \sigma^2}{\sigma^4} \right) e^{-r^2/2\sigma^2} \tag{B.5}$$

By discretizing (B.5), the 5x5 convolution kernel can be found (normally known as Laplacian of Gaussian, LoG):

0	0	-1	0	0
0	-1	-2	-1	0
-1	-2	16	-2	-1
0	-1	-2	-1	0
0	0	-1	0	0

B.1.4 Mask direction

Surface topographies achieved through Scanning Probe Microscopy technology should have to be considered as collection of profiles, rather than real 3D data sets.

For these reason analysis tools processing data along the same scanning direction are preferred by the author. Nevertheless great advantage can be brought by an analysis tool working perpendicularly to that.

In the developed software tool 3 options are available: *x* and *y direction*, corresponding respectively to horizontal and vertical axes (Fig 1) and *All directions.* In the last case, the selected mask is rotated by 16 rotational shifts: the higher value is eventually given as an output for each pixel.

Kirsch Compass: this tool, widely known and applied, has been developed based on the concept (called Compass operation) described here above. The base mask is the following:

3	3	3
3	0	3
-5	-5	-5

B.1.5 Other

Sometime development of new masks is important, to give an answer to specific needs. In fact a mask engineered for a particular topography can bring to better results. For this reason an open dialog mask has been set in the developed software tool. Positive and negative integer number can be freely set.

Here below two examples:

- the fist one is an unbalanced matrix, giving in the output the original topography summed up with the first derivative: the result is thereafter the beginning surface with stressed edges;
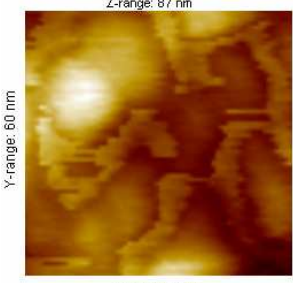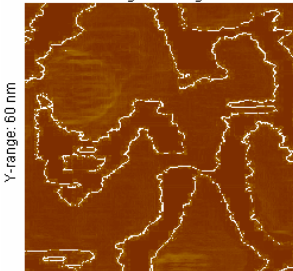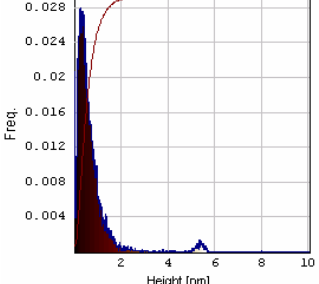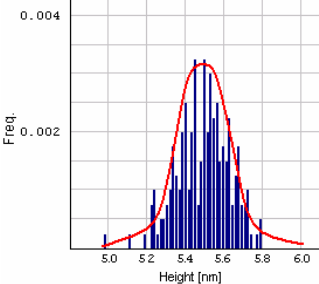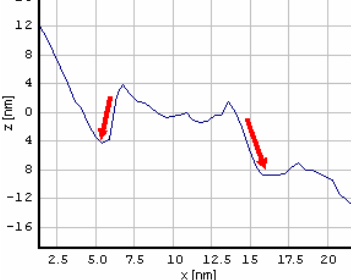

- the particular distribution of coefficients in this second matrix is minded to enhance circular grains edge.
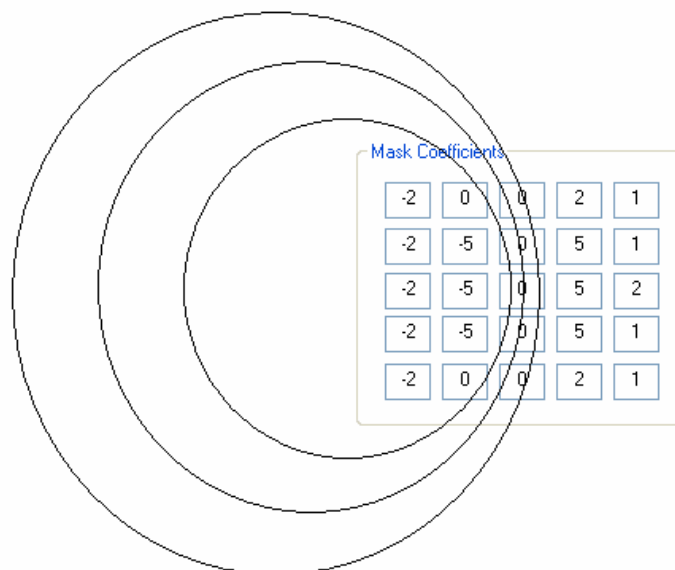
B.2   A solution to mode switching

As anticipated in Paragraph 3.3.5, filtering masks can be of help for detecting mode switching artifacts, providing also a partial compensation. The method is described in the following table.

Table B.1: Mode switching compensation method.

	Generally mode switching is present as unexpected height shifts. The sudden increase/decrease in the amplitude is then related to the tip to surface interaction. For a given surface, characterized through AFM with a given set of parameters, the phenomenon has a certain stability. In fact it occurs in proximity of well defined topography slopes and curvatures, producing height shifts with a certain constancy.
	Through edge detection and segmentation procedures, it is possible to isolate jumps that most probably are related to mode switching distortions.
	The height distribution histogram, evaluated on the segmented image, presents a U shaped diftribution. The left higher peak is descriptive of topography "normal" variations. The peak on the right, even if small, is indicative of a systematic step affecting the surface topography.
	A close look to the second peak allows for determination of average step due to mode switching.
	The detected mean height shift can eventually be used for a correction of distorted profiles.